

Heavy Precipitation Biases in the TRMM PR and TMI Products and Their Origins Assessed with CloudSat and Reanalysis Data

(TRMM PRおよびTMIプロダクトの強雨バイアス検証ならびにCloudSatおよび再解析データを用いたその要因評価)

Andung Bayu Sekaranom

(アンドウン バユ セカラノム)

Heavy Precipitation Biases in the TRMM PR and TMI Products and Their Origins Assessed with CloudSat and Reanalysis Data

(TRMM PRおよびTMIプロダクトの強雨バイアス検証なら
びにCloudSatおよび再解析データを用いたその要因評価)

Andung Bayu Sekaranom

(アンドウン バユ セカラノム)

A dissertation for the degree of Doctor of Science
Department of Earth and Environmental Sciences
Graduate School of Earth and Environmental Studies
Nagoya University

(名古屋大学大学院環境学研究科地球環境科学専攻学位論文 博士(理学))

2018

Abstract

This study aims to 1) identify the properties of the differences in extreme rain estimations among the Tropical Rainfall Measuring Mission (TRMM) data products, that is, the precipitation radar (PR) 2A25 TRMM Microwave Imager (TMI) 2A12, and TRMM Multisatellite Precipitation Analysis (TMPA) products, and 2) characterize the background physical processes in the development of those heavily precipitating clouds that contribute to the inter-product differences. In the first step, a case study over the Maritime Continent is conducted to identify the statistical properties of the climatological and extreme precipitation. The analysis is then extended to different regions over the globe in light of the atmospheric environment responsible for the algorithmic errors. The global observations of the TRMM, CloudSat, and ECMWF Reanalysis (ERA) Interim datasets from 2006 to 2014 are utilized to explain the precipitation biases. An extreme rain database is constructed by extracting the highest portion of the rain-rate distribution from the rain-rate climatology at each $0.25^\circ \times 0.25^\circ$ grid resolution.

The Maritime Continent climatology, which is first studied as a pilot case study, shows that the PR-TMI rain rate differences are larger over land and coast than over ocean. When extreme rain is isolated, a higher frequency of occurrence is identified by the PR over ocean, followed by the TMI and the TMPA. Over the Maritime Continent land, the TMI yields higher rain frequencies than the PR with an intermediate range of rain rates (between 15 mm h^{-1} and 25 mm h^{-1} , but it gives way to the PR for the highest extremes. The turnover at the highest rain rates over the Maritime Continent arises because the heaviest rain depicted by the PR does not necessarily accompany the strongest ice-scattering signals, which the TMI relies on for estimating precipitation over land and coast. The PR identifies heavy rain events with lower storm top heights, and the PR rain-rate increases downward to the surface while such a vertical gradient is absent for the TMI.

In order to understand the sources of precipitation biases in more depth, the analysis is expanded to other geographical regions across the global tropics. In general, the PR identifies a larger number of rain events in the upper end of the rain-rate

distribution, similarly to the Maritime Continent. Over land, the TMI detects a large number of extreme events associated with abundant ice particles during afternoon peak precipitation, while the PR does not observe as many extreme events. Over ocean, the TMI identifies extreme events with stronger emission signals than the PR. The TMI ice-scattering channels also capture a regional gradient between Eastern and Western Pacific Ocean. TMI extreme events are associated with higher ice-scattering signals than the PR over Western Pacific Ocean, but lower signals over Eastern Pacific Ocean. Nevertheless, the PR overall exceeds the TMI in extreme rain estimates over the entire ocean domains.

The TRMM PR and TMI precipitation estimates are studied in light of the CloudSat radar reflectivity and ERA-Interim data to assess the atmospheric environment such as the cloud structure and thermodynamic field associated with the precipitation system. The CloudSat and ERA-Interim data are composited with respect to the occurrence of extreme rains to identify the detailed cloud structures and the background environmental conditions which are not captured by the TRMM. The CloudSat composite analysis shows that the PR and TMI capture different degrees of convective organizations. Over the tropical ocean, the TMI identifies heavy rainfall events with notable convective organizations and clear regional gradients between the western and eastern Pacific Ocean, while the PR fails to capture the eastward shallowing of convective systems. Over tropical land, the TMI tends to preferentially detect deep isolated precipitation clouds in relatively drier and unstable environments, while the PR identifies more organized systems. The PR-TMI differences for the moist and stable environments are reversed over tropical land. The cloud vertical-horizontal extents at different level of organizations affect the distribution of liquid and ice particles, which are responsible to the PR-TMI estimation biases in extreme rainfall.

Table of Contents

1. Introduction	1
1.1 Background	1
1.1.1 The Tropical Rainfall Measurement Mission (TRMM)	2
1.1.2 TRMM PR-TMI rain estimation biases	3
1.1.3 TRMM PR-TMI extreme-rain biases	4
1.2 Objectives and outline of this thesis	6
2. Data and method	12
2.1. Data	12
2.2 Method	14
2.2.1 Spatial and temporal coverage of the analysis	14
2.1.3 TRMM data processing	14
2.2.3 Extreme rainfall analysis	15
2.2.4 CloudSat and ERA-Interim data processing	16
3. Comparison of TRMM PR-TMI rain estimation biases in general and extreme rainfall: A case study of the Maritime Continent	22
3.1 The Maritime Continent Heavy Rainfall	22
3.2 Statistical Intercomparison	23
3.3 Rain rate probability distribution	27
3.4 Comparison of Extreme Rainfall	28
3.5 Discussion and Summary	30
4. TRMM PR-TMI regional extreme-rain biases and its difference in the retrieval process	45
4.1 A global view of TRMM PR-TMI climatological and extreme-rain estimation biases ...	45
4.2 Regional comparison of the diurnal cycle	47
4.3 Comparison of collocated PR Radar reflectivity profiles	48
4.4 Comparison of collocated TMI brightness temperatures	50
4.5 Discussion and Summary	51

5. Explaining the origin of TRMM PR-TMI extreme-rain biases	
using CloudSat and Reanalysis data	67
5.1 TRMM PR-TMI heavy rainfall biases in the view of CloudSat composite cloud structure and convective fractions.....	67
5.2 TRMM PR-TMI heavy rainfall biases in the view of environmental instability from ERA-Interim.....	69
5.3. TRMM PR-TMI heavy rainfall biases and its association with precipitation organizations	71
5.4. Discussion and Summary	73
6. Conclusions	86
References	89

1. Introduction

1.1 Background

Precipitation systems in global tropics are often characterized by the high frequency of heavy rainfall events. The extreme events have significant contributions to the large frequency of hydrometeorological hazards over this area. For example, an analysis of 11-year records of global flood frequency in 1998-2008 shows that a considerable number of fatalities over South and South East Asian Countries, African Sahel, and Central American Regions (Adhikari et al. 2010). Heavy rain events are also responsible for triggering landslides, which also generate a significant number of casualties over those regions (Kirschbaum et al. 2009). Information about heavy rain events is therefore important as an input in monitoring and forecasting hydrometeorological hazards (Hong et al. 2007; Pappenberger et al. 2012), which in turn, could be beneficial for reducing societal exposure to those hazards.

Various studies have been aimed to characterize the environmental factors accompanying the extreme rain events over the global tropics. In general, extreme rain events are related to large instability near the surface and large-scale moisture convergence in the thunderstorm development (Reale et al. 2012). In the initial stage, warm-moist air at near-surface begins to rise due to the large positive buoyancy. In the mature stage, the top of clouds approaches tropopause and forms anvil top. Heavy precipitations occur primarily in this stage due to intensive condensation above the freezing level. In the dissipating stage, the updraft stops and the precipitation decreases (Houze 1993). Heavy rain events are also often associated with mesoscale convective systems (MCSs) (Maddox 1980). In MCSs, precipitating clouds become organized and last over several hours or even longer (Houze 1993). Heavy precipitation can accumulated to a considerable degree when the systems are maintained for a long duration at the same location (Moore et al. 2012; Schumacher and Johnson 2005).

Despite the importance of monitoring extreme rainfall, various constraints still exist due to limitations of ground observations in measuring precipitation. Most ground observations over land depend on the availability of weather stations and radar networks. The existence of mountainous areas, deserts, forests, and remote islands hinders the

deployment of those networks (Liu and Zipser 2014). Over the global ocean, the ground measurements mostly depend on buoys, which are also unevenly distributed (Liu and Zipser 2014). The above conditions result in the lack of observations, so the general mechanisms of the extreme precipitation development in the Tropics are hardly explained using ground-based observations only.

1.1.1 The Tropical Rainfall Measurement Mission (TRMM)

Precipitation estimates derived from satellite observations are now widely used in various meteorological studies to overcome the limitations in ground-based observations. One of the earliest precipitation estimation methods was developed by using infrared (IR) sensors obtained from geostationary satellites (Griffith et al. 1978). IR sensors measure cloud top temperatures as a proxy of surface precipitation estimations, although these measurements are known to be only indirect estimations. Currently, precipitation estimations using passive microwave (PMW) radiometers are widely used, and many satellites carry these instruments. PMW radiometers use a more direct approach of measuring emission signals from liquid-phase hydrometeor contents as well as scattering signals from ice-phase hydrometeors inside precipitating clouds (Wilheit 1986; Wilheit et al. 1994). A further breakthrough was brought about by the Tropical Rainfall Measurement Mission (TRMM) (Kummerow et al. 1998). The TRMM was equipped with a precipitation radar (PR) as an active sensor in addition to the TRMM microwave imager (TMI), which was a passive sensor (Kummerow et al. 1998; Simpson et al. 1996).

Substantial amounts of precipitation data over the global tropics have been collected through the TRMM mission. The long-term observations (from the end of 1997 to 2014) have enabled the detection of numerous rare events related to precipitation, particularly extreme rainfall. Information regarding various key aspects related to extreme events might be retrieved from rainfall estimates derived from both TRMM PR and TMI. PR is the first spaceborne precipitation radar with a 13.8 GHz frequency band with vertical profiling ability in detecting raindrop-size particles (Iguchi et al. 2000). The vertical profiling ability is achieved by measuring the time difference between each transmitted radar pulse and received echo signals (Figure 1). By measuring the return time, distances between the observed object and the satellite could be calculated and

converted to heights. In the PR algorithm, rain-rates are determined by the relationships between radar reflectivity (Z), specific attenuation (k) and rain rate (R) as well as the path integrated attenuation (PIA) (Iguchi et al. 2000).

In contrast to PR, TMI estimates precipitation based on microwave emissions and ice-scattering signals from precipitating clouds (Kummerow and Giglio 1994; Kummerow et al. 1996). The TMI estimates instantaneous rain rates based on a given set of brightness temperature inputs from the emission bands (10, 19, 21, and 37 GHz) and 85 GHz ice-scattering bands (Kummerow et al. 1998). Physically-based assumptions are utilized to derive the statistical relationship between the brightness temperature and rain-rates (T_B - R). In the standard TMI algorithm, TMI utilizes a Bayesian approach to calculate the probability of the rain rate by comparing the retrieved and observed microwave signals using a hydrometeor profile database (Kummerow and Giglio 1994; Kummerow et al. 2001). However, unlike PR, TMI cannot measure vertical rain structures and, therefore, depends entirely upon assumed vertical cloud structures (Kummerow et al. 2001). TMI has another disadvantage when estimating rain rate over land surfaces due to the noise generated by surface emissions. Therefore, over land surfaces, the TMI algorithm depends entirely on the 85 GHz and 21 GHz bands (Wang et al. 2009).

1.1.2 TRMM PR-TMI rain estimation biases

Due to the aforementioned differences in measuring principles between the active and passive sensors of the TRMM, rain-rate estimation biases exist among the TRMM-derived rainfall products. Therefore, the accuracy of satellite precipitation estimation is subject to its own uncertainties compared to ground-based observations. Various studies have been conducted to identify the differences in TRMM-derived rainfall products on a global scale by directly comparing the precipitation estimates (Berg et al. 2006; Kumar et al. 2009; Gopalan et al. 2010), or by identifying the factors underlying the differences, for example, based on its corresponding precipitation water (Masunaga et al. 2002) and precipitation features (Liu and Zipser 2014).

Several studies have highlighted the fundamental causes of the PR-TMI differences. One of the currently known sources of biases comes from the TMI ice-scattering signals. Higher ice-scattering signals are acquired by TMI at mature to

decaying stages of convection, where the storm top height is maximum with abundant ice particles (Furuzawa and Nakamura 2005). However, these types of events may have low near-surface rain due to a time lag between the processes occurring at the cloud top and the surface (Rajendran and Nakazawa 2005). A comparison study with ground radar data over the United States showed that TMI has a significant overestimation concerning ice particles (Zagrodnik and Jiang 2013). Very high rain-rates are often estimated by TMI at low brightness temperatures particularly below 220 K, while PR shows a less significant relationship between rain-rate and ice scattering signals.

In addition to the global comparison, a large number of regional comparison and validation studies have been conducted to analyze the differences, for example, by comparing against other satellite products, ground radar, and rain gauge data. In general, precipitation estimates from both PR and TMI tend to underestimate ground-based observations (Prakash et al. 2012). However, the above studies indicate significant improvements for the most recent TRMM algorithms (V7), and the global rain estimations by PR and TMI show a better agreement compared to the earlier versions. Nonetheless, the regional-scale differences remain large, which are presumably due to regional variations of climate characteristics affecting precipitation-related processes (Berg et al. 2006).

1.1.3 TRMM PR-TMI extreme-rain biases

Various studies have attempted to explore the origins of the rain-rate differences between PR and TMI, but not many studies were focused on the extreme events, which have a threatening potential to cause severe disasters. The estimation of heavy rain-rates from satellites remains challenging because of the large uncertainties involved in the estimation process. In the PR point of view, Z from the PR sensor in the Rayleigh limit is the sixth moment of the drop size distribution (DSD), which is written as follows:

$$Z = \int_0^{\infty} N(D)D^6 dD$$

where $N(D)$ is the particle size distribution as a function of diameter (D). The above DSD-reflectivity relationship of the 13.8 GHz radar frequency is subject to considerable attenuation when large raindrops are present, as is typical for heavy rainfall events. To correct attenuation, a hybrid method involving the Hitschfeld-Bordan and surface reference technique (SRT) is utilized (Iguchi et al. 2000, 2009). The Hitschfeld-Bordan method produces the best estimate at light rain rates, but it fails for high rain rates. Furthermore, this method often generates higher PIA as an effect of the cumulative error from its vertical profiling. In contrast, SRT can produce better results for heavy rain, but it has no vertical information. In the PR standard rainfall algorithm, the PIA from the Hitschfeld-Bordan method is adjusted with the SRT to obtain optimal estimates. Previous studies have found that precipitation estimation biases derived from the PR arise from the assumptions in the *DSD* and attenuation correction (Iguchi et al. 2009; Kozu et al. 2009; Schumacher and Houze Jr 2000). Some ground validations indicate that the PR often shows rain-rate values that underestimate the heavy rain rates (Henderson et al. 2017; Kirstetter et al. 2013; Zagrodnik and Jiang 2013), especially for convective rains (Iguchi et al. 2009).

In contrast to PR, TMI is less sensitive to the *DSD* assumptions than those from the PR since microwave emission signals depend largely on liquid water path (LWP) regardless of DSD. The 85-GHz TMI brightness temperature channels are more sensitive to ice particles than those at lower-frequency channels. The lower frequency channels (especially at 10 GHz) have their own disadvantages in rainfall estimations due to the beam-filling effect because the footprint is large (Kummerow 1998; Kummerow et al. 2004). In the case of deep isolated rainfalls, the rain-rate might be underestimated since the extreme rain can be averaged out within a footprint. As a result, TMI rainfall biases for deep isolated precipitation systems can be more significant than they would be for PR (Liu and Zipser 2014). Although TMI T_{BS} does not strongly depend on DSD, biases could be generated by DSD assumptions in the conversion from the liquid water contents to rain rates (Masunaga et al. 2002).

The deep convection is known to have tall cloud structures, with low temperatures at the top and large precipitation amounts at the bottom. Theoretically, the stronger and taller the deep convective grows, the more rain it will produce. However, using previous studies involving the PR and TMI comparisons and validations (Berg et al. 2006;

Furuzawa and Nakamura 2005; Shige et al. 2006), more complicated variations heavy rainfall structures have been observed throughout the global tropics. Over tropical land areas, PR tends to detect heavy rain rates with lower storm top heights (STHs) than TMI (Liu and Zipser 2014; Hamada et al. 2015) (Figure 2). The rain with lower STHs identified by PR is likely associated with a more humid environment (Song and Sohn 2015). They also suggest that PR detects extreme warm rain events with significant collision and coalescence processes near the surface. It has been identified that the extreme events could occur in a more stable environment since the higher humidity enhances the graupel production in the mid-troposphere (Song et al. 2017) (Figure 3). The above differences are less significant over ocean than over land. Over the global ocean, TMI identifies greater precipitation areas than PR (Liu and Zipser 2014). It also has been known that TMI tends to produce a higher estimation for the extensive stratiform rain and a lower estimation for the convective rain than those of PR (Henderson et al. 2017) (Figure 4). It is also suggested that the tendency of TMI in detecting the large-scale stratiform rain is related to the beam-filling effect. From the above studies, we could infer that these rain estimation biases in extreme rainfall might be related to specific physical differences in the environmental factors responsible for precipitation formations.

1.2 Objectives and outline of this thesis

Although previous results well characterized the PR-TMI rainfall biases, the reasons why the differences exist were left unresolved. This study is aimed to assess the origins of the biases, particularly for heavy rain events. Identifying the origin of the heavy rain biases could help develop more accurate satellite estimations, which is useful for disaster early warning systems and understanding the future climate. To address this issue, the corresponding cloud structures from CloudSat and the background environmental profiles from ERA-Interim are utilized. CloudSat provides information about cloud droplets-size particles by utilizing a 94 GHz cloud profiling radar (Stephens et al. 2002). CloudSat could provide information about cloud structures, which are not entirely captured by PR. ERA-Interim data are also useful for characterizing the background environmental condition in the extreme rain development. The utilization of CloudSat and ERA-Interim gives detailed background analysis to explain the origin of the biases.

The description of the datasets and explanations of the research methodology are shown in detail in Section 2. Description about the TRMM, CloudSat, and ERA-Interim products utilized in this research is given in Subsection 2.1. Explanation of the methodology to compare the three datasets is shown in Subsection 2.2. An attempt to characterize the TRMM estimation biases in general (climatological) rainfall and extreme rainfall among the products using the Maritime Continent case study is shown in Section 3. General characteristics of the Maritime Continent that possibly influence the biases is explained in Subsection 3.1. Statistical intercomparison of the general rain biases is explained in Subsection 3.2. The climatological biases as a function of probability distribution is explained in Subsection 3.3. The estimation differences under extreme condition are emphasized in Subsection 3.4. The results of the case study are expanded to global ocean and land in Section 4. As an initial introduction to the global differences, the differences between the TRMM general and extreme-rain biases are presented in Subsection 4.1. The comparison of the collocated PR reflectivity profiles and STHs are shown in Subsection 4.2. The comparison of collocated TMI brightness temperature signals is shown in Subsection 4.3. The differences are further examined using the CloudSat and ERA-Interim in Section 5. The CloudSat cloud structures accompanying the PR-TMI differences are shown in Subsection 5.1. The corresponding environmental profiles are shown in Subsection 5.2. The discussion of the differences in the physical processes and their relationships with convective structure organizations are provided in Subsection 5.3. General conclusions of this research are given in Section 6.

TRMM PR (Active Sensor)



TRMM TMI (Passive Sensor)



Figure 1. Illustration of the physical concept differences between TRMM PR and TMI in estimating rain-rates. TRMM PR (left) measures radar reflectivity from large hydrometeor particles, while TMI (right) measure microwave emission from liquid hydrometeor particles and scattering from ice particles (Images from <http://www.eorc.jaxa.jp>).

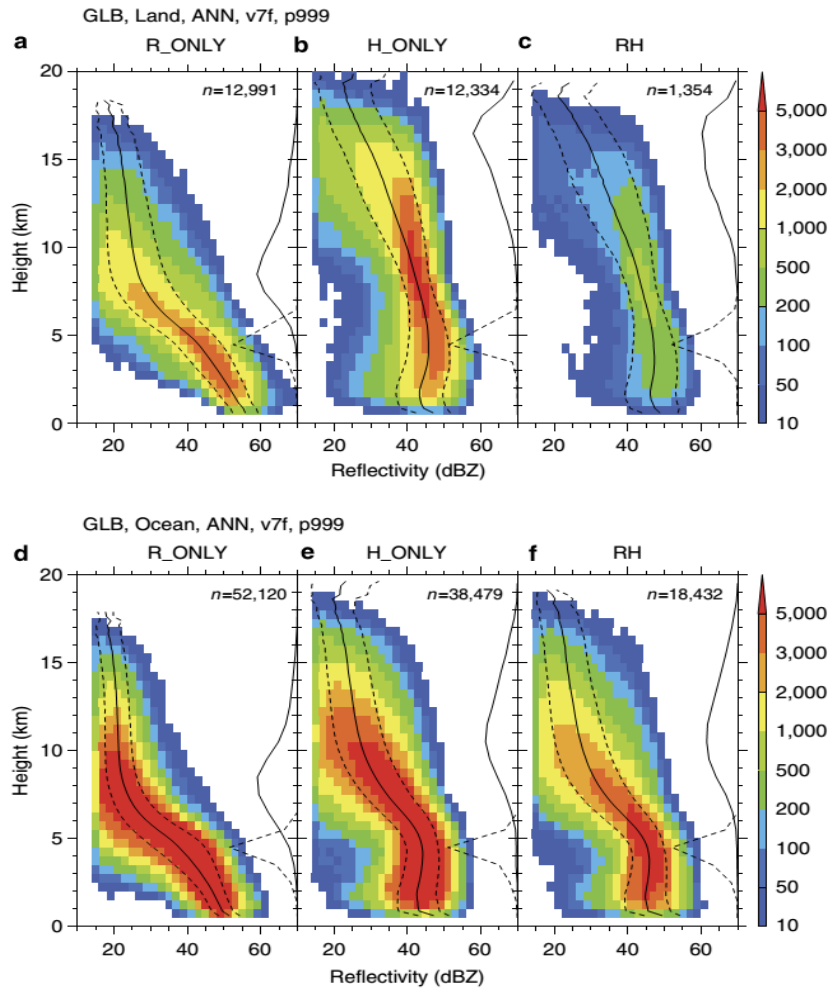


Figure 2. Composite structures of radar reflectivity at extreme pixels within the TRMM observation domain. R_ONLY indicates rain events with PR near-surface reflectivity above the uppermost 0.1%. H_ONLY indicates rain events with PR echo top heights above the uppermost 0.1%. RH indicates rain events with PR near-surface reflectivity and echo top heights above the uppermost 0.1% (Hamada et al. 2015).

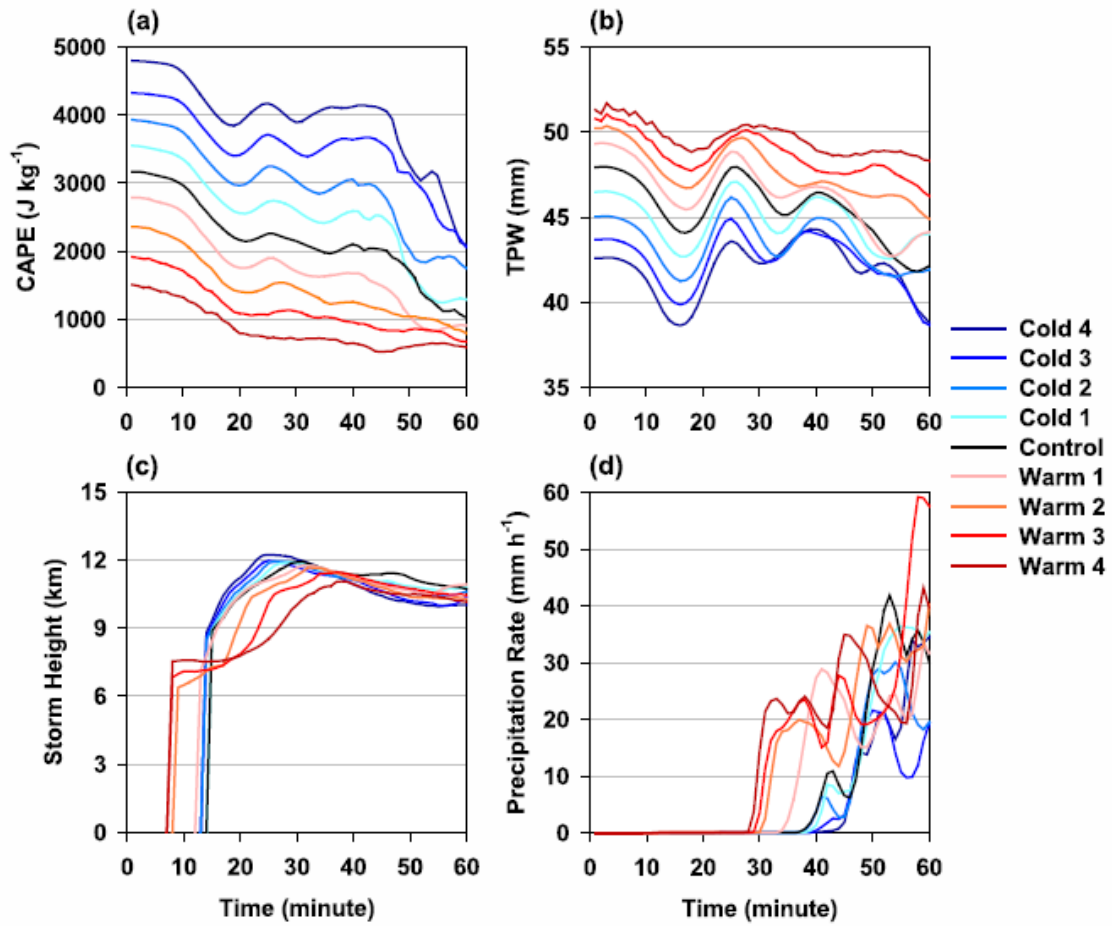


Figure 3. Temporal evolution of (a) Convective Available Potential Energy (CAPE), (b) Total Precipitable Water (TPW), (c) 15 dBZ echo height, and (d) precipitation rate in the idealized experiments. Red lines indicate a warm rain process at moister, but stable environment. Blue lines indicate a cold rain process at less moist, but unstable environment. Cold 1 and Warm 1 experiments was expressed by the observed differences, and increased to 4 times perturbation (Song et al. 2017).

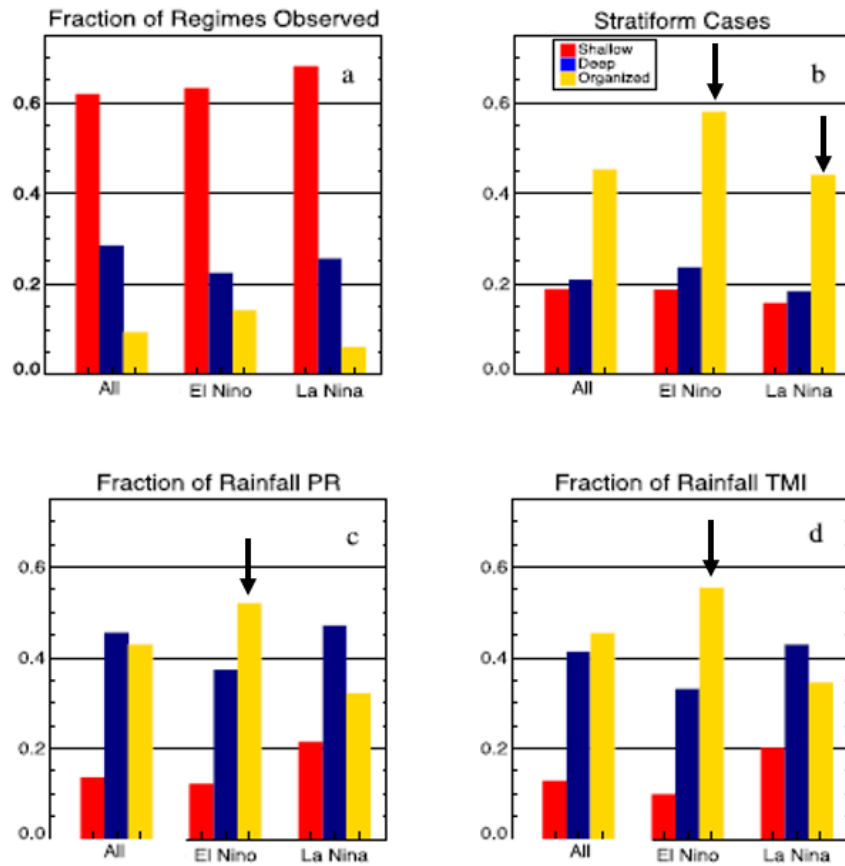


Figure 4. Precipitation regime-based statistics for PR and TMI rain rates for: (a) fraction of precipitation regimes for all years, El-Nino, and La Nina years, (b) the fraction of precipitation regime identified as a stratiform case, (c) fraction of rainfall contributed by each precipitation regime for PR, and (d) fraction of rainfall contributed by each precipitation regime for TMI (Henderson et al. 2017).

2. Data and method

2.1. Data

This study utilizes the TRMM precipitation data from PR and TMI as the core dataset for the comparative analysis. The 94 GHz radar reflectivity data from CloudSat are used to explain the different cloud structures associated with the PR and TMI heavy rainfall events. Several environmental variables from ERA-Interim are used to explain the thermodynamic environments involved in the formation of PR and TMI heavy rainfall events. The description of each dataset utilized in this research is described in this subsection.

The TRMM product used in this research is the version-7 level 2 product. The level 2 product contains the instantaneous precipitation data from TRMM PR and TMI. The PR precipitation dataset analyzed in this work was obtained from the near-surface rain rates from the TRMM PR 2A25 product (NASA 2011a). This product has an approximately 5 km² horizontal resolution at nadir and a 250 km swath width (Iguchi et al. 2000). Three-dimensional rain-rate and corrected reflectivity profiles are utilized in this research. In the 2A25 product, the vertical profiles are stored for every 250 m vertical distance within 80 height bins. The vertical profiles extend from the surface to about 20 km in height. The main data utilized in this analysis is the ‘near-surface rain’ data, which is obtained from the rain profiles above the identified ground clutter. Storm top height (STH) data from TRMM PR 2A23 are also utilized to describe the PR-TMI differences. The STH is defined as the top height of reflectivity profiles above the PR minimum rain-rate detection (> 17 dBZ), which is similar to precipitation top heights.

The TMI precipitation dataset was obtained from the TRMM TMI 2A12 product (NASA 2011b). The horizontal resolution is coarser than that of PR but has a broader swath width than PR (± 850 km) (Kummerow et al. 1998). In the Version 7, TMI surface rain over the ocean is estimated from the Bayesian approach between matched TMI T_{BS} and PR near-surface rain data. The matched PR rain-rates in this version act as a replacement to cloud-resolving model data utilized in the previous versions. This

replacement yields an improvement in the current algorithm. To further examine the details of the differences originating from the emission and ice-scattering patterns obtained by the PMW sensor, the brightness temperature dataset from TRMM TMI 1B11 is also analyzed (NASA 2011c). Slight changes in the original spatial resolution and swath widths due to an orbit boost in 2001 are considered to be negligible for the present purposes. The TMI surface flags from the same product are used to classify the surface types and separate the study area into ocean and land surfaces.

The cloud properties corresponding to the PR and TMI heavy rainfall events are derived from CloudSat, which has operated from 2006 until present. CloudSat carries a 94 GHz Cloud Profiling Radar (CPR) that captures the vertical cloud profiles (Austin et al. 2009; Stephens et al. 2002). Each CloudSat profile contains 125 vertical height bins, which extends from the surface to about 30 km in height. By design, the CloudSat measurements provide only vertical cross-section of clouds along its track with a horizontal resolution of approximately 1.4×1.7 km. This resolution is approximately three times finer than that of TRMM PR. In this analysis, the CPR reflectivity data from the CloudSat-2B-GEOPROF product are used (CloudSat DPC 2017). Cloud flag data stored in the same product are also obtained to classify the cloud/non-cloud states. The rain-type data from CloudSat-2B-PRECIP are also analyzed to classify the observed rain events into convective/stratiform precipitation events. The CloudSat measurements are matched in space and time with the TRMM.

The ERA-Interim data contains atmospheric reanalysis products with a horizontal grid resolution of approximately $0.75^\circ \times 0.75^\circ$ and contains 37 vertical levels, spanning from 1000 hPa to 1 hPa (Dee et al. 2011). The ERA-Interim dataset is available for 1979 until the present (European Centre for Medium-Range Weather Forecasts 2017), which covers the TRMM and CloudSat observational periods. The data are available for four times a day. In this analysis, the air temperature, specific humidity, relative humidity, and vertical velocity data are used to explain the physical processes related to the PR-TMI differences.

2.2 Method

2.2.1 Spatial and temporal coverage of the analysis

The global tropical areas are divided into several domains to identify the regional differences in the PR and TMI estimations of extreme rain events. The regions are further classified into ocean and land subregions. Over the tropical ocean, the domains are divided into the a) Global Tropical Ocean (GlobalTropics), from 180°W-180°E and 15°S-15°N; b) Maritime Continent (MaritimeCont), from 90°E-150°E and 15°S-15°N; c) Tropical West Pacific (WestPac), from 150°E-180°E and 15°S-15°N; d) Tropical Central Pacific (CentralPac), from 130°W-180°W and 15°S-15°N; and e) Tropical East Pacific (EastPac), from 90°W-130°W and 15°S-15°N.

Over the tropical land, the domains were divided into the a) Global Tropical Land (GlobalTropics), from 180°W-180°E and 15°S-15°N; b) Maritime Continent (MaritimeCont), from 90°E-150°E and 15°S-15°N; c) South America (SouthAm), from 45°W-80°W and 35°S-15°N; and d) Central Africa (CentralAf), from 15°E-45°E and 15°S-15°N. The domains are shown in Figure 6. The analysis spans 2006-2014, when TRMM, CloudSat, and ERA-Interim data are all available.

2.1.3 TRMM data processing

Due to differences in area coverage and spatial and temporal resolutions among the three products, a direct comparison among these data is difficult in the original format of each dataset; therefore, a pre-processing routine is required. In this research, we consider the data only in which a PR swath exists, neglecting the TMI data falling outside the PR field of view because the PR swath is narrowest. Since the spatial resolution is approximately 5 km × 5 km for PR and 5 km × 12 km for TMI, a spatial averaging technique should be implemented. First, the precipitation data from PR and TMI are plotted onto a 0.25° × 0.25° grid. All precipitation data points are averaged inside each grid point to represent the grid point rain-rate value. This process ensures that the precipitation biases due to the resolution differences in the original PR and TMI measurements are minimized.

The ocean/land surfaces are determined using the TMI surface flag at the 0.25° × 0.25° grid resolution. In the original resolution, the TMI surface flag is determined to

classify TMI footprint into ocean, land, and coast surfaces. Inside the $0.25^\circ \times 0.25^\circ$ grid resolution, each surface flag is populated. If more than $2/3$ of the grid is dominated by ocean flags within each $0.25^\circ \times 0.25^\circ$ grid box, the grid is classified as an ocean grid. A similar criterion was used for the land grids. Grids that did not meet the above condition represent coast/mixed surfaces and are not considered in this analysis.

The minimum rain rate differs between the TRMM PR and TMI products. The minimum PR echo detectability is approximately 17 dBZ (Iguchi et al. 2000), close to 0.5 mm h^{-1} . The latest version of the TMI algorithm (Version 7) removes the rain/no-rain screening over the ocean and instead provides rain probability parameters, with a minimum detectability of 0.4 mm h^{-1} (Zagrodnik and Jiang 2013). Therefore, in addition to the spatial and temporal differences, there is also a difference in the definition by which each pixel is categorized as rain or non-rain from PR and TMI. There are three main groups of non-rain/rain flag classifications from PR, consisting of no-rain, rain-possible, and rain-certain fields (NASA 2011a). A pixel is classified as rain in PR when its echo exceeds a certain threshold. Furthermore, when the echo is weak but higher than the threshold or when it is possibly influenced by clutter contamination, it is labelled as a rain-possible field. Since the minimum rain rate detectability is approximately 0.5 mm h^{-1} from PR and considerably lower for TMI, we set a higher value than the threshold for determining raining/non-raining grids to avoid ambiguity. In this analysis, we set a threshold of 1 mm h^{-1} to classify raining/non-raining grids.

2.2.3 Extreme rainfall analysis

There are various methods for categorizing non-extreme and extreme rain events. For example, (Hamada et al. 2015) defined the uppermost 0.1% data distribution at each $2.5^\circ \times 2.5^\circ$ grid as extreme events. Furthermore, due to large variations accompanying different classification methods, multiple classification methods to define the extremes, such as fixed thresholds, regional uppermost values, and annual maximum values could be utilized (Kiktev et al. 2003).

In this work, a heavy rainfall event database is constructed by simply taking the uppermost 10% of the rain rates from the data in each grid coordinate. Using the 10% threshold as an extreme criterion rather than using an even higher threshold ensures that

the combined datasets capture a sufficient number of observations. The database contains information about the grid rain rate, the grid center coordinate, the maximum rain rate inside the grid, the geolocations of the maximum rain rates inside the grid, and the recording times of each identified heavy rainfall event.

The TMI brightness temperature data are also gridded following the same rules as the PR and TMI precipitation data. Over the ocean surface, the brightness temperature data from all nine TMI channels are analyzed. Only the brightness temperature data from the 85 GHz vertical and horizontal polarization channels are used for the land surfaces. In this research, ice-scattering signals in the TMI 85 GHz brightness temperature are a proxy of heavy convective rainfall although such signals are more heavily relied upon over land than over ocean. Differences between PR and TMI estimations that are attributed to the ice-scattering signal have also been reported, particularly between deep convection and warm rain events (Nesbitt et al. 2000; Zagrodnik and Jiang 2013). Regarding this issue, we identify the extremes as a function of polarization-corrected brightness temperature (PCT), which is calculated based on the vertically polarized brightness temperature (T_{BV}) and horizontally polarized brightness temperature (T_{BH}) at 85 GHz band (Spencer et al. 1989). The PCT calculation combines the vertical and horizontal polarization T_{BS} to a value which is relative to clear air T_{BS} . The PCT is intended to eliminate the influence of surface emissions. The PCT is calculated following (Spencer et al. 1989), where:

$$PCT = 1.818 T_{BV} - 0.818 T_{BH}$$

2.2.4 CloudSat and ERA-Interim data processing

The combination of TRMM-CloudSat data is achieved by using a similar method to that described by (Masunaga 2012). In this analysis, the precipitation events identified by the TRMM are utilized as the space and time centers to be matched with the CloudSat data (Figure 5). Utilizing the temporal differences between the TRMM and CloudSat data, the precipitation cloud properties before, at, and after extreme events are statistically reconstructed. Although the temporal changes could be easily obtained, identifying the

heavy precipitation clouds at a $0.25^\circ \times 0.25^\circ$ resolution could produce inaccurate results since CloudSat has a very narrow FOV. Therefore, only slices of the TRMM gridded data that overlap with the CloudSat FOV ($1.4 \text{ km} \times 1.7 \text{ km}$) are considered. The coordinates with the maximum rain rates inside each TRMM grid are utilized to ensure that CloudSat captures the center of the heavy precipitation systems. Only grids where the CloudSat coordinates are centered between $\pm 5 \text{ km}$ from the coordinate of the TRMM maximum rain rate are selected. The maximum time difference between the TRMM and CloudSat observations is set to ± 1.5 hours. These strict criteria limit the number of samples from CloudSat to about 80 samples over the land domains (Table 1).

Two-dimensional (horizontal distance-height) composite cloud fractions are constructed to diagnose the PR and TMI extreme precipitation cloud structures. The composite cloud fractions are generated by using a similar method to that described by Igel et al (2014). Clouds are identified using the minimum detected reflectivity threshold of -28 dBZ . Only the single cloud closest to the coordinate of the maximum rain rate inside each grid point are considered when the composite cloud fractions are computed. To further explain the PR and TMI extreme precipitation cloud differences, the convective/stratiform cloud fractions are calculated using the CloudSat rain-type flags. The convective/stratiform ratios are calculated for each 1.5-hour bin for the 6 hours before and after the heavy rain rates were identified by the TRMM.

In contrast to the TRMM instantaneous rain rates, the ERA-Interim dataset has 6-hourly observations with a coarser resolution than the quarter-degree gridded precipitation database. In this analysis, those ERA-Interim grid coordinates nearest to the corresponding TRMM grid are obtained to represent the environmental profiles. Only the ERA-Interim data that fall between 1.5 hours before and after the TRMM extreme events are considered. The potential temperature and specific humidity profiles are then averaged for each ocean/land region. The Convective Available Potential Energy (CAPE) is calculated to explain the relationship between the PR-TMI extreme rain rates with environmental instability. The CAPE represents the maximum energy available to an ascending air parcel, and calculated by using the following equation:

$$CAPE = \int_{LFC}^{EL} g \left(\frac{\theta(z) - \bar{\theta}(z)}{\bar{\theta}(z)} \right) dz$$

where LFC is the level of free convection and EL is the height of the equilibrium level (neutral buoyancy). $\theta(z)$ is the virtual temperature of the specific parcel, $\bar{\theta}(z)$ is the virtual temperature of the environment, and g is the acceleration due to gravity. The CAPE was averaged for each 1.5 hour bin from 24 hours before and after the extreme events observed in the TRMM.

Table 1. Total Number of Observed CloudSat Collocated Profiles for the TRMM rain rate
> the uppermost 10%

Region	Ocean		Land	
	PR	TMI	PR	TMI
GlobalTropics	2092	1703	730	940
MaritimeCont	457	396	103	80
WestPac	339	268	-	-
CentralPac	323	308	-	-
EastPac	175	174	-	-
SouthAm	-	-	432	491
CentralAf	-	-	176	220

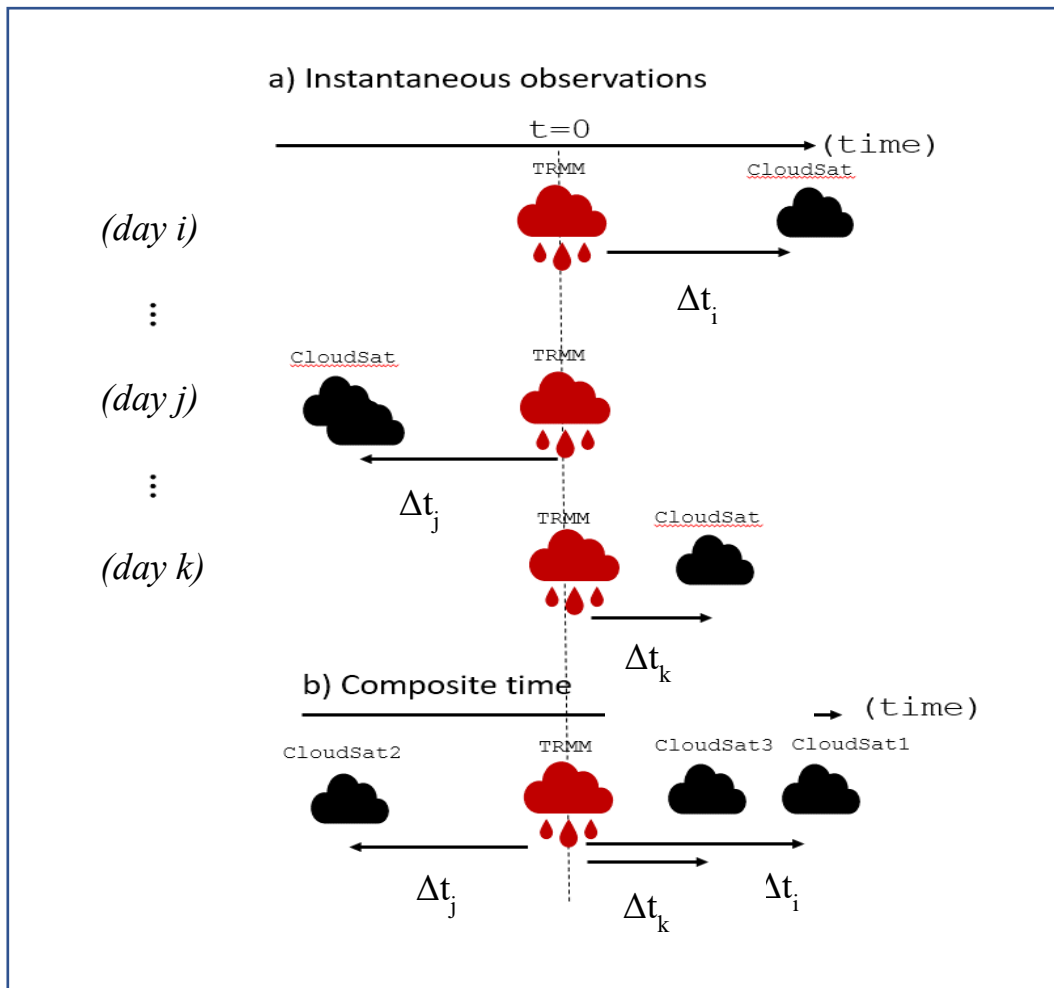


Figure 5. Illustration of the match-up process between the TRMM and CloudSat).

CloudSat composite time series are calculated using time differences between

TRMM and CloudSat observations (Adapted from Masunaga (2012)).

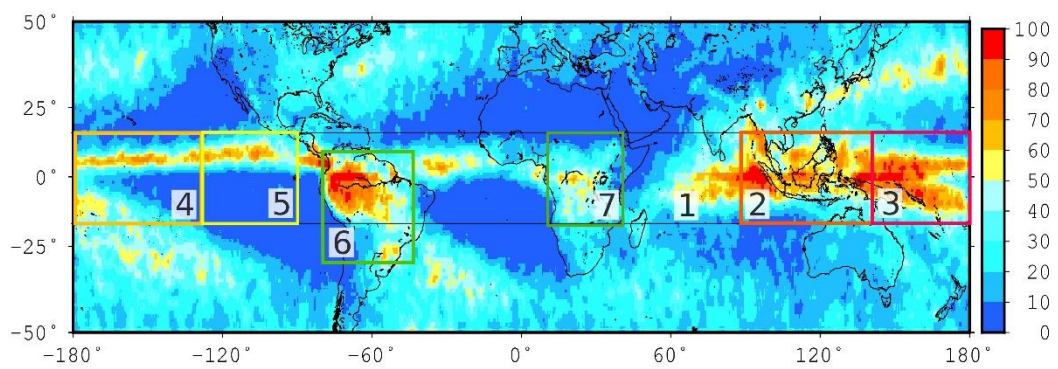


Figure 6. Regional domains in this analysis. Shaded colors show the number of CloudSat deep convective cases over the (1) Global Tropics, (2) Maritime Continent, (3) West Pacific, (4) Central Pacific, (5) East Pacific, (6) South America, and (7) Central Africa.

3. Comparison of TRMM PR-TMI rain estimation biases in general and extreme rainfall: A case study of the Maritime Continent

3.1 The Maritime Continent Heavy Rainfall

In this section, a pilot analysis with focus on the Maritime Continent is conducted to first illustrate the statistical aspects of the inter-product differences in climatological and extreme precipitation. Targeting on a specific area is useful for separating algorithm-specific issues from the regional variability responsible for the algorithm biases. The TRMM TMI often estimate lower rain-rates than the PR over the Maritime Continent, but becomes larger over Eastern Pacific Ocean (Henderson et al. 2017). The above difference is not clearly observed when the global domain is averaged. In this section, the statistical properties from TRMM PR, TMI, and TMPA over the Maritime Continent are presented.

The Maritime Continent (MC), as introduced by Ramage (1968), defines an archipelagic area over the tropics and is primarily characterized as one of the highest precipitation areas on earth (Figure 7). The MC covers a wide area that surrounds Southeast Asian countries between the Indian Ocean and the Pacific Ocean, i.e., Peninsular Malaysia, Singapore, Indonesia, Brunei, Timor, and New Guinea (Qian 2008). Considerable amounts of precipitation occur over the MC due to a combination of complicated environmental factors. One of the most influential components is the existence of warm surface water in the Western Pacific Ocean and the Eastern Indian Ocean, which are labeled as "warm pools" (Ramage 1968). High evaporation rates over these warm pools provide a large moisture supply around the MC, which subsequently becomes a source of precipitation over the area. However, despite the large moisture supply, precipitation over the MC would be less without an enhancement effect from the Southeast Asian Monsoon, which is known as one of the most predominant monsoons in the world (Kripalani and Kulkarni 1997). This monsoon transports moisture from the surrounding ocean directly toward the center of the MC. From December to February, the westerly monsoonal wind dominates and carries abundant moisture from the Indian

Ocean, whereas in June through August, the moisture is primarily transported from the Pacific Ocean (Aldrian and Dwi Susanto 2003; Chang et al. 2005). Large amounts of precipitation frequently occur when large volumes of moisture carried by the monsoon reach close to the islands, transported further to the land particularly during late afternoon, and condensed due to a lifting process as a result of the island's mountainous landform (Mori et al. 2004; Ichikawa and Yasunari 2006). Although there are significant variations due to the local topography, the resulting processes generally yield high precipitation concentrations in the central part of the land (Qian 2008).

The MC's regional characteristics are often described as an area with intense deep convections (Qian 2008). The environmental characteristics specific to the MC are not only responsible for the high annual precipitation, which is approximately 1,500-3,000 mm year⁻¹ over land (As-Syakur et al. 2013), but also the high frequency of extreme precipitation that can trigger hazards over the MC. An analysis of 11 year records of global flood frequency in 1998-2008 conducted by Adhikari et al (2010) shows that Indonesia (which constitutes the largest part of the MC) is listed as one of the top ten countries for the number of flood events. Several studies have aimed to characterize the environmental factors accompanying the extreme events, and these studies indicated that there are various intra-annual and inter-annual factors involved. For example, an analysis of extreme events over Peninsular Malaysia and North Borneo conducted by Salahuddin and Curtis (2011) from 1998 to 2007 revealed that the combination of the South China Sea circulation and the Madden Julian Oscillation (MJO) is a factor that generates the extreme events. The MJO influence was also identified by Tangang et al (2008) in Peninsular Malaysia during flood events in December 2006 to January 2007, where an active phase of the Indian Ocean Dipole (IOD) was also viewed as another factor responsible for the extremes. However, due to a lack of observations, the general mechanism for the extreme precipitation dynamics over the MC is still not fully understood.

3.2 Statistical Intercomparison

As an initial analysis, the three datasets are compared over a range from very light rain to the heaviest rain. A comparison over coast is also conducted to obtain a more detailed

view of the ocean-coast-land differences. Several statistical intercomparisons are conducted for the three datasets, consists of mean rain-rates, rain biases, and root mean squared error (RMSE).

The mean rain rate is computed in two different manners: conditional and unconditional rain rates. The conditional means are calculated with raining grid boxes only (grid with rain rate $> 0.5 \text{ mm h}^{-1}$ while the unconditional means represent the average of all grid boxes irrespective of raining or non-raining. The mean values are obtained separately for different surface types of ocean, land, and coast/mixed surfaces. We also study the potential difference in moderately or extremely heavy rainfall using several rain rate thresholds. Eight thresholds of 0.5, 1, 5, 10, 15, 20, 30, and 40 mm h^{-1} are examined, below which all rain rates are excluded.

A comparison of the unconditional and conditional means for each surface type is presented in Table 2. This table shows that TMPA has the highest unconditional mean compared to PR and TMI for all surface types, that is, 0.21, 0.32 and 0.23 mm h^{-1} for ocean, land, and coast, respectively. In contrast to the unconditional mean, TMPA has the lowest value for any surface type as observed from the conditional mean. TMI tends to produce the highest conditional means compared to PR and TMPA. The TMI conditional mean for land is 2.74 mm h^{-1} and for coast is 2.55 mm h^{-1} , while PR produces the highest conditional mean over ocean (2.41 mm h^{-1}). The differences between PR-TMI conditional means are further investigated based on its original pixel-by-pixel standard deviations within each TMPA grid resolution. The PR standard deviations for ocean, land, and coast are 3.60, 3.87, and 3.82, while TMI standard deviations are 1.67, 2.59, and 2.55. In general, PR yields higher rain-rate variations than TMI within the $0.25^\circ \times 0.25^\circ$ grid resolution. It is possible that rain events detected by PR contain smaller precipitating areas than TMI because the PR swath is narrower than the TMI swath.

To obtain more detailed information than the mean values from all rain rates, it is useful to identify the rain occurrence above specific rain rate thresholds compared to the total number of observations, as shown in Table 3. A comparison of rain frequencies over ocean, land, and coast shows that generally the land surface often has the highest rain frequency. As identified by Qian (2008), this contrast likely results from the strong afternoon heating over land that draws large moisture flux from the ocean, which then condenses into rain in the central part of the islands. The rain rate remaining the highest

over land holds for light rain to heavy rain from $> 0.5 \text{ mm h}^{-1}$ to $> 20 \text{ mm h}^{-1}$. Furthermore, this table also provides support for the previous result related to the large number of very light rain rates identified by TMPA. In this case, TMPA has a higher frequency for very light rain rates ($> 0.5 \text{ mm h}^{-1}$ and $> 1 \text{ mm h}^{-1}$) but decreases to less than PR and TMI for the higher thresholds ($> 5 \text{ mm h}^{-1}$ and above). At the middle to upper range, PR tends to identify a higher number of rain events compared to the other two estimates. The higher PR frequency is particularly found over ocean and coast from rain-rate $> 5 \text{ mm h}^{-1}$ to $> 40 \text{ mm h}^{-1}$ thresholds. In contrast to PR, TMI tends to identify higher rain frequencies for medium to heavy rain over land, from > 10 to $> 30 \text{ mm h}^{-1}$. Although this table can define the general characteristics of rain frequencies, a closer look at each specific rain rate is required. A detailed analysis was obtained by further elaboration with a more comprehensive statistical analysis based on cumulative contribution, as presented in the next part.

Second, differences in the rain-rate estimation is assessed in further detail between each pair among the three products, that is, PR-TMI, PR-TMPA, and TMI-TMPA. Absolute non-rain events, in which both of the values are equal to $\leq 0.5 \text{ mm h}^{-1}$ are excluded from the analysis. The dissimilarities between the first and second data from each pair is computed to identify a positive or negative difference value. This positive (negative) difference value implies that a higher (lower) rain rate estimation exists from the first data to the second data in a pair based on the following function:

$$D = \frac{1}{n} \sum_i R_{xi} - R_{yi}$$

where D is the difference values, n is the total number of data, R_{xi} and R_{yi} are the first and second data in each pair, and i denotes the individual data samples.

A few additional analyses of the difference values are conducted to account for the fact that rain screening is not homogeneous across the three products. Following Habib et al (2009) and Zagrodnik and Jiang (2013), we calculate the hit signal difference (HD), miss signal difference (MD), and false signal difference (FD). The HD is calculated when both the first and the second data in a pair contain a finite rain rate within the same grid box:

$$HD = \frac{1}{n} \sum_i R_{xiH} - R_{yiH}$$

where HD is the hit signal difference and R_{xiH} and R_{yiH} are the first and second rain data samples for $R_{xiH} > 0$ and $R_{yiH} > 0$. The MD is calculated with the samples where the first data misses the rain events detected by the second data in a pair.

$$MD = \frac{1}{n} \sum_i R_{yiT}$$

where MD is the miss signal difference and R_{yiT} is the second data samples for $R_{xi} = 0$ and $R_{yi} > 0$. FD is defined as the inverse to the MD:

$$FD = \frac{1}{n} \sum_i R_{xiT}$$

where FD is the false signal difference and R_{xiT} is the first data samples for $R_{xi} > 0$ and $R_{yi} = 0$.

Subsetting each data pair only for the HD component, the conditional root mean square difference (RMSD) is calculated and decomposed into its systematic and random differences (Habib et al. 2009; Zagrodnik and Jiang 2013):

$$RMSD = RMSD_s + RMSD_r = \sqrt{\frac{1}{n} \sum_i (R_{xi} - R_{yi})^2}$$

where $RMSD_s$ is systematic difference, $RMSD_r$ is random difference, and n is total number of each data in a pair with rain rate $>0.5 \text{ mm h}^{-1}$. The systematic error is extracted by linear regression as:

$$RMSD_s = \sqrt{\frac{1}{n} \sum_i (R'_{xi} - R_{yi})^2}$$

where $R'_{xi} = a + b \times R_{yi}$ and a and b are the regression constants.

Finally, the exceedance probability distribution is utilized to assess the inter-product differences in extreme rainfall. The exceedance values represent the occurrence probability at or above a certain rain rate, following the formula:

$$P = m/(n + 1)$$

where P is the exceedance probability, m is the data rank ordered from the highest rain rate to the prescribed threshold of rain rate, and n is the total number of each data.

The result of difference value analysis (HD, MD, and FD) are presented in Table 4, while the RMSD between each pair of products is shown in Table 5. Both of the analysis show that PR-TMI often produce the largest difference compared to the other data pairs, regardless of surface types. The PR-TMI high MD and FD imply that the majority of the differences are closely related to the non-rain and rain classifications by each product. Based on the conditional RMSD, TMI-TMPA is the smallest in the total RMSD for all three surfaces (1.36, 1.92, and 1.95 mm h⁻¹ for ocean, land, and coast, respectively). However, the systematic component of the RMSD shows that the difference between PR and TMPA is smaller over ocean and coast.

3.3 Rain rate probability distribution

This section presents an analysis of the probability distribution of rainfall in terms of cumulative probability, exceedance probability, and mean rain-rates as a function of the TMI 85 GHz PCTs. The first result, shown in Figure 8, provides the cumulative probability contribution among the three data sets. The main feature is that PR provides the smallest contribution to low and medium rain rates compared to the TMI and TMPA. The contribution of rain rate from the minimum up to 10 mm h⁻¹ is approximately 70-80% for PR, while higher contributions are achieved by TMI and TMPA in the same

range. The TMPA's cumulative contribution is higher than PR and TMI for any given rain-rate value, particularly over ocean and land. The higher cumulative contribution is possibly generated by a large number of light rain events, which are responsible to the TMPA's low conditional means shown in Table 2. The TMI contribution, when compared to the TMPA, shows a similar pattern. However, the TMI has a smaller contribution than the TMPA for low to medium rain rates, particularly over land. The TMI contribution is approximately 80% at 10 mm h^{-1} over land, which is close to PR. Over coast, the TMI contribution is consistent with TMPA.

The exceedance probability is presented in Figure 9. The result indicates that PR generally produces a higher exceedance probability than TMI and TMPA over ocean and coast. This result provides an explanation for Table 3, where PR identifies a higher number of rain events $> 10 \text{ mm h}^{-1}$ and $> 20 \text{ mm h}^{-1}$ over ocean and coast than the other two data sets, while TMI is higher over land. It appears that the TMI land algorithm produces a higher exceedance probability than PR between $10\text{-}25 \text{ mm h}^{-1}$. However, the TMI exceedance probability rapidly decreases after $> 25 \text{ mm h}^{-1}$. This result is further examined in Section 5.

Figure 10 shows a comparison of the mean rain rate as a function of TMI 85 GHz PCT. Over land, all of the algorithms produced similar results when TMI 85 GHz PCT $> 200\text{K}$, while for lower PCTs, TMI tends to show higher rain rates than the other two data sets. The higher TMI rain rate below 200K PCT is also observed over coast, but the spread occurs at lower PCT (at approximately 160K). This spread presumably explains why TMI exhibits a higher frequency of rain events for a rain rate of $> 10 \text{ mm h}^{-1}$. It could be implied that the higher exceedance probability of TMI over land shown in Figure 9 is due to the frequent rain events with PCTs below 240K . The excess of TMI rain for low PCTs is not observed over ocean, which may be expected because the TMI land algorithm relies entirely on the ice-scattering channels.

3.4 Comparison of Extreme Rainfall

The previous result in Figure 10 shows that the ice scattering may not be tightly linked to the surface rainfall. In particular, the TMI land algorithm is known to being insensitive to light rain without ice particles (Furuzawa and Nakamura 2005; Rajendran and Nakazawa

2005; Zagrodnik and Jiang 2013). The apparent inconsistency between the exceedance probability plot (Figure 9b) and rain rate-PCT plot (Figure 10b) over land is further investigated in this section. Figure 11 presents a two-dimensional histogram of rain rate and TMI PCT. The relationship between rain rate and PCT is broadly spread except for the TMI land and coast, in which the rain rate is tightly correlated with PCT. This result is likely because the TMI land and coast algorithms do not rely on the emission channels. Although the mean rain rate as a function of PCT (shown as black plus signs in Figure 11) indicates that the TMI land and coast algorithms are higher than PR and TMPA at an intermediate rain range, the histogram shows that the TMI rain-PCT curve over land and coast rarely contains rain rates higher than 20 mm h^{-1} except at the lowest PCTs. However, PR rain can exceed 20 mm h^{-1} over a wide range of PCTs over the three surfaces.

Figure 12 shows the PCT-rain relation as plotted in Figure 10 but calculated from the samples limited to the uppermost 1% rain rate for each 5K PCT bin. The uppermost 1% is selected in this analysis rather than the uppermost 10% to capture the highest value in the PCT distribution. PR consistently has the highest rain rate for all PCTs over land and coast compared to TMI and TMPA. This result is in contrast with the mean rain rate-PCT plot presented in Figure 10, where TMI is the highest over land for an intermediate range of rain rates compared to the two other data sets. Comparison of the two figures shows that there are differences related to the range of the data distribution inside the TMI land algorithm, especially between the mean and the uppermost values as a function of PCTs.

A remaining question is, as shown in Figure 11, why are the heaviest rains detected by PR not necessarily associated with the lowest TMI PCTs? To address this question, we examine the storm top heights from collocated PR 2A23 associated with extreme rain rates of the uppermost 1% for each 5K PCT bin in Figure 13. The result indicates that PR, TMI, and TMPA could produce comparable results over ocean. As identified by the three estimates, the storm top height is approximately 6 km at 10 mm h^{-1} to approximately 8-10 km at 30 mm h^{-1} over ocean. However, it appears that TMI yields a higher storm top height for any given rain rate over land and coast compared to PR and TMPA. Over land, TMI indicates storm top heights of approximately 8 km at 10 mm h^{-1} to 12 km at 30 mm h^{-1} . The extreme events derived from PR and TMPA, in contrast, exhibit lower storm top heights over land: approximately 5 km at 10 mm h^{-1} to

10 km at 30 mm h⁻¹. Because TMI does not directly observe surface rain rates but rather relies on the empirical relationship with ice-scattering signals, this relationship may be somewhat too exaggerated (i.e., excessive ice scattering for a given surface rain rate) for extreme rainfall.

The relation of surface rain with PCT is further examined in terms of vertical rain profiles. Figure 14 shows the PR vertical rain profiles averaged within the extreme subset identified by PR (red), TMI (green), and TMPA (blue) while considering the PCT values. The plots are categorized into four PCT ranges: <160K, 160-200K, 200-240K, and >240K. Over ocean, the vertical profiles agree well among the three products for all PCT ranges. At the lowest 85 GHz PCTs (<160K), the near surface rain reaches approximately 22-23 mm h⁻¹. The near surface rain rates are decreasing at higher PCTs: approximately 15 mm h⁻¹, 10 mm h⁻¹ and 3 mm h⁻¹ for 160-200 K, 200-240K, and >240K PCTs, respectively. Over land, the vertical rain profiles disagree among the products compared to the ocean. The PR-identified extreme rain profiles exhibit a significant increase in rain rate from 5 km to near the surface. In contrast, such a downward increase is more modest for the TMI-identified extremes. This PR-TMI difference resulted in the TMI's lower near surface rain. For PCTs <160K, the near surface rain rate is approximately 12-13 mm h⁻¹ when extremes are defined by PR, while the surface rain rate reaches only approximately 10 mm h⁻¹ for the TMI sorted subset. This kind of difference is also found for PCTs of 160K-200K and 200K-240K. Comparison of the vertical rain profiles over coast also indicates similar differences to those over land.

3.5 Discussion and Summary

The results of this study highlight the properties of different rain rate estimation among PR, TMI, and TMPA over MC for both non-extreme and extreme cases using long-term data records from 1998-2014. The results revealed that the rain rate in general and in the extreme cases has its own characteristics attributed to the differences. 1) For the non-extreme rain events (below 10 mm h⁻¹), TMI and TMPA have a higher probability of detection than PR over the three surfaces. 2) For moderately heavy rain events (between 10-25 mm h⁻¹), the TMI algorithm over land detects more frequent rain events than PR and TMPA. 3) However, the detected extreme events from TMI land algorithm decreased

at above 30 mm h⁻¹. Further analysis shows that The TMI extreme events are heavily accompanied with the strongest ice-scattering signals and highest storm top heights, while the PR extremes show a weaker relationship between the three variables.

The PR-TMI differences in representing the uppermost 1% extremes highlights the known weakness in the TMI land algorithm. The TMI land estimates depend on the existence of ice particles aloft in precipitating clouds since it assumes a tight relationship between ice-scattering signals and surface rain rates. Heavy rain events are generally associated with stronger convection, which contains ice particles aloft. However, it has been shown that the rain rate-ice scattering relationship is not always robust. Very intense rain events identified by PR are not associated with the highest storm top height and are thus unlikely with most grown ice particles aloft. The comparison with the exceedance probability provided in the previous section indicates that higher extreme events are not necessarily accompanied by extreme ice-scattering signals, similar to Hamada et al (2015), while the TMI land algorithm by design always predicts the heaviest rains from the lowest PCT. The factors contributing to the higher PR extremes are now under investigation.

There are several remarks related to this study. First, despite the PR-TMI extreme contrast over land, it appears that both estimates are statistically consistent over ocean, which is possibly due to the utilization of the TMI emission channels. However, a more detailed comparison shows that the PR and TMI differently identify extreme events over ocean, as explained in the next section. Second, although TMI often provides similar results as TMPA for light rain rates, there are large estimation differences for medium to heavy rain events, particularly over ocean and coast. Comparison of the uppermost 1% for each 5K PCT bin yields higher conformity between PR and TMPA in terms of ice-scattering signals, storm top heights, and vertical rain profiles. However, the results also suggest that extreme events from both of the data are not quite similar, although TMPA tends to provide rain estimates between PR and TMI. The main reason for this difference is still unclear. It is possible that the temporal mismatch between instantaneous PR rainfall and 3-hourly snapshot rain data from TMPA may have a significant contribution to this condition (Prakash et al. 2012). Further, since the extreme cases are selected from 1% of the upper distribution, the large number of very light rain events from TMPA could also introduce a bias to the 1% threshold, which determines the extremes. Changing the 1% extreme threshold into a higher specific value does increase the TMPA extreme means.

However, a similar comparison using two specific thresholds (10 mm h⁻¹ and 15 mm h⁻¹) shows no significant differences in the extreme properties, particularly the vertical rain-rate profiles.

Table 2. Total number of grid boxes (including non-raining grids), unconditional mean (average of all grid boxes $\geq 0 \text{ mm h}^{-1}$), and conditional mean (average of all grid boxes for $> 0.5 \text{ mm h}^{-1}$) based on each surface type.

Data-set	Total number of grid			Unconditional mean			Conditional mean		
	Ocean	Land	Coast	Ocean	Land	Coast	Ocean	Land	Coast
PR				0.19	0.28	0.20	2.41	2.55	2.48
TMI	66.14%	11.09%	22.77%	0.17	0.26	0.14	2.04	2.74	2.55
TMPA				0.21	0.32	0.23	1.97	2.40	2.41

Table 3. Percentage of grid boxes for rain rate $> 0.5 \text{ mm h}^{-1}$ to $> 40 \text{ mm h}^{-1}$ based on each algorithm and surface type. Surface maximums are displayed in bold font.

Threshold	Surface	% of total data		
		PR	TMI	TMPA
$> 0 \text{ mm h}^{-1}$	Ocean	8.0149	8.2439	10.8422
	Land	10.9565	9.3488	13.1510
	Coast	8.1611	5.4697	9.3435
$> 1 \text{ mm h}^{-1}$	Ocean	5.0773	4.81	6.7406
	Land	7.5153	6.8109	9.0515
	Coast	5.4264	3.8474	6.2759
$> 5 \text{ mm h}^{-1}$	Ocean	0.9077	0.6744	0.7026
	Land	1.3362	1.2065	1.3944
	Coast	0.9631	0.6585	1.0307
$> 10 \text{ mm h}^{-1}$	Ocean	0.2329	0.1208	0.1173
	Land	0.3019	0.3731	0.2833
	Coast	0.2380	0.1393	0.2133
$> 20 \text{ mm h}^{-1}$	Ocean	0.0335	0.0167	0.0089
	Land	0.0392	0.0468	0.0217
	Coast	0.0272	0.0152	0.0226
$> 30 \text{ mm h}^{-1}$	Ocean	0.0060	0.0048	0.0019
	Land	0.0041	0.0055	0.0026
	Coast	0.0051	0.0020	0.0035
$> 40 \text{ mm h}^{-1}$	Ocean	0.0013	0.0011	0.0005
	Land	0.0007	0.0004	0.0006
	Coast	0.0012	0.0002	0.0007

Table 4. Cross matrix of hit, miss, and false signal difference of rain rate between each pair out of the three algorithms (in mm h⁻¹). The results are classified based on each surface type from left to right. The hit difference (HD), miss difference (MD), and false difference (FD) are shown from top to bottom. The highest difference for each surface is displayed in bold font.

		Ocean		Land		Coast	
		TMI	TMPA	TMI	TMPA	TMI	TMPA
Hit bias	PR	0.43	0.09	0.09	-0.05	0.63	-0.05
	TMI	-	-0.330	-	-0.20	-	-0.77
Miss bias	PR	-0.88	-0.92	-1.37	-1.22	-1.27	-1.21
	TMI	-	-0.82	-	-1.06	-	-1.44
False bias	PR	0.90	0.79	1.22	0.86	1.33	0.87
	TMI	-	0.61	-	0.74	-	0.73

Table 5. Cross matrix of conditional root mean square differences (RMSD_s) and the contribution of systematic RMSD_s (in mm h⁻¹) between each algorithm (for rain rate > 0.5 mm h⁻¹). The highest RMSD at each surface is displayed in bold font.

		Ocean		Land		Coast	
		TMI	TMPA	TMI	TMPA	TMI	TMPA
RMSE	PR	2.01	1.62	2.67	1.98	2.57	2.00
	TMI	-	1.36	-	1.92	-	1.95
RMSE _s	PR	0.35	0.29	1.35	0.57	1.04	0.61
	TMI	-	0.44	-	0.49	-	1.19

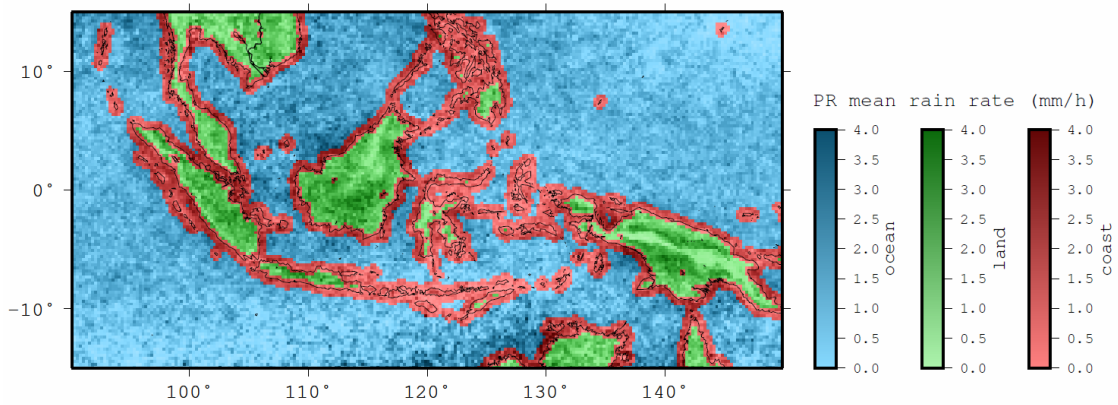


Figure 7. Map of the Maritime Continent with classified surface types based on the TMI 2A12 surface flag. Dark shaded colors represent higher mean rain rates from the PR 2A25 near surface rain averaged from 1998-2014.

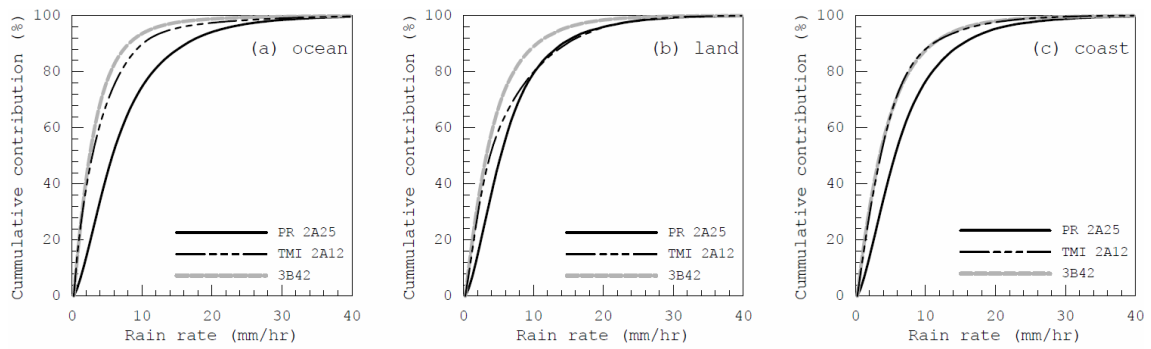


Figure 8. Cumulative contribution to mean rain rate (%) from PR (solid black line), TMI (dashed black line), and TMPA (dashed gray line) for (a) ocean, (b) land, and (c) coast, calculated from each 0.25° square grid from 1998-2014.

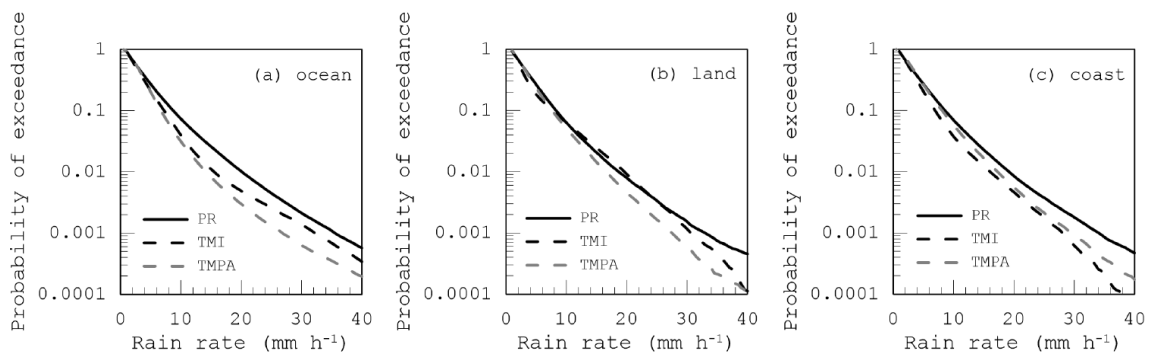


Figure 9. Probability of exceedance for PR (solid black line), TMI (dashed black line), and TMPA (dashed gray line) based on each 0.25°square grid from 1998-2014. A rain rate with corresponding exceedance value close to 1 indicates a higher probability to occur. The plots represent each surface from left to right: (a) ocean, (b) land, and (c) coast.

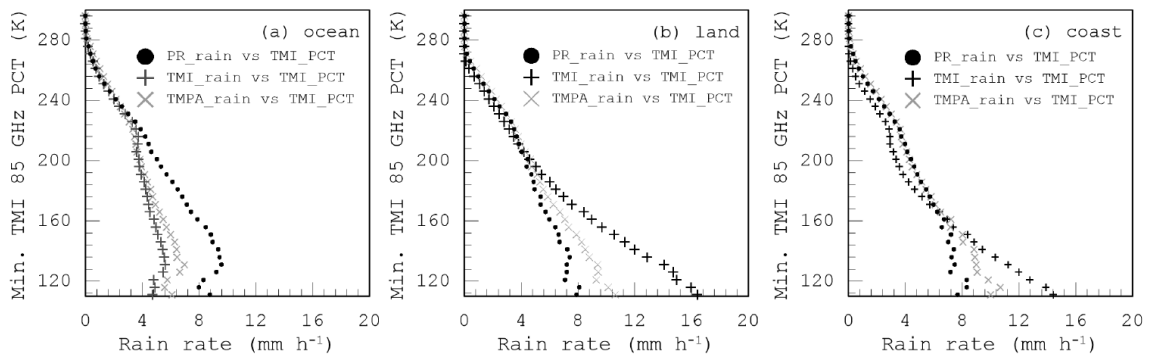


Figure 10. Plots of TMI minimum 85 GHz PCT versus averaged rain rate from PR (black dot sign), TMI (black plus sign), and TMPA (gray x). The PCT values are obtained from the minimum value inside collocated $1/4^\circ$ square grid boxes from 1998-2014. Each point represents the mean value for a 5 K PCT bin. The result is classified to three surface types from left to right: (a) ocean, (b) land, and (c) coast.

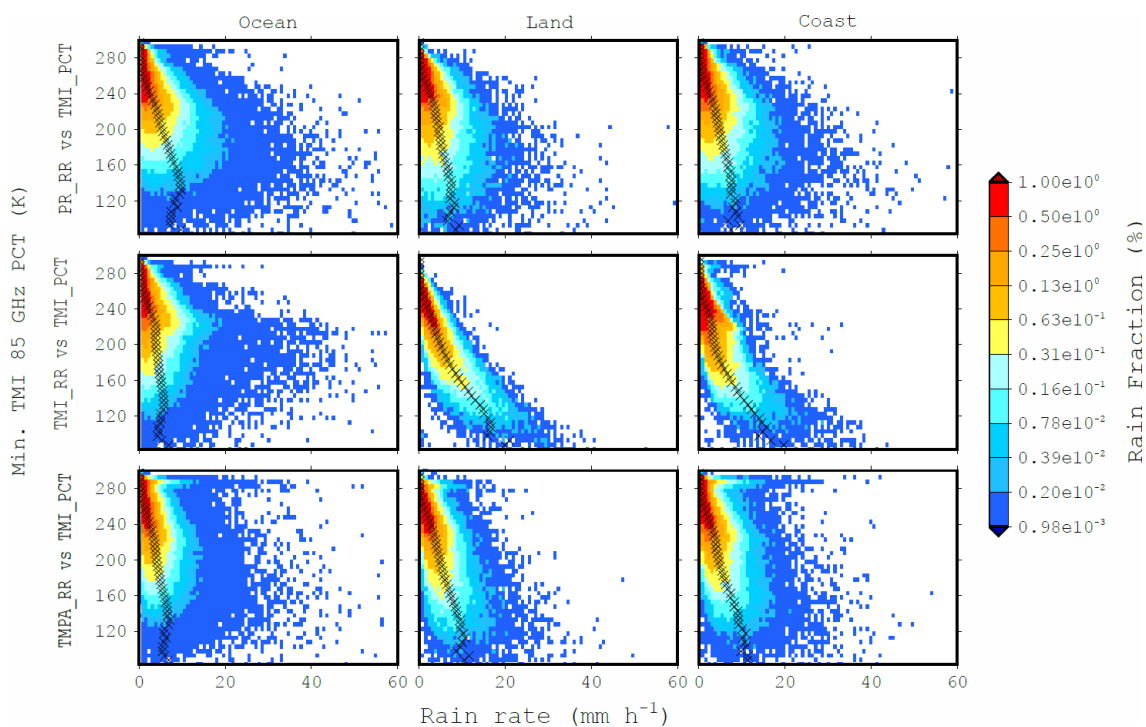


Figure 11. Fraction to the total number of rain events as a function of rain rates and TMI minimum 85 GHz PCTs, obtained from collocated $\frac{1}{4}^\circ$ square grid boxes from 1998-2014. The data are classified based on the algorithms (from top to bottom: PR, TMI, and TMPA) and surface types (from left to right: ocean, land, and coast). The scale represents fractions of the total data for each plot.

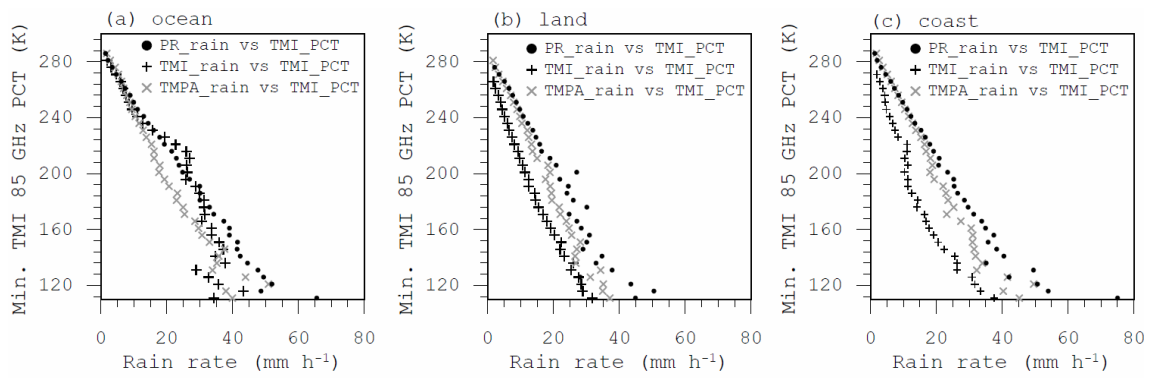


Figure 12. Similar to Figure 10 but for the average of the uppermost 1% rain rate at each 5 K 85 GHz TMI minimum PCT bin.

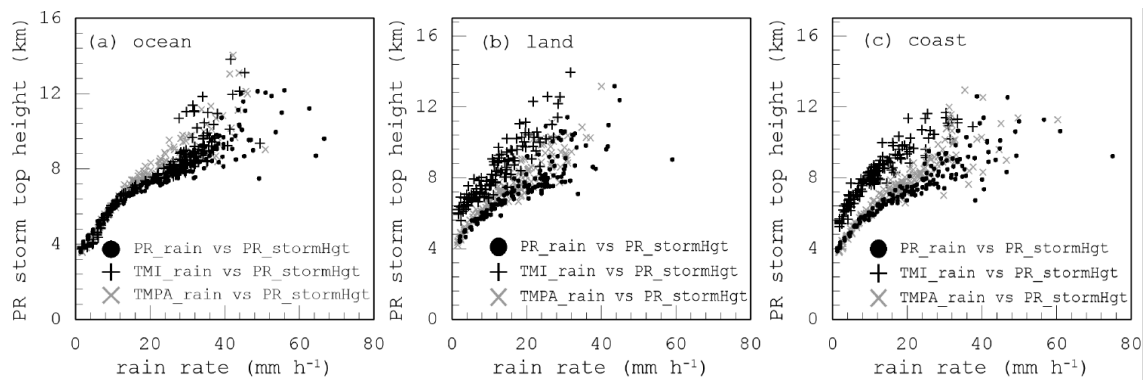


Figure 13. Plots of collocated PR storm top height as a function of the uppermost 1% rain rates at each PCT bin from PR (black dot sign), TMI (black plus sign), and TMPA (gray x). The uppermost 1% are obtained using TRMM observations from 1998-2014. The storm top height data are obtained from the average value of collocated PR2A23 at $\frac{1}{4}^\circ$ square grid boxes and classified to ocean (left), land (middle), and coast (right).

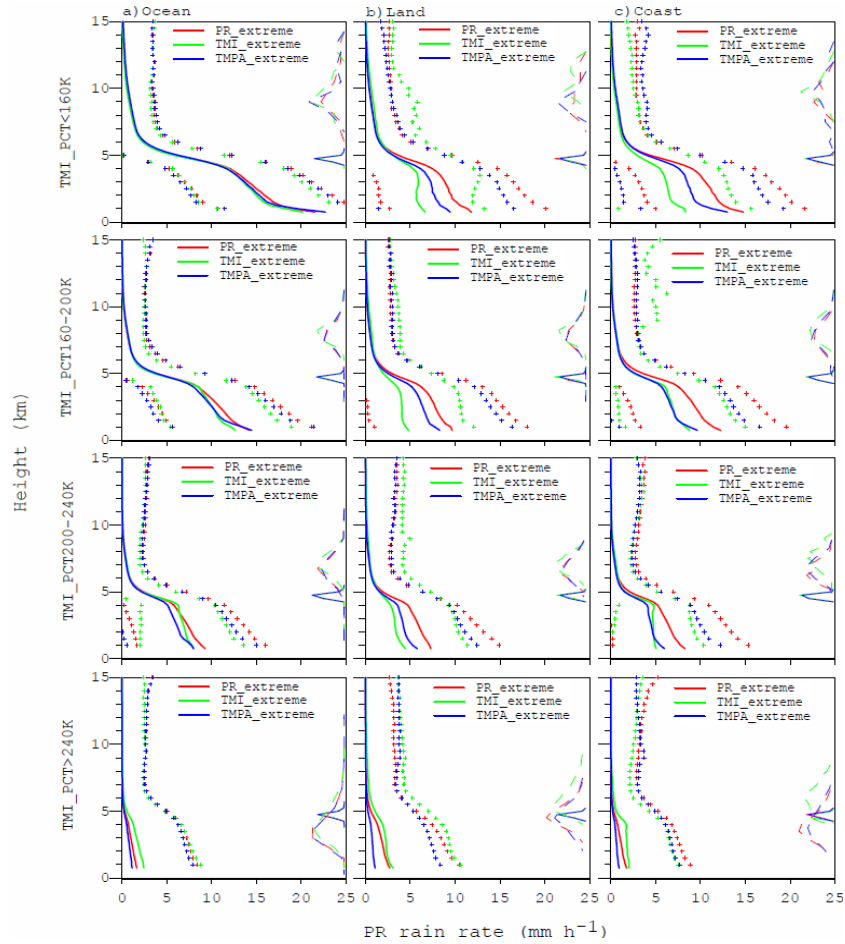


Figure 14. Collocated PR2A25 vertical rain rate mean for PR uppermost 1% extremes (red), TMI uppermost 1% extremes (green), and TMPA uppermost 1% extremes (blue), as classified by four TMI minimum 85 GHz PCT ranges (<160 K, 160K-200 K, 200K-240 K, and >240 K) from top to bottom, and ocean, land, and coast from left to right. The uppermost 1% are obtained using TRMM observations from 1998-2014. Cross signs indicate 95% confidence interval. Solid color lines on the right represent the corresponding freezing heights, while dashed color lines represent the corresponding PR2A23 storm top heights.

4. TRMM PR-TMI regional extreme-rain biases and its difference in the retrieval process

4.1 A global view of TRMM PR-TMI climatological and extreme-rain estimation biases

The previous section presented a case study of TRMM inter-product biases in climatological and extreme-rain biases over the Maritime Continent. One might wonder whether the present statistics from the Maritime Continent precipitation are also representative of global rainfall characteristics. To address this question, this section gives the explanation of the differences of TRMM PR-TMI general rain biases and the extreme-rain biases over the tropical ocean and land domains across the globe. To compare the general biases against the biases specific to extreme rain, the general rain-rates differences are first described. The general differences are taken using unconditional rain-rate from the PR and TMI. The TMPA is not included in the analysis to follow, because the error sources in the TMPA rainfall are rather complicated to interpret, while the PR and TMI products offer illustrative descriptions of the algorithmic issues intrinsic to each TRMM instrument. The results are then compared with the extreme-rain biases using the uppermost 10% from the rain-rate database. The 1% threshold adopted in the previous section is increased to 10% from now on, because the TRMM matchups with cloudSat orbits are so rare that the definition of extreme events must be relaxed to ensure the statistical robustness.

The general differences between TRMM PR and TMI in estimating rainfall over the tropics are shown in Figure 15. The figure shows that both the PR and TMI similarly identify a number of regions with higher rain-rates than the average. The regions are for example the Maritime Continent, Central Africa, South America, and ITCZ path over the Pacific Ocean. Although the PR and TMI identify a similar pattern, biases in rain-rate estimation still exist. The comparison of the PR-TMI general biases is shown in Figure 15c. The figure shows that there are regional biases between the PR and TMI among several tropical land and ocean regions.

Over the tropical ocean, the PR identifies higher rain-rates than the TMI over the Maritime Continent, Indian Ocean, and East Atlantic Ocean. However, it identifies lower rain-rates than the TMI over the East Pacific Ocean and large descends areas close to the subtropics. Over the tropical land, the PR identify higher rain-rates than the TMI over the Maritime Continent and the north part of Amazon Basin. In contrast, the PR identifies lower rain-rates than TMI over Central Africa and south part of The Amazon Basin. A similar result has been identified by Liu and Zipser (2014) using the TRMM level 3 products.

A comparison of the PR-TMI extreme-rain biases is shown in Figure 16. The figure shows a different pattern identified by the PR and TMI. The PR identifies higher rain-rates over some ocean domains than the TMI. The PR pattern is similar to the unconditional mean rain-rates. The higher rain-rates following ITCZ path are not clearly observed from TMI. Over the tropical land, the PR estimates higher rain-rates than the TMI in contrast to the general rain biases. The comparison of PR- TMI extreme-rain biases are shown in Figure 16c. The result shows that the PR identifies higher extreme rain rate over the entire tropical ocean. Over South America, the PR dominantly identifies higher rain-rates compared to the TMI. While over Central Africa, the PR identify higher extreme rain-rates over the central part. However, the TMI somehow identifies higher rain-rates near the Saharan Desert.

The differences between PR and TMI biases for general rain-rates and extreme rain-rates shown in the previous figure give an example how the extreme-rain biases could be different from the general rain events. Over the entire tropical ocean domains, the PR identifies higher rain-rates than the TMI, while the unconditional mean shows a variation between both the datasets. Over the tropical land, the estimation biases in extreme rainfall are also different than the general rain estimation biases. Over South America, the PR becomes more dominant in identifying higher rain-rates than the TMI, while the unconditional biases show a difference between the northern and southern parts. Over Central Africa, the areas where TMI identify higher rain-rates for the unconditional mean are shifted to the PR in the case of extreme.

The differences between the PR-TMI rain estimation biases in general climatology and extreme events over both ocean and land are closely related to its rain-rate distribution. Liu and Zipser (2014) show that both over the tropical ocean and land,

the PR identifies a larger number of events than TMI for the upper-end of the rain rate distribution. To identify the regional variation of the PR-TMI extreme-rain biases as a function of rain-rate distribution, an analysis of rain-rate contribution is presented in this section. Figure 17 shows the regional variation of rain-rate contribution over the tropical ocean domains. The result shows that there are several differences between the PR and TMI in term of rain-rate contributions. For low to medium rain-rates, approximately below 10 mm h^{-1} , the TMI identifies higher contributions than the PR. The TMI rain contribution from the minimum up to 10 mm h^{-1} is approximately 70% for all of the regions, but lower for the PR. On another hand, the PR identifies a larger contribution for higher rain-rates, especially above 15 mm h^{-1} .

Comparison of the rain-rate contribution over the land domains is shown in Figure 18. The result, in general, indicates distinctive properties compared to the ocean domains. Although there are variations in the low to medium rain-rate contribution ($< 10 \text{ mm h}^{-1}$), the TMI tends to estimate higher contribution for moderate extremes ($10\text{-}20 \text{ mm h}^{-1}$). For the heavier rain-rates ($> 20 \text{ mm h}^{-1}$), the PR again identify a larger number of extreme events than the TMI. The differences between general and extreme-rain biases therefore related to the rain-rates ranges in which they are examined. For example, over Central Africa, the TMI estimates higher unconditional rain-rates since it identifies a higher number of moderate extreme rains in this region. However, when these values are excluded, the PR estimates higher rain-rates than the TMI.

4.2 Regional comparison of the diurnal cycle

In this part, comparison of the PR-TMI differences in term of diurnal cycle is conducted to initially identify the retrieval process differences. Yamamoto et al (2008) show that there is a time shift in the diurnal cycle between the PR and TMI in detecting rain peaks over land. The PR tends to detect earlier rain peaks than the TMI since it detects near surface rain. The TMI, on another hand, detect the maximum deep convection and solid hydrometeors during the mature stage, which occurs after PR rain peaks. This difference leads to higher number of stratiform precipitation observed by the TMI than the PR.

To detect how the PR and TMI behave in detecting heavy rains, a similar method conducted by Yamamoto et al (2008) are presented in this research. First, we focus on the

general rain differences over the ocean domains, as shown in Figure 19. Collocated TMI 85 GHz PCTs are also plotted to characterize the climatological and extreme differences. The climatological plots show that although the PR and TMI show a conform diurnal pattern, the TMI identifies rain events are associated with weaker ice-scattering signals than the PR. This condition is observed over the entire ocean domains. For the extreme cases shown in Figure 20, the differences PR-TMI ice-scattering signatures become lower. Weaker ice-scattering signals from TMI extreme events are observed only over East Pacific Ocean, but almost equal to PR extreme events for the other ocean regions.

The diurnal time peaks over land have a more significant variation than observed over the ocean regions (Figure 21). The climatological plots show that the PR rain peaks occur earlier than identified by the TMI. This result is similar to Yamamoto et al (2008) as described above. Differences between PR and TMI ice-scattering signatures are also observed. In contrast to the ocean differences, the TMI identifies stronger ice-scattering signals than the PR. Plots of the extreme differences (Figure 22) show larger differences for the afternoon peaks. The peak frequencies are much higher for TMI extreme events than PR extreme events. This result suggests that PR-TMI extreme-rain biases over land are possibly related to the precipitation development processes during the land afternoon heating. For the extreme cases, the collocated TMI 85 GHz PCTs show a larger difference than the climatological differences. The TMI tends to identify extreme events with very strong ice-scattering, which occur mostly during the afternoon. The higher TMI afternoon peak frequency for the extreme cases are associated with the linear relationship between rain-rates and ice-scattering, as observed from the Maritime Continent case study. A regional comparison between collocated PR radar profiles and TMI 85 GHz ice-scattering, as similar to the Maritime Continent case study, is examined in the next part.

4.3 Comparison of collocated PR Radar reflectivity profiles

The previous comparison of PR-TMI general and extreme-rain biases shows that there are specific features of the extreme that could not be explained by the general rain. This section aims to identify the source of the rain estimation biases in extreme rainfall by focusing on the PR and TMI retrieval processes. From the case study analysis, the collocated PR vertical rain profiles show that higher near-surface rain-rates could occur

without significant ice particles. To examine more detail about the regional differences, a similar methodology is conducted for each ocean and land region. In the first part, the comparison of the PR collocated radar reflectivity profiles corresponding to PR and TMI extreme events is shown. Differences in TMI collocated brightness temperatures are explained next.

Several researchers have identified that some PR and TMI biases, in general, are related to the differences in the retrieval process. One of the factors is the condition where the PR and TMI identify different phases of convection. The TMI tendency to identify mature to decaying cloud phases is suggested to be associated with taller clouds (Furuzawa and Nakamura 2005; Yamamoto et al. 2008). Another condition that should be considered is related to the warm rain process where collision and coalescence occur intensively (Song and Sohn 2015; Hamada et al. 2015). This condition could lead to a high radar reflectivity near-surface, but remains low at the upper part.

A comparison of the collocated PR radar reflectivity profiles for PR and TMI extreme rain events over the ocean domains are shown in Figure 23. The result shows that PR extremes have higher reflectivity than TMI extremes for almost the entire vertical profile. The near-surface reflectivity is close to 50 dBZ for PR extremes, and 40 dBZ for TMI extremes. The higher reflectivity suggests a strong signal detected by the PR, but somehow missed by the TMI. The higher PR reflectivities are observed from all the ocean domains and consistent with Figure 16 where the PR identifies higher rain-rates than the TMI in extreme ranges.

The comparison of the collocated radar reflectivity profiles over land shows almost similar profiles compared to the ocean (Figure 24). PR and TMI extreme profiles more conform at 5 km and above. Below this level, PR extreme profiles are continuously increasing close to the surface. In contrast to PR extreme profiles, the TMI downward increase is less significant than identified by the PR. The increasing reflectivity near the surface possibly generated by the high rate of collision and coalescence of rain particles below the freezing level, as indicated by Song et al (2017). These factors contribute to the PR downward increase that represents the warm type extremes, which are not identified by the TMI.

4.4 Comparison of collocated TMI brightness temperatures

To clarify why TMI hardly identify warm type extreme over land and does not detect strong PR signals over the ocean, a comparison of the collocated TMI brightness temperatures is conducted, as similar to the Maritime Continent case study. In this section, the observed differences between the PR and TMI when identifying heavy precipitation events are demonstrated. First, the joint distribution plots of the collocated TMI 85 GHz minimum polarization corrected brightness temperatures and rain-rates are presented. Plots of the probability distribution functions (PDFs) of the collocated TMI brightness temperatures corresponding to the PR and TMI uppermost 10% rain rates are also compared in this part. Over the ocean domains, the PDF plots for the 10, 19, 21, 37, and 85 GHz brightness temperature bands are presented. Over the land domains, only the 85 GHz brightness temperature data are shown.

The plots of the collocated TMI 85 GHz minimum PCTs versus rain-rates over each ocean domain are shown in Figure 25. This figure indicates that both PR and TMI show a board relationship between the near-surface rain and the collocated 85 GHz PCTs. This result is similar to the Maritime Continent case study in the previous section. In addition, the figure also shows that for TMI, the upper-end distribution of extreme events is found at higher PCTs compared to the PR. White lines in the figure pinpoint the PCT where the maximum number of events are observed for rain rates above the uppermost 10%. The TMI lines correspond to slightly higher PCTs at some regions compared to the PR.

The plots of the collocated TMI 85 GHz minimum PCTs versus the rain rates over the land domains are shown in Figure 26. This figure shows the clear contrast between PR and TMI for all of the land domains. The PR joint distribution plots show similar relationships for the ocean domains. In contrast to the PR, the TMI shows a strong relationship between the two parameters, as similar to the Maritime Continent case study. In a more specific, the TMI tends to detect higher numbers of events at lower PCTs, approximately about 160-180 K at above the uppermost 10% rain events (white lines in Figure 26).

The PDF plots of the collocated TMI 85 GHz brightness temperatures for the PR and TMI extreme events over the ocean domains are shown in Figure 27. This figure shows that the TMI exhibits a gradual change from the Maritime Continent to the Eastern Pacific Ocean. The PR extreme events tend to have lower 10 GHz brightness temperatures than the TMI extremes over the Maritime Continent. The PDFs corresponding to the PR and TMI extreme events are more conform over the East Pacific Ocean. The TMI extreme events produce slightly lower brightness temperatures at 85 GHz than the PR extreme events over the Maritime Continent. This contrast with East Pacific Ocean, where the TMI extreme events have higher brightness temperatures at 85 GHz than the PR extremes.

The plots of the collocated TMI 85 GHz brightness temperature PDFs for the PR and TMI extreme events over the land domains are shown in Figure 28. All the regions show that the TMI extreme events are characterized by lower brightness temperatures than the PR extreme events at the rightmost edge of the distribution, while the PR PDF is skewed slightly warmer than the TMI PDF. The warmer PR PDF suggests that PR not only capture precipitation with a large number of ice particles near the cloud top as similar to TMI, but also the warm extremes.

4.5 Discussion and Summary

This section gives an introduction about the PR-TMI extreme-rain biases and explains how it could be different compared to the general rain biases. Previous analysis conducted by Yamamoto et al (2008) highlights the differences between the PR and TMI for general rains, which are related to the physical backgrounds in convective development. The comparison of PR-TMI extreme-rain biases reveals that it becomes more significant since the TMI detects a large number of afternoon peak compared to the PR over land. The PR extreme events over land also could be described to have relatively low storm top heights (Liu and Zipser 2014) and weak ice-scattering signals (Furuzawa and Nakamura 2005; Zagrodnik and Jiang 2013). All of the above results indicate that the PR and TMI capture different heavy precipitation systems as a response to the differences in the active-passive sensors.

To demonstrate the differences between the TRMM active-passive sensors in identifying heavy rainfall, comparison of collocated PR radar reflectivity profiles and

collocated TMI brightness temperature have been conducted. A downward increase of reflectivity has been identified for PR extreme events over land. The PR downward increase is also identified by Song and Sohn (2015) and Hamada (2015). Comparison of the collocated TMI extreme profiles, however, cannot detect heavy rainfall with the large downward increase as similar to the PR, as suggested from the Maritime Continent case study. The TMI land algorithm assumes higher rain-rates with higher ice scattering. However, PR extreme events show that heavy rainfall could occur with weaker ice-scattering signals.

The PR-TMI extreme rain differences over the ocean are characterized by higher radar reflectivity for the entire vertical profiles for the PR extremes, and lower for the TMI extremes. Although the utilization of TMI emission bands indicates better agreement in the ice-scattering and rain-rate relationship compared to the PR, there is a regional variation of the collocated TMI T_{BS} over the ocean. In general, there is a westward decrease of collocated TMI 85 GHz T_{BS} over the Pacific Ocean that is not identified by the PR. Liu and Zipser (2014) suggested that the wide but shallow precipitation systems over the East Pacific possibly gives an influence to the TMI emission bands. The emission signals from TMI extreme events over the East Pacific conform the emission signals from PR extreme events. However, the ice-scattering signals identified by the TMI are weaker than the PR. Over the Western Pacific Ocean, TMI extremes have stronger emission signals and ice-scattering signals as well. In contrary, the heavy precipitation structures identified by the TMI in those areas have weaker reflectivity than identified by the PR.

The reason why TMI detects stronger emission and ice-scattering signals, but lower radar reflectivity over the West Pacific and the Maritime Continent is not yet known. The reason might be underlying in the different tendency of the PR and TMI in identifying regional properties of the precipitation structure. For example, over the West Pacific and the Maritime Continent Ocean, CloudSat often identify deep convective clouds with weaker reflectivity at the cloud top compared to the global mean (Sohn et al. 2015). To this end, the different factors influencing the extreme rain-rate retrieval are well explained using collocated PR radar reflectivities and TMI brightness temperature data. The combination with other satellite sensors and datasets, particularly CloudSat and ERA-Interim, is presented in the next section.

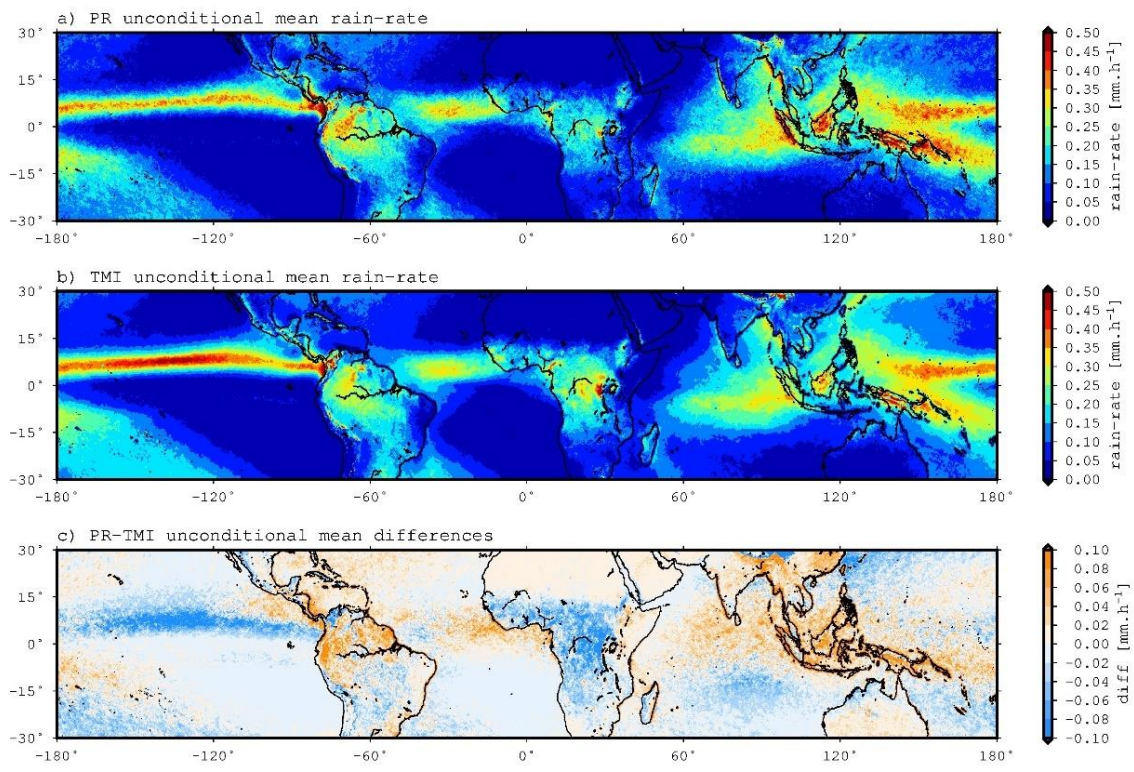


Figure 15. Global map of unconditional mean rain-rates from a) TRMM PR, b) TRMM TMI, and c) PR-TMI unconditional mean differences.

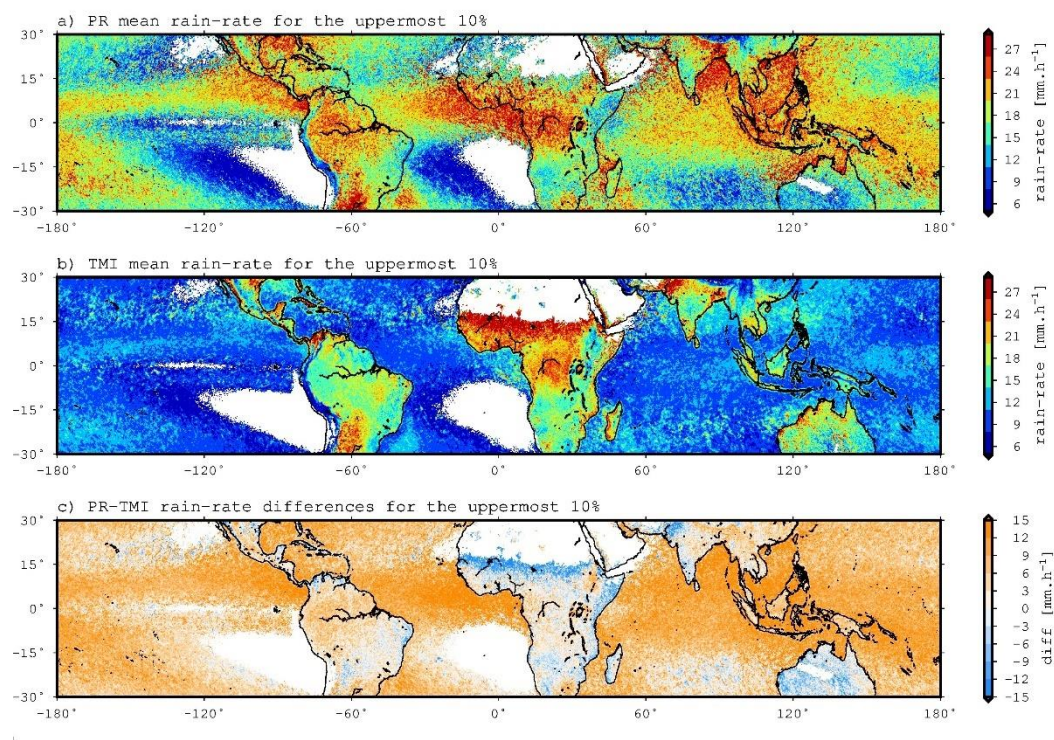


Figure 16. Similar to Figure 15, but only for the uppermost 10% of the rain-rate distribution.

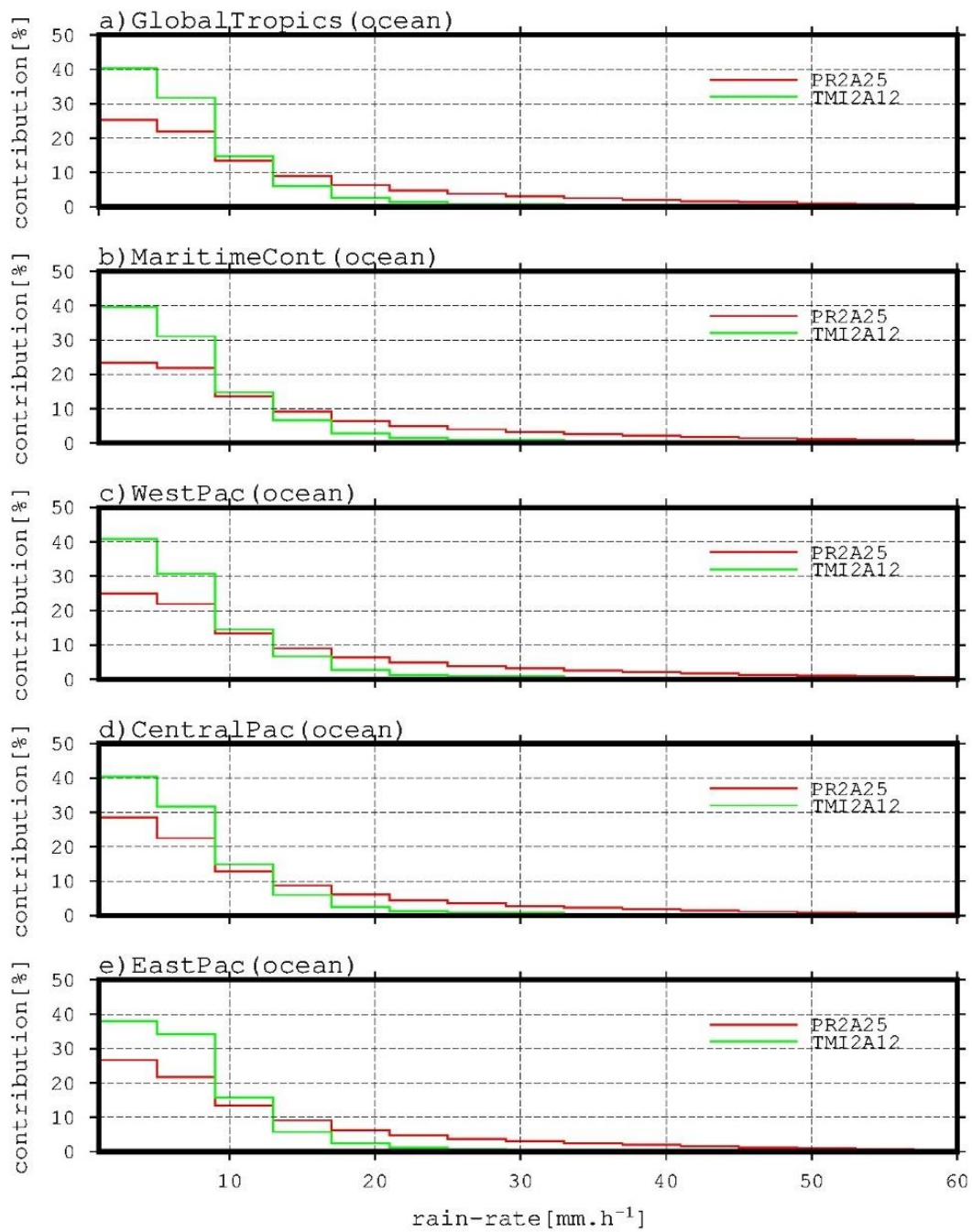


Figure 17. Rain-rate contribution to the total rainfall from PR (red) and TMI (green) for the ocean domains: a) Global tropics, b) Maritime Continent, c) West Pacific, d) Central Pacific, and e) East Pacific.

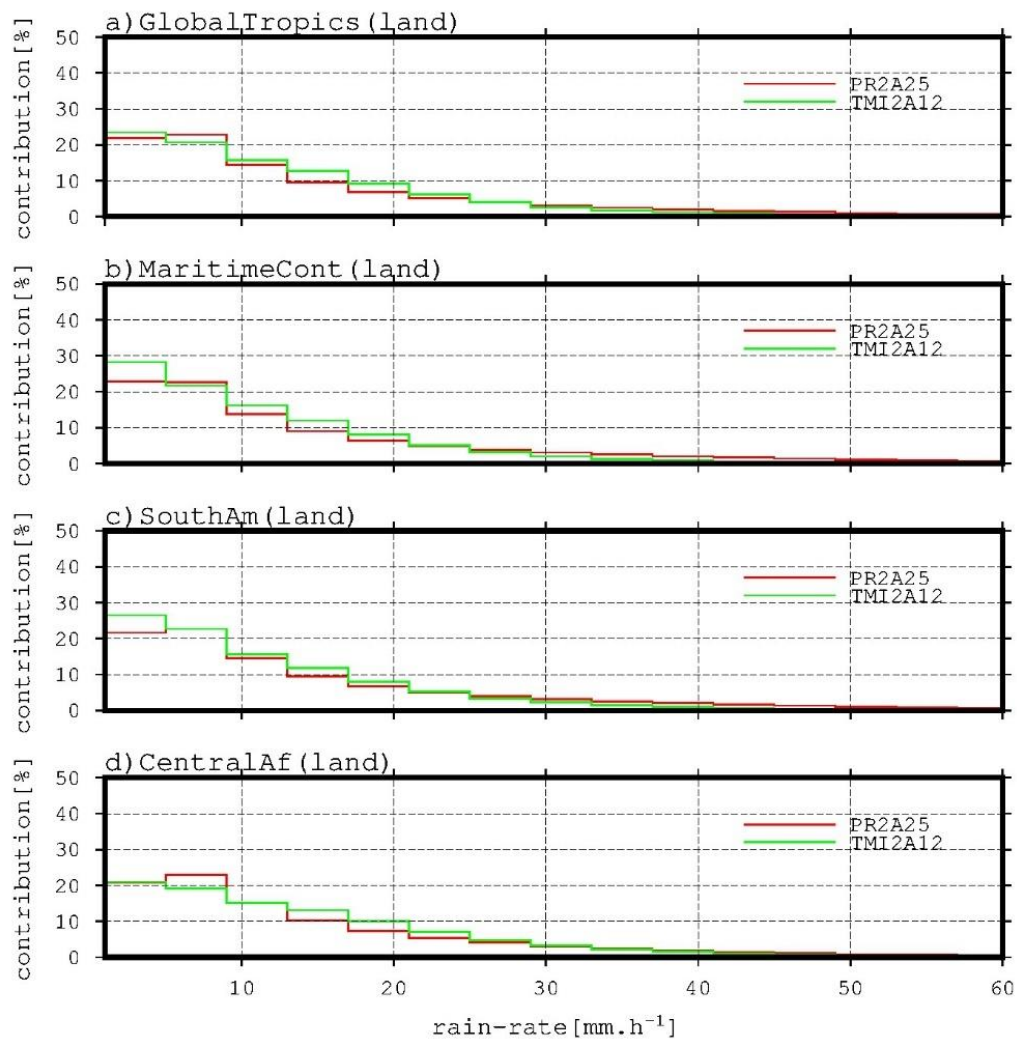


Figure 18. Rain-rate contribution to the total rainfall from PR (red) and TMI (green) for the land domains: a) Global tropics, b) Maritime Continent, c) South America, d) Central Africa.

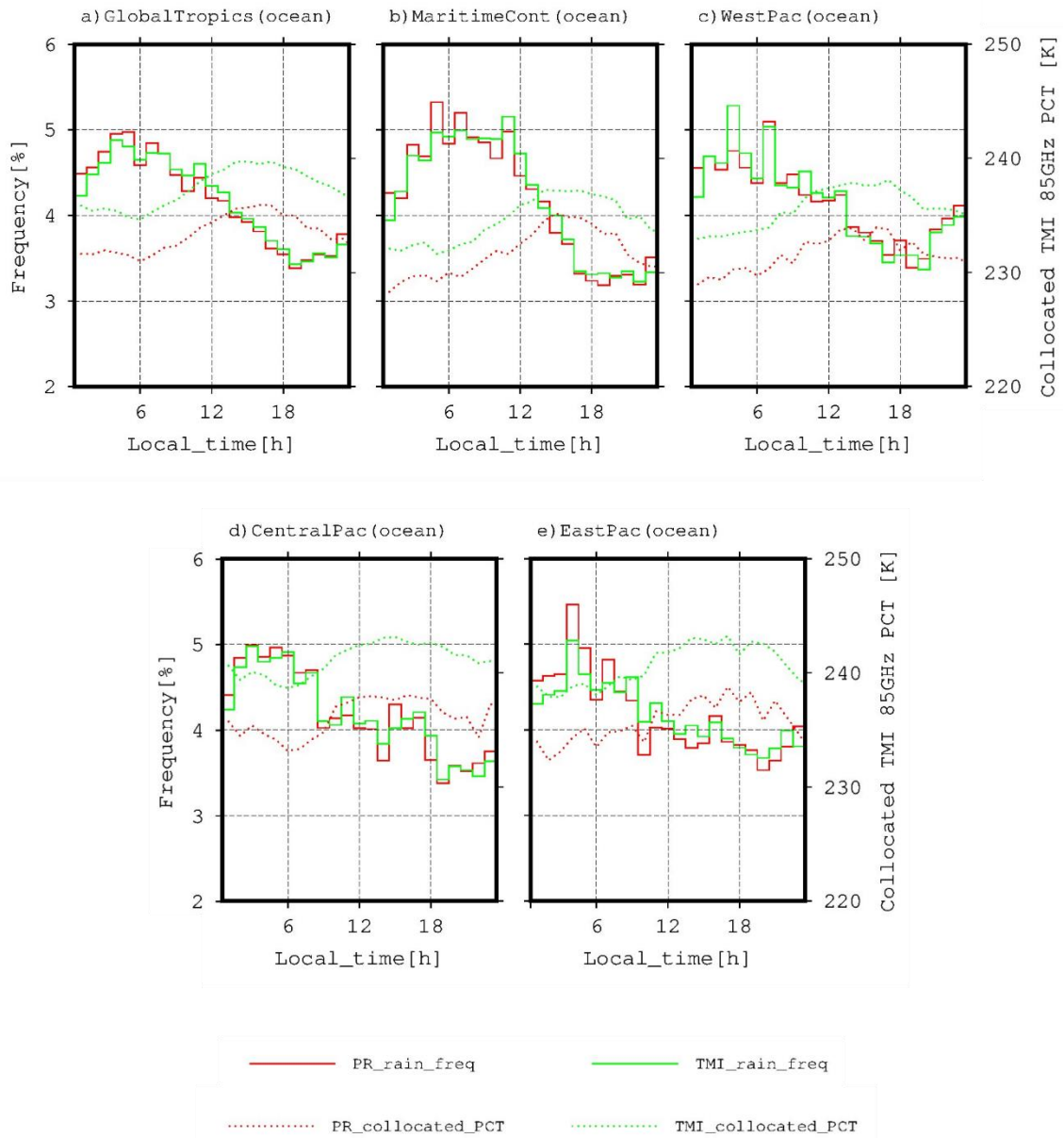


Figure 19. Fraction to total rain events in the local time basis for rain rate above 1 mm h^{-1} over the ocean domains: a) Global Tropics, b) Maritime Continent, c) West Pacific, d) Central Pacific, and e) East Pacific.

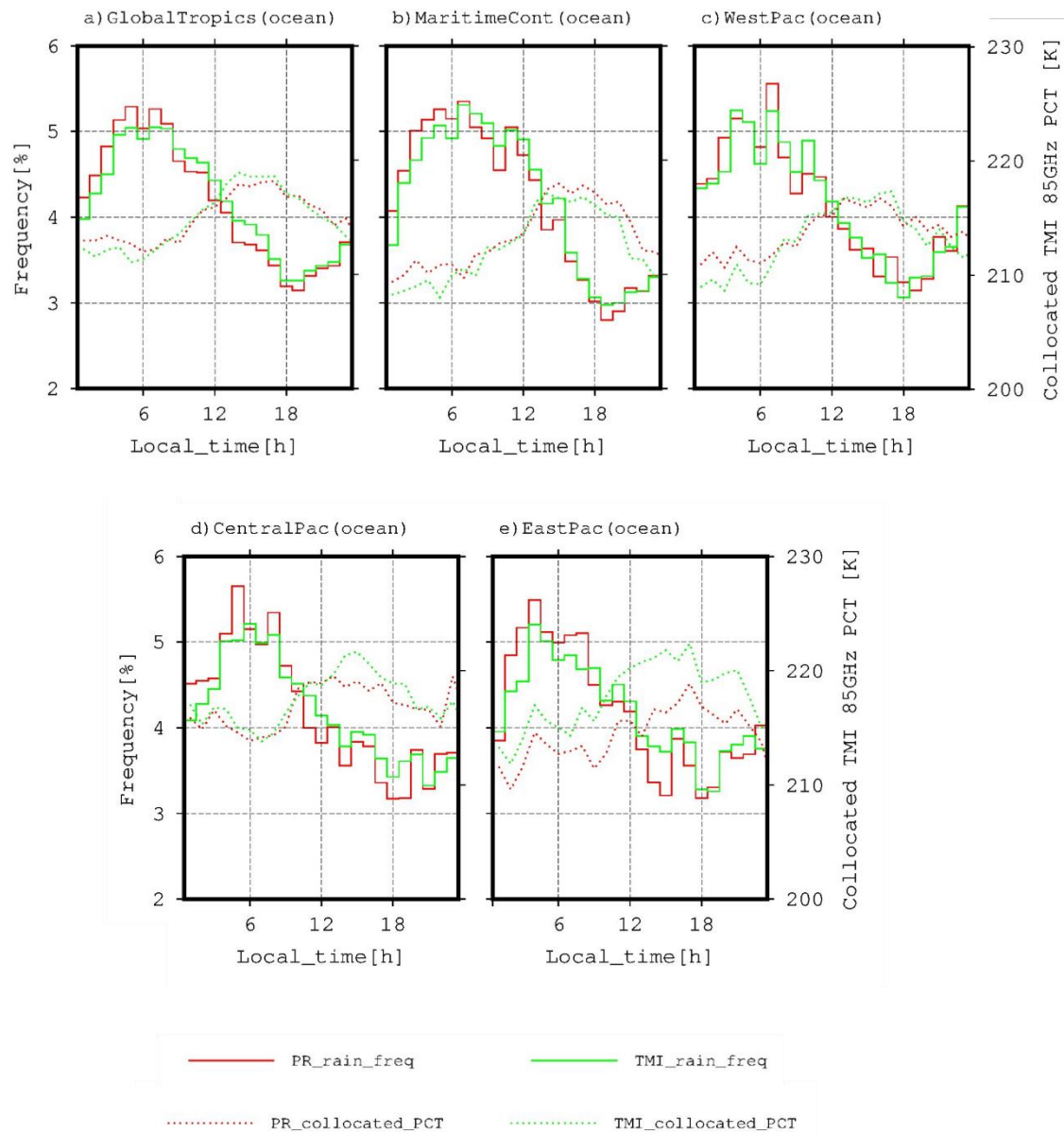


Figure 20. Similar to Figure 19, but for the uppermost 10% rain-rates only.

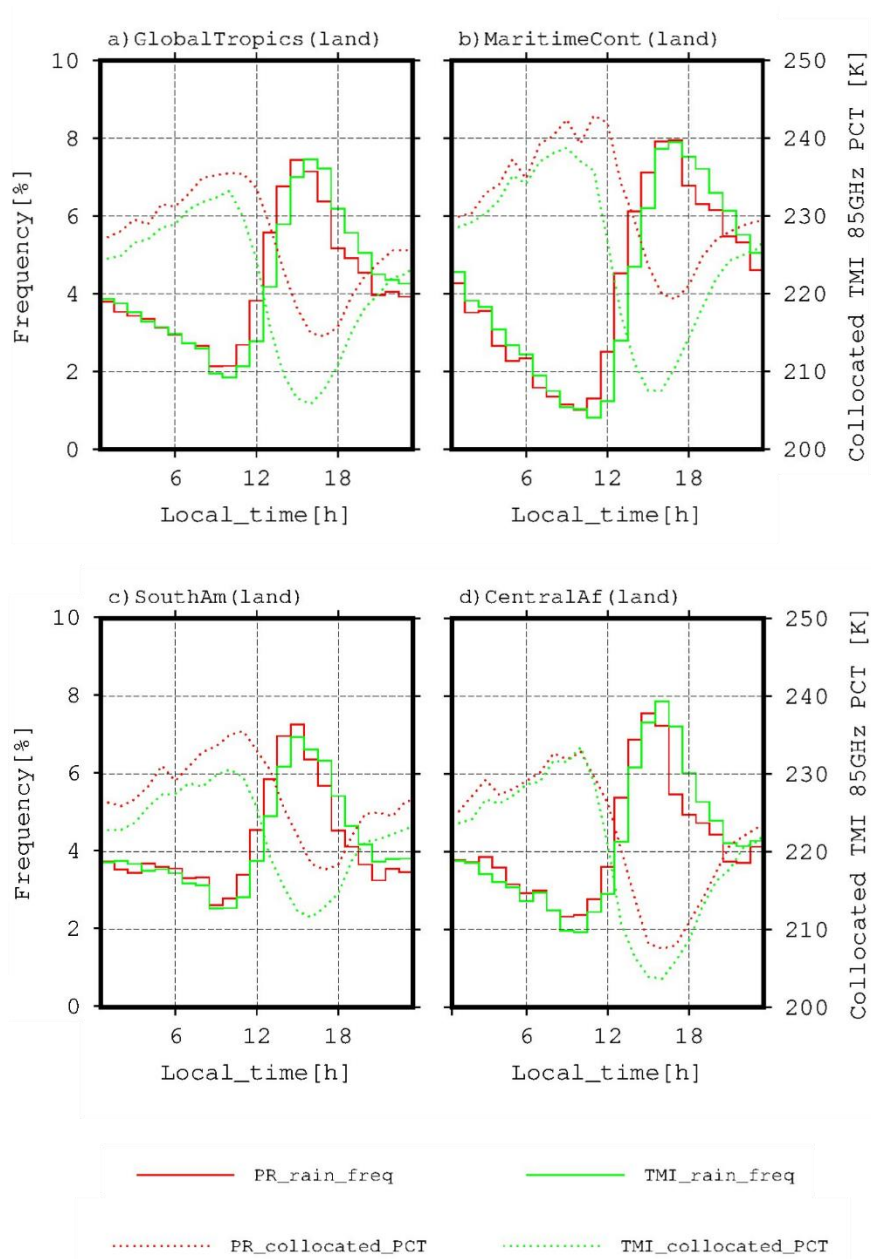


Figure 21. Fraction to total rain events in the local time basis for rain rate above 1 mm h^{-1} over the land domains: a) Global Tropics, b) Maritime Continent, c) South America, and d) Central Africa.

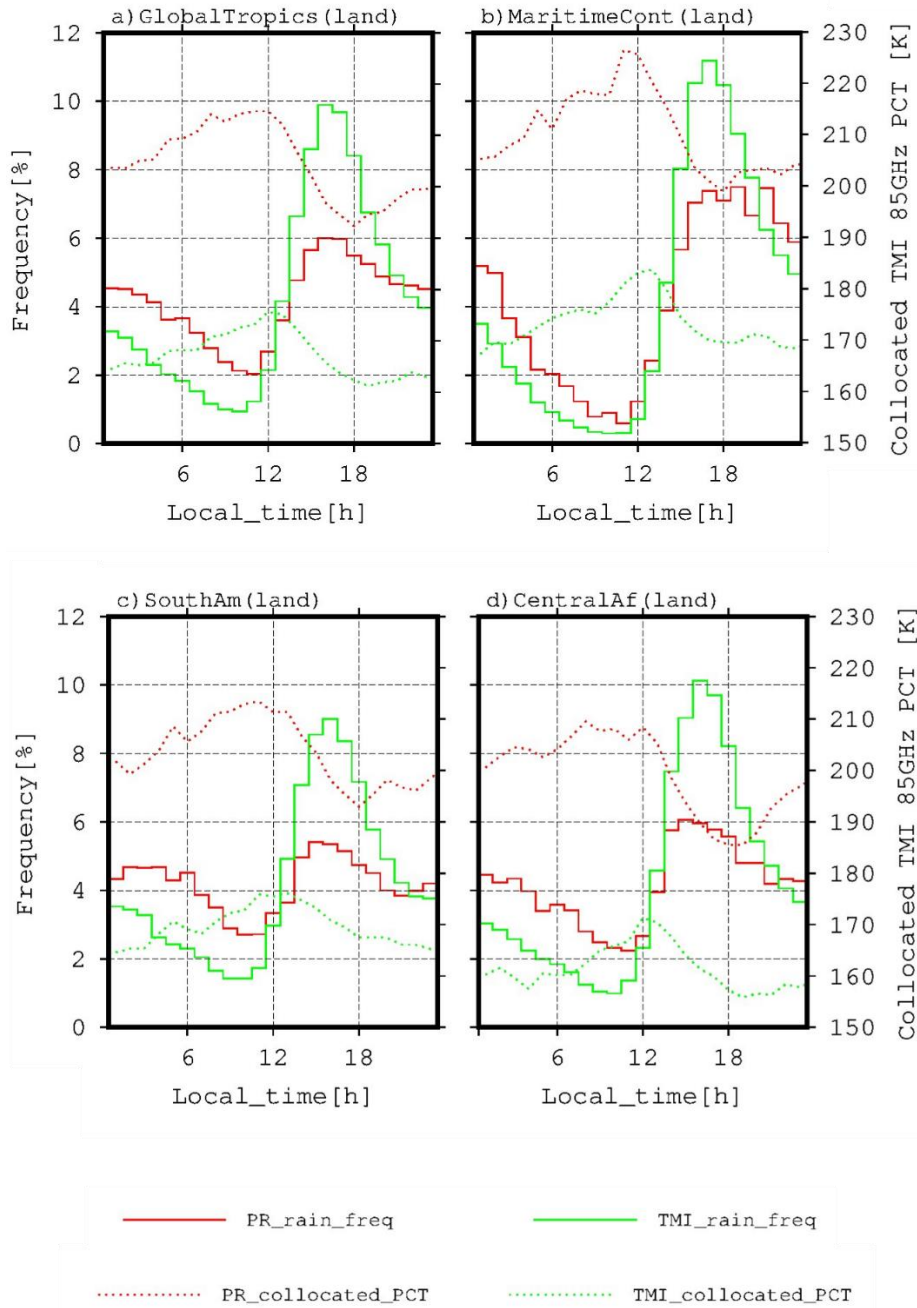


Figure 22. Similar to Figure 21, but for the uppermost 10% rain-rates only.

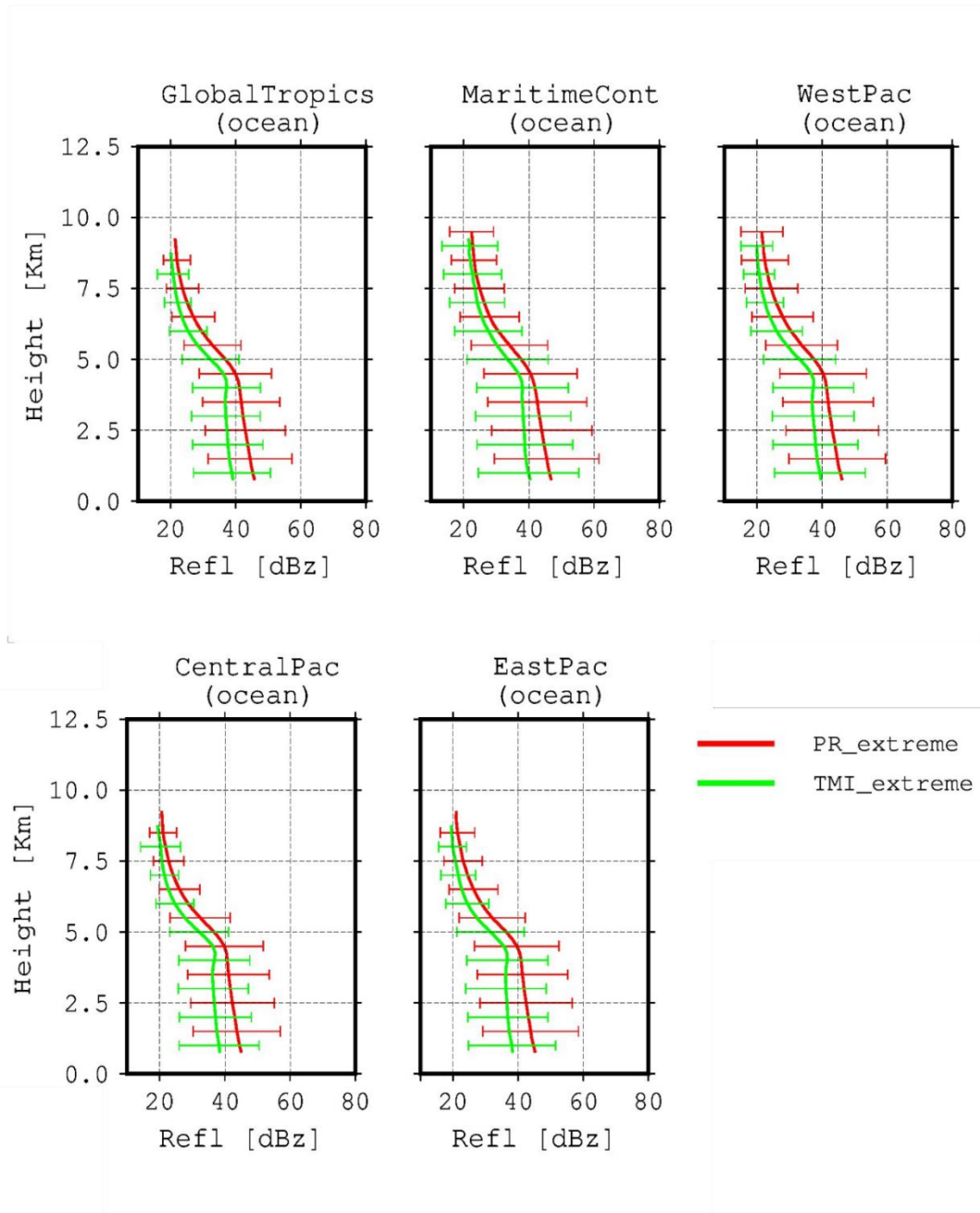


Figure 23. Collocated TRMM PR reflectivity profile for PR rain-rates (top) and TMI rain-rates (bottom) for the uppermost 10% distribution. Top (from left to right): Global Tropical Ocean, Maritime Continent, and West Pacific. Bottom (from left to right): Central Pacific and East Pacific.

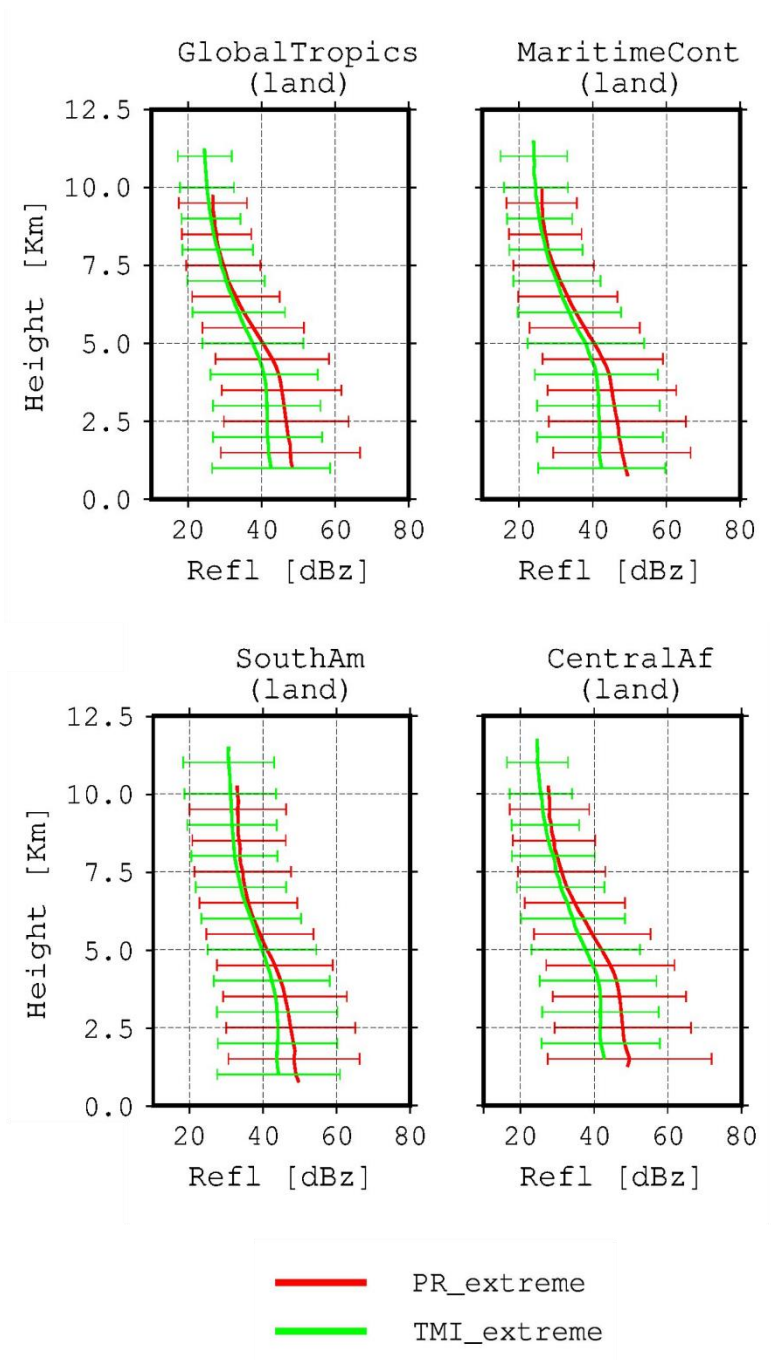


Figure 24. Similar to Figure 23, but for the land domains. Top: Global Tropical Land (left) and Maritime Continent (right). Bottom: South America (left) and Central Africa (right).

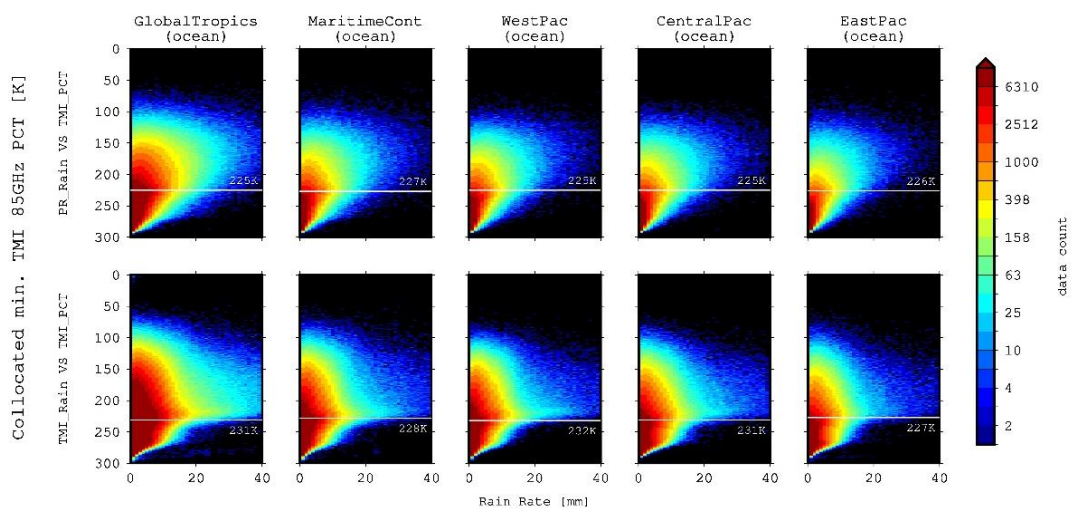


Figure 25. Joint distribution of collocated minima TMI 85 GHz PCTs vs PR rain rates (top) and TMI rain rates (bottom) for ocean regions. From left to right: Global Tropics, Maritime Continent, West Pacific, Central Pacific, and East Pacific. The color bar indicates the number of data points. The white lines indicate the brightness temperature where the rain frequency above the uppermost 10% reached a maximum.

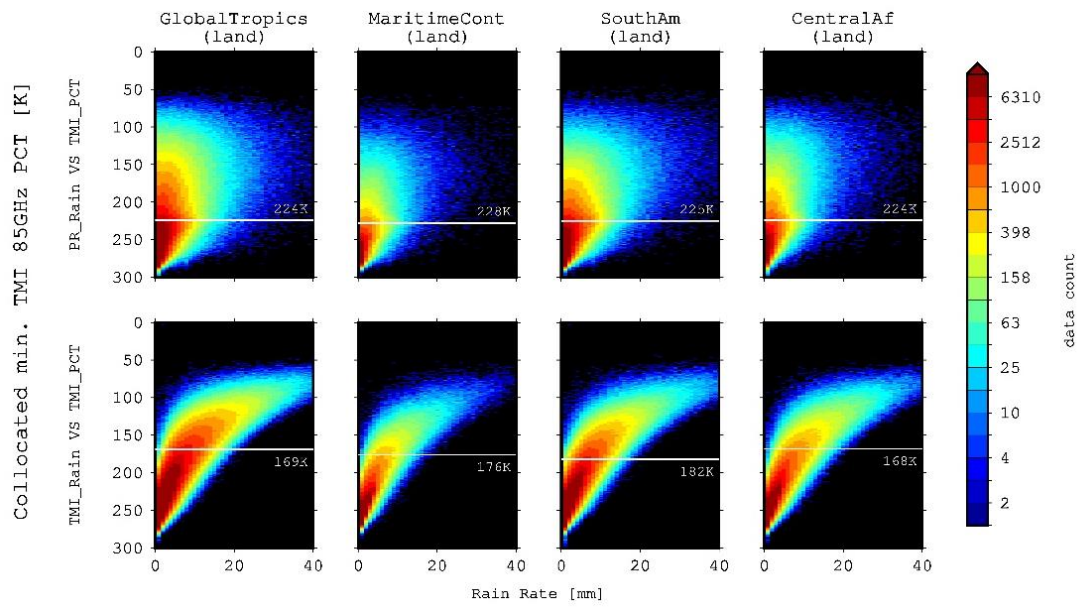


Figure 26. Similar to Figure 25, but for the land domains. From left to right: Global Tropical Land, Maritime Continent, South America, and Central Africa.

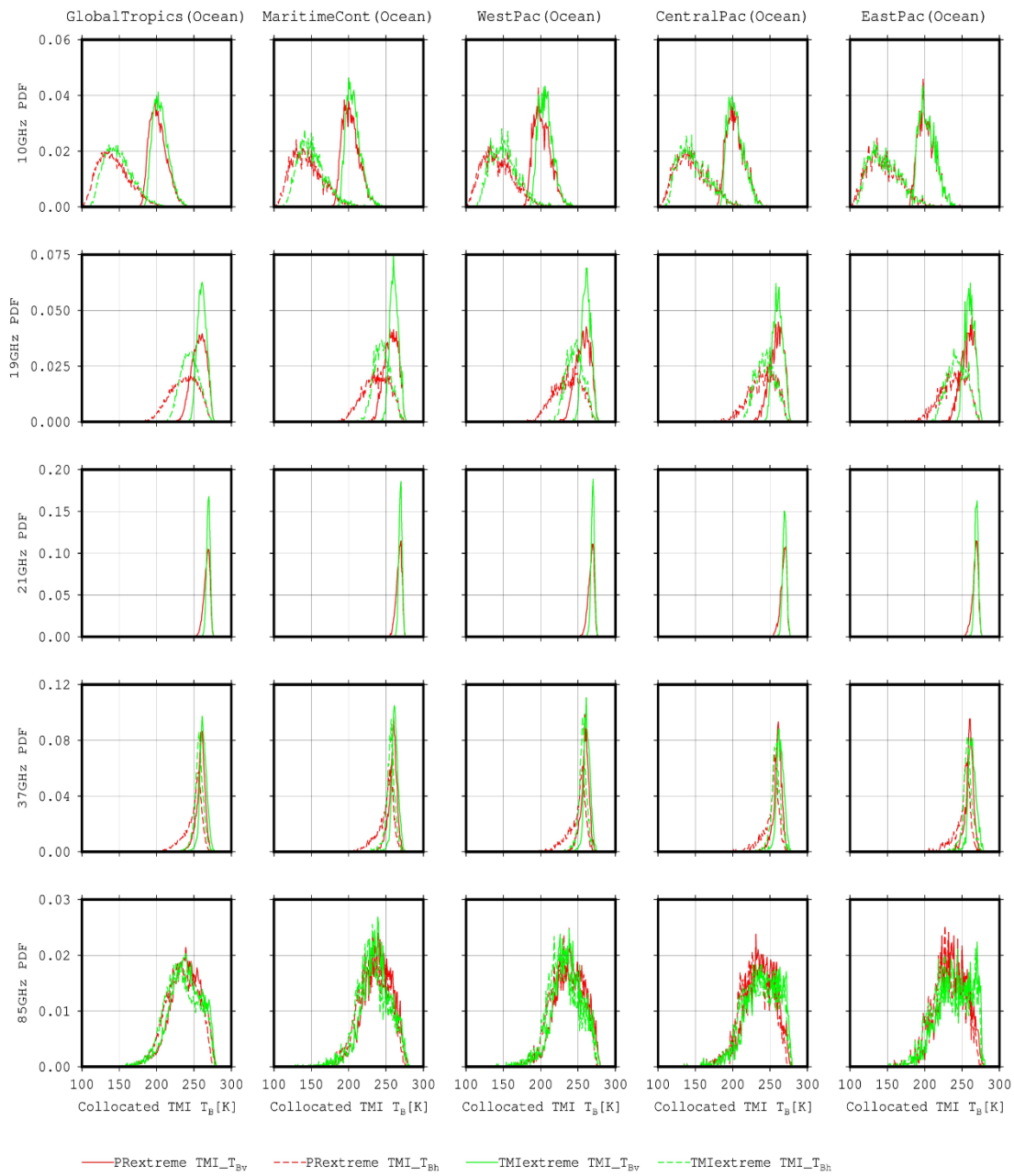


Figure 27. Collocated TMI brightness temperatures for the PR and TMI extreme events over the oceans for each region (left-right) and the brightness temperature channels (top-bottom).

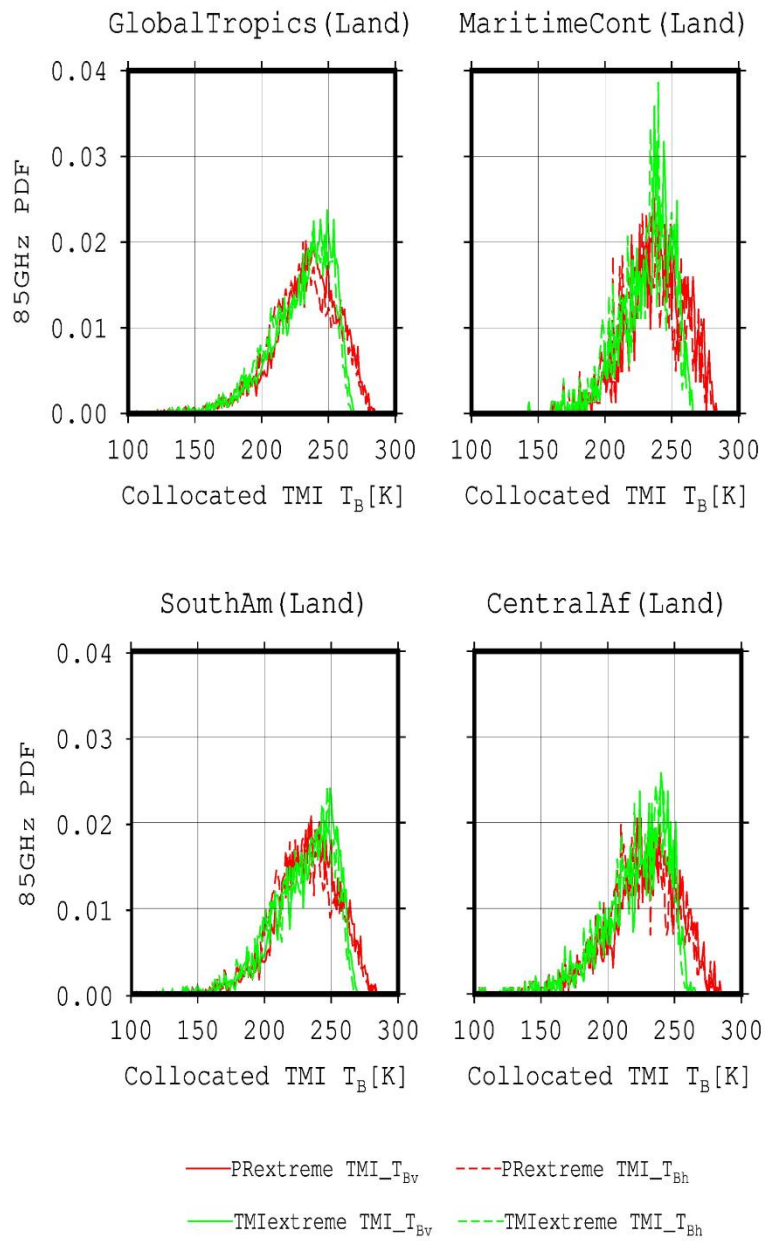


Figure 28. Similar to Figure 27, but for the land domains.

5. Explaining the origin of TRMM PR-TMI extreme-rain biases using CloudSat and Reanalysis data

5.1 TRMM PR-TMI heavy rainfall biases in the view of CloudSat composite cloud structure and convective fractions

The comparative analysis of the PR-TMI extreme-rain biases presented in the previous section suggests that the active and passive TRMM sensors are systematically different in their methods in identifying heavy precipitation events. The previous result also suggests that an analysis of the detailed cloud structures would be beneficial for explaining the PR-TMI extreme precipitation biases. A combination of different satellite observations, such as CloudSat, has been known to give a more detailed view of the precipitating clouds (Masunaga 2012; Sohn et al. 2015).

In this section, the differences between the PR-TMI extreme events are assessed by utilizing CloudSat and ERA-Interim observations. Although the utilization of CloudSat 94 GHz radar is beneficial to identify cloud structures (Sohn et al. 2015), stronger attenuation by large hydrometeor particles, which is typical for extreme events, could produce large errors. Therefore, this analysis is limited to the horizontal cloud structures. In the first part, a comparison of the collocated CloudSat composite cloud fractions (Igel et al. 2014) is presented. The collocated CloudSat convective/stratiform cloud fractions from CloudSat are examined next.

As the first result, the collocated CloudSat cloud fractions associated with the PR and TMI extremes over the ocean domains are shown in Figure 29. TMI displays regional variations from the Maritime Continent to the eastern Pacific Ocean. Over the Maritime Continent, the TMI extreme events correspond to taller and horizontally extensive clouds. However, the heights continuously decrease toward the eastern Pacific Ocean. Over the eastern Pacific Ocean, the TMI tends to identify shallow but organized clouds. Liu and Zipser (2013) showed that shallow-organized clouds are predominant in this area. TMI somehow detects these clouds as extremes rather than detecting the taller clouds identified

by PR. Moreover, the differences among the ocean regions identified by PR do not display this gradual change. Shige et al (2008) showed that PR captures the contrast between the western and eastern Pacific Oceans that mainly occur during La Nina. In the present results, the PR rainfall over the eastern Pacific Ocean produces a similar profile to that of the western Pacific Ocean, possibly because this work exclusively targeted extreme events.

The corresponding PR and TMI extreme precipitation cloud fractions over the land domains are shown in Figure 30. The CloudSat cloud fractions over the land domains differ from those over the ocean domains. All land domains show that the TMI extreme events are confined to narrow convective cells. In contrast, the PR extreme events are generated by more horizontally extensive cells with lower cloud top heights than those of TMI. However, the PR extremes with relatively low STHs could generate greater rain rates than the TMI extremes with taller STHs.

It has been identified in the previous section that there is a contrast between the Western Pacific Ocean and the Eastern Pacific Ocean in term of TMI brightness temperatures. To characterize the difference in more detail, a contrast between cloud temporal evolution between over the Maritime Continent Ocean and the East Pacific Ocean is shown in Figure 31. The TMI extreme cloud structure over the Maritime Continent Ocean is initially larger than the PR extreme cloud structure. The TMI clouds are getting wider and taller over time, which corresponds to stronger brightness temperature signals captured by TMI. Over the East Pacific Ocean, TMI initially identifies shallow but horizontally extensive clouds. The TMI cloud top heights remain low over time compared to the PR clouds, which corresponds to weaker ice-scattering signals captured by TMI.

To further characterize the above difference, the CloudSat convective/stratiform fractions over the ocean domains are shown in Figure 32. A different feature is observed between the Maritime Continent and the eastern Pacific Ocean. Over the Maritime Continent, an earlier convective peak is identified by TMI, occurring approximately 3 hours before the extremes detected by the TRMM, while the PR convective peak occurs 1.5 hours before. Liu and Zipser (2014) showed that TMI tends to detect greater precipitation areas than PR. The greater precipitation areas could be generated by more horizontally extensive cells with earlier convective peaks than those detected by PR. Over

the observed land domains, TMI often identifies larger convective fractions than PR (Figure 33). However, the time peak difference is only observed over the Maritime Continent.

From the above results, we can initially characterize the PR-TMI differences as a function of convective organizations. Since many variables could be utilized to characterize this organization (Rickenbach and Rutledge 1998), in this research, the organizations are simply defined with regard to the horizontal scales of the systems. The more organized systems are associated with larger cloud structures and vice versa. Furthermore, a comparison of CloudSat data for different time windows shows that the horizontal cloud extents are continuously increasing after the convective peaks are reached. The degree of organization of the systems can therefore be characterized based on the time differences between the peaks. Over the Maritime Continent, TMI captures more organized systems than PR. This result is reversed over the eastern Pacific Ocean, where TMI captures less organized systems than PR.

5.2 TRMM PR-TMI heavy rainfall biases in the view of environmental instability from ERA-Interim

To further study the physical processes in the precipitation cloud development, comparisons of the environmental profiles from the ERA-Interim are given in this part. A similar comparison to Hamada et al (2015) to characterize the warm rain extreme is conducted in this analysis. To begin with, the potential temperature and humidity profile differences corresponding to the PR and TMI extreme events are compared. This comparison is conducted to ensure that the differences caused by the warm rain are present for the PR extremes. Comparison of those variables is also useful in characterizing the PR-TMI gradual changes over the Pacific Ocean. At the end of this part, the influence of the instabilities in the PR and TMI heavy precipitation cloud development are explained.

First, the corresponding PR-TMI environmental profile differences over the ocean domains are shown in Figure 34. The results show that the TMI extreme events occurred in more humid environments than those of PR. A transition is also observed from the

Maritime Continent to the eastern Pacific Ocean. The height at which the humidity difference is largest decreases from the west to the east. Over the Maritime Continent, the TMI extreme events correspond to higher humidities throughout the troposphere. Over the eastern Pacific Ocean, the humidity excesses of the TMI extremes are reversed and become humidity deficits above 500 hPa and near the surface.

The PR extreme events over the ocean domains generally have slightly warmer potential temperatures near the surface, but have colder values above the 500 hPa level than those of the TMI extreme events. The Maritime Continent-eastern Pacific Ocean transition is also present in the potential temperature profiles. As identified by PR, the Maritime Continent is characterized by lower potential temperatures in the mid-troposphere and shows only slight differences from the TMI values near the surface. Over the eastern Pacific Ocean, the near-surface temperature differences become larger.

The corresponding PR-TMI environmental profile differences over the land domains are shown in Figure 35. This figure shows that the PR extreme events occur at higher specific humidities than the TMI extreme events for all identified regions, except near the surface, differing from the results for the ocean extremes. Higher specific humidities were observed, especially at the 850-500 hPa level. Furthermore, the corresponding PR extreme events show colder potential temperatures near the surface than those of the TMI extreme events. The greater humidity but lower potential temperature differences corresponding to the PR extreme events were also identified by Hamada et al (Hamada et al. 2015). However, the ocean has considerably different thermodynamic characteristics than those of the land domains, and clouds cannot be explained by the above results.

The CAPE plots corresponding to the PR and TMI extreme events over the ocean domains are shown in Figure 36. In general, the highest rain rates are detected with downward slopes after the CAPE drops following a maximum that resembles tropical deep convective clouds (Masunaga 2012). The PR extreme events over the ocean domains have higher CAPE values than the TMI extreme events. The ocean CAPEs also increase from the eastern Pacific to the western Pacific, reaching a maximum over the Maritime Continent. TMI extremes prefer slightly more stable environments than the PR extremes as implied by the potential temperature profiles shown earlier. Over the land domains, the corresponding TMI CAPEs are greater than the PR CAPEs with notable

diurnal variations (Figure 37). This result indicates that the TMI extreme events occur in more unstable environments than the PR extreme events, differing from the ocean composite.

5.3. TRMM PR-TMI heavy rainfall biases and its association with precipitation organizations

This study investigates the precipitation biases from the TRMM active-passive sensors due to different cloud structures and environmental properties. The combination of the TRMM, CloudSat, and ERA-Interim data provides comprehensive information to explain the PR-TMI estimation differences. The general properties of the PR-TMI differences in identifying the heavy rainfall events are further discussed in this section.

Noticeable differences between the PR and TMI extreme events are observed over the ocean and land domains. The TMI extremes are not essentially different from the PR extremes over ocean domains regarding their PCTs (Figure 25). However, the collocated TMI microwave emissions indicate regional differences of TMI over the ocean domains (Figure 27) that also differ from the PR extreme events. Over the eastern Pacific Ocean, the cloud top heights corresponding to the TMI extreme events are lower than those of the PR extreme events (Figure 29), which may represent shallow but organized clouds because their horizontal extent is much larger than those of individual cumulus clouds (Figure 38: bottom right) (Liu and Zipser 2013). The shallow horizontally extensive clouds are associated with moister environments near the surface, but dryer environments than those of their the PR counterparts at approximately the 500 hPa level (Figure 34). The shallow horizontally extensive clouds were also found in a more stable environment than that identified by PR (Figure 36). In contrast to the shallow horizontally extensive clouds, the higher cloud top heights associated with the PR heavy rainfall events correspond to more unstable environments.

Comparisons among the ocean domains show a regional transition of the extreme precipitation cloud structures from the eastern to western parts of the Pacific Ocean. Over the western Pacific Ocean, the CloudSat profiles show that the horizontal extents are slightly broader for the TMI extremes than for the PR heavy rainfall events (Figure 29).

The TMI convective fraction is greater, and its peak occurs earlier than the PR convective peak, which implies that TMI detects heavily organized precipitation systems (Figure 38: upper right). Based on the corresponding environmental conditions, the TMI extreme events tend to occur in more humid and stable environments than the PR extreme events (Figure 36). In the case of TMI extreme events, the moister environment (Figure 34) could produce more extensive convective cloud systems. The moister environment could be partially due to rain evaporation in stratiform clouds, which moistens the atmosphere.

Over the land domains, the clear ice-scattering signatures (Figure 26) and horizontally confined cloud structures (Figure 30) of the TMI extremes indicate that the TMI heavy rain events are associated with isolated deep convective clouds over land (Figure 39: right). Plots from the ERA-Interim data show that the TMI extreme events over land occur in drier free troposphere conditions but more unstable environment than the PR extreme events. The CAPE patterns (Figure 37) also indicate that the diurnal forcing strongly controls the heavy rain events, primarily via afternoon surface heating (Yamamoto et al. 2008). The more unstable environment produces higher cloud tops and can produce more abundant ice particles aloft (Song et al. 2017), which can then produce a stronger ice-scattering signal.

In contrast, the PR extremes over land tend to be associated with more organized systems (Figure 39: left). The absence of a strong relationship between the PR rain rates and the TMI 85 GHz PCTs (Figure 26) implies that the PR extremes are not always associated with a substantial amount of ice-phase hydrometeors aloft (Furuzawa and Nakamura 2005). The extreme precipitation clouds corresponding to the PR extreme events show more horizontally extensive convective cells than those associated with the TMI heavy rainfall events (Figure 30). The PR heavy rainfall events are associated with moister free troposphere conditions as well as more stable environments than the TMI heavy rainfall events (Figure 37). This more stable environment produces lower cloud top heights and less confined cloud structures, which include warm rain extremes (Song et al. 2017). These warm rain extremes may be missed by TMI due to the lack of ice particles.

5.4. Discussion and Summary

This section highlights the different properties between PR and TMI extreme rain events by using CloudSat and ERA-Interim data. Overall, the differences in the rain-rate retrieval shown in the previous section could be explained using the above datasets. Through a combination of the above datasets, we could learn that the PR-TMI extreme-rain biases are generated by the differences in the vertical and horizontal precipitation structures.

In this research, the PR-TMI rain estimation biases in extreme rain events are further stressed in term of convective organizations. The result shows that there is a contrast between the precipitation organization identified by the PR and TMI over the tropical ocean and land. Over the tropical ocean, the PR tends to identify less organized precipitation than the TMI. Over the tropical land, the PR tends to identify more organized precipitation than the TMI. The above contrast exists due to differences in TMI algorithms over the ocean and land.

The TMI ocean algorithm use both emission and ice-scattering bands. The emission bands have a coarse resolution which is less sensitive to inhomogeneous rainfall (Kummerow 1998). In this research, clear regional differences are observed in the 10 GHz band, where the resolution is more than 60 km x 60 km. It is possible that PR heavy rain events are considered inhomogeneous due to more confined structures compared to TMI heavy rain events. The inhomogeneous rains identified by the PR seems to give an influence to the lower collocated 10 GHz T_{BS} compared to TMI extreme events.

In contrast to the ocean algorithm, the TMI land algorithm utilizes 85 GHz ice scattering band which has the finest resolution compared to the other bands. The TMI 85 GHz band resolution is only slightly lower than the PR resolution. However, the collocated 85 GHz channels show a bias between the PR and TMI since the TMI could not identify liquid phase hydrometeors close to the surface. The assumption in the relation of ice-scattering and rain-rates in the TMI land algorithm, as indicated in this research, is less robust. In the case of warm extreme events, heavy rainfall are possible to be generated generated by excessive moisture near the surface (Song et al. 2017).

The differences in precipitation organizations between PR and TMI extreme events in this research also helps to relate the result with the general rain biases. Over the East Pacific Ocean, the general rain comparison shows that the TMI identifies higher rain-rates than the PR. This is related to the TMI tendency to identify shallow but widely

organized clouds in this area (Liu and Zipser 2014). The taller cloud structures rarely occur in this area, but the PR seems to capture these structures at the uppermost rain-rate distribution. Over the West Pacific and Maritime Continent Ocean, the PR estimates higher rain-rates than TMI for the general rain biases, which are similar to the extreme-rain biases . This condition implies that the TMI fails to estimate less organized precipitations over these areas.

The differences in precipitation organizations are also applied to the general rain biases over the tropical land. Over Central Africa, the TMI estimates higher rain-rates than PR in the general rain biases, but reversed for the extreme rain biases. This could be related to the dominant precipitation structures over Central Africa, which have tall vertical structures and could reach the tropopause (Liu and Zipser 2005). However, heavier precipitation could occur when a large moisture supply is found in the lower troposphere even with a more stable environment. A contrast condition can be observed over the Maritime Continent Land. Over this area, the PR estimates higher rain-rates than the TMI for the general and extreme rain events. The PR tends to detect warm-organized rains which could be related to a humid environment. In more detail, this condition is related to the diurnal circulation that transports a large moisture supply from the ocean to the land (Mori et al. 2004; Ichikawa and Yasunari 2006).

Previous studies have attempted to characterize the PR and TMI biases as a function of precipitation features (Liu and Zipser 2014; Henderson et al. 2017). In advance, Henderson et al (2017) made a PR-TMI adjustment by classifying shallow, deep isolated, and organized precipitations. The differences in precipitation organization are emphasized further in this research. To summarize, heavy rain events mostly occur when the clouds are moderately organized. The organizations not only support the convective cells to repeatedly occur over an area for a long time (Schumacher and Johnson 2005). More importantly, the rain produced in organized systems could evaporate back and produce excessive moisture that is important in warm extreme development (Song et al. 2017). Classifying the degree of precipitation organization, therefore, could be useful in adjusting the sensors to reduce rain-rate estimation biases.

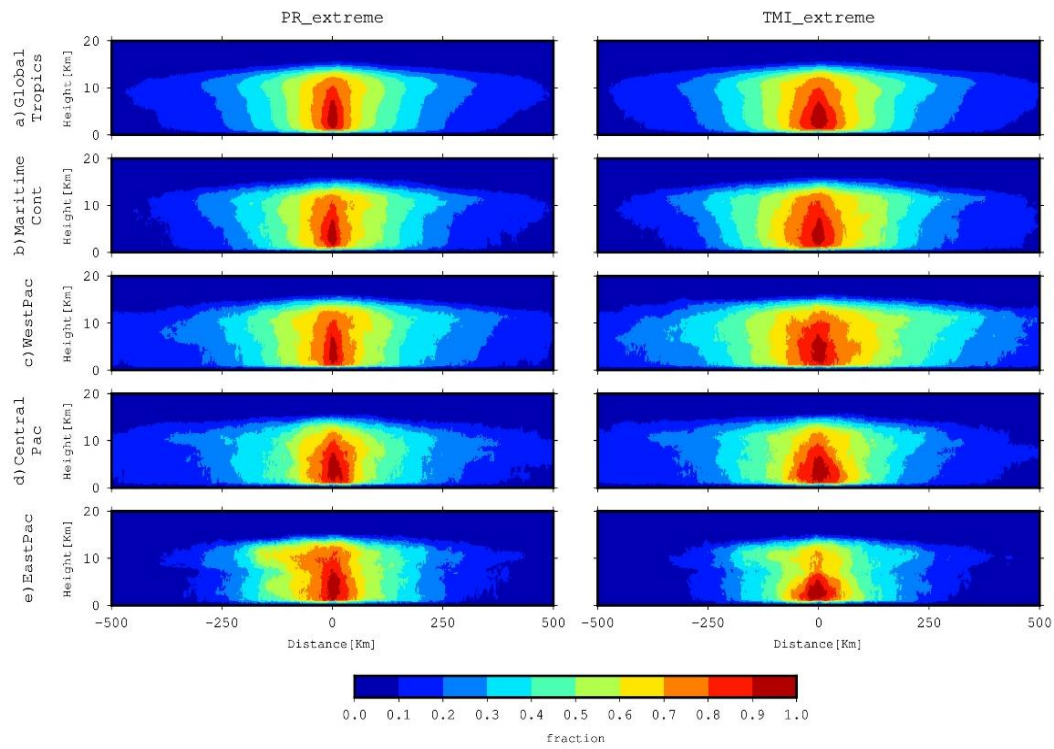


Figure 29. CloudSat collocated cloud fractions for the PR extreme events (left) and TMI extreme events (right) over the examined ocean domains. From top to bottom: Global Tropical Ocean, Maritime Continent, West Pacific, Central Pacific, and East Pacific.

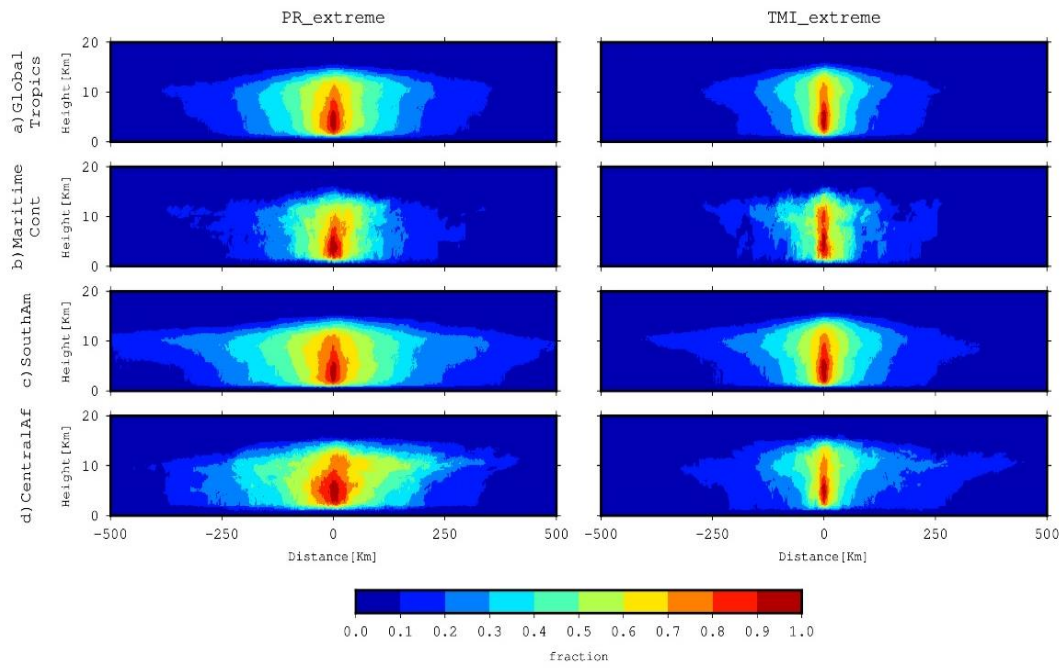


Figure 30. Similar to Figure 29, but for the land domains. From top to bottom: Global Tropical Land, Maritime Continent, South America, and Central Africa

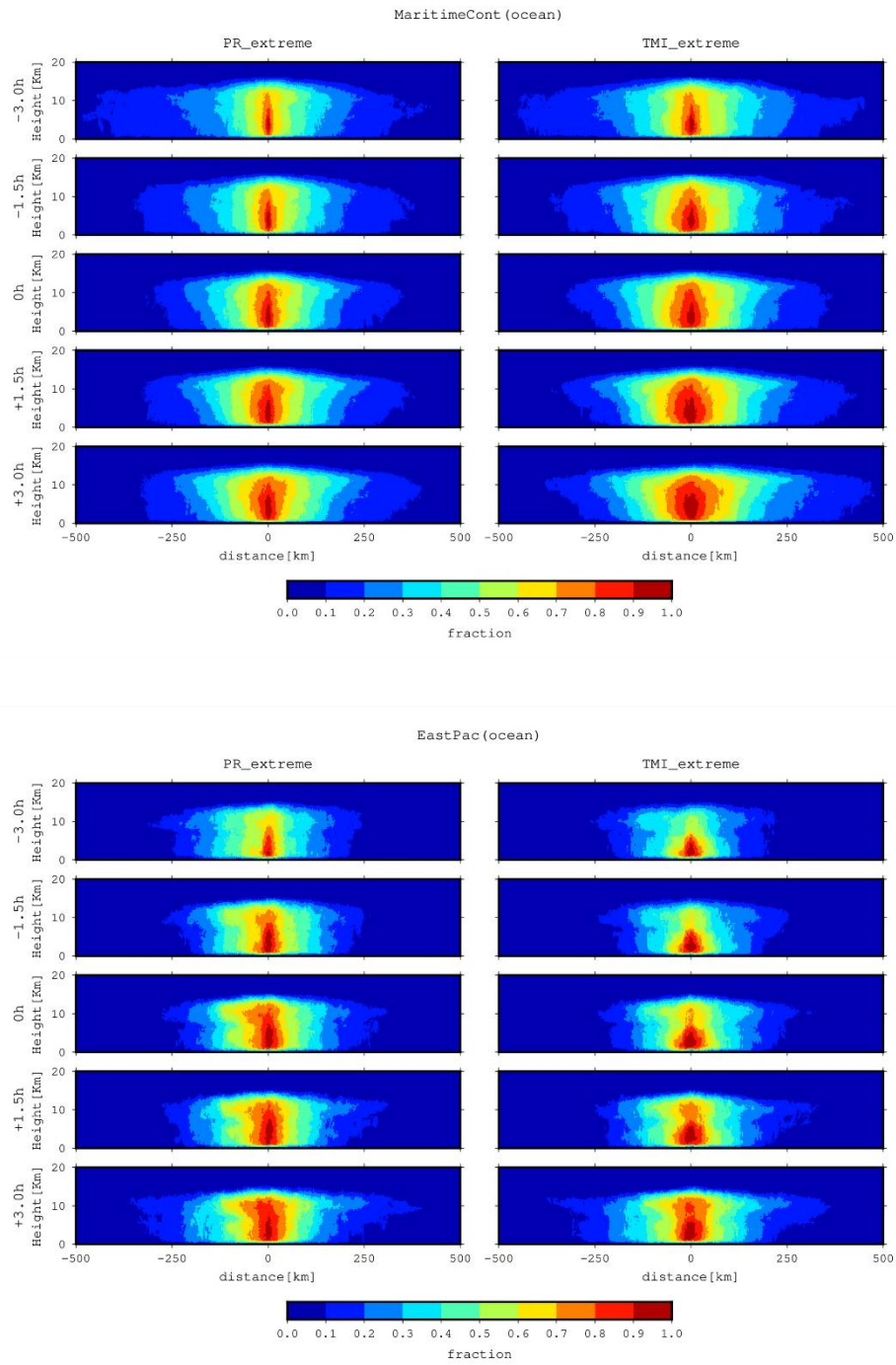


Figure 31. Temporal evolution of the CloudSat collocated cloud structures relative to TRMM extreme events (3 hours before and after). A contrast between PR and TMI extreme cloud structures over the Maritime Continent (top) and the East Pacific Ocean (bottom) is shown.

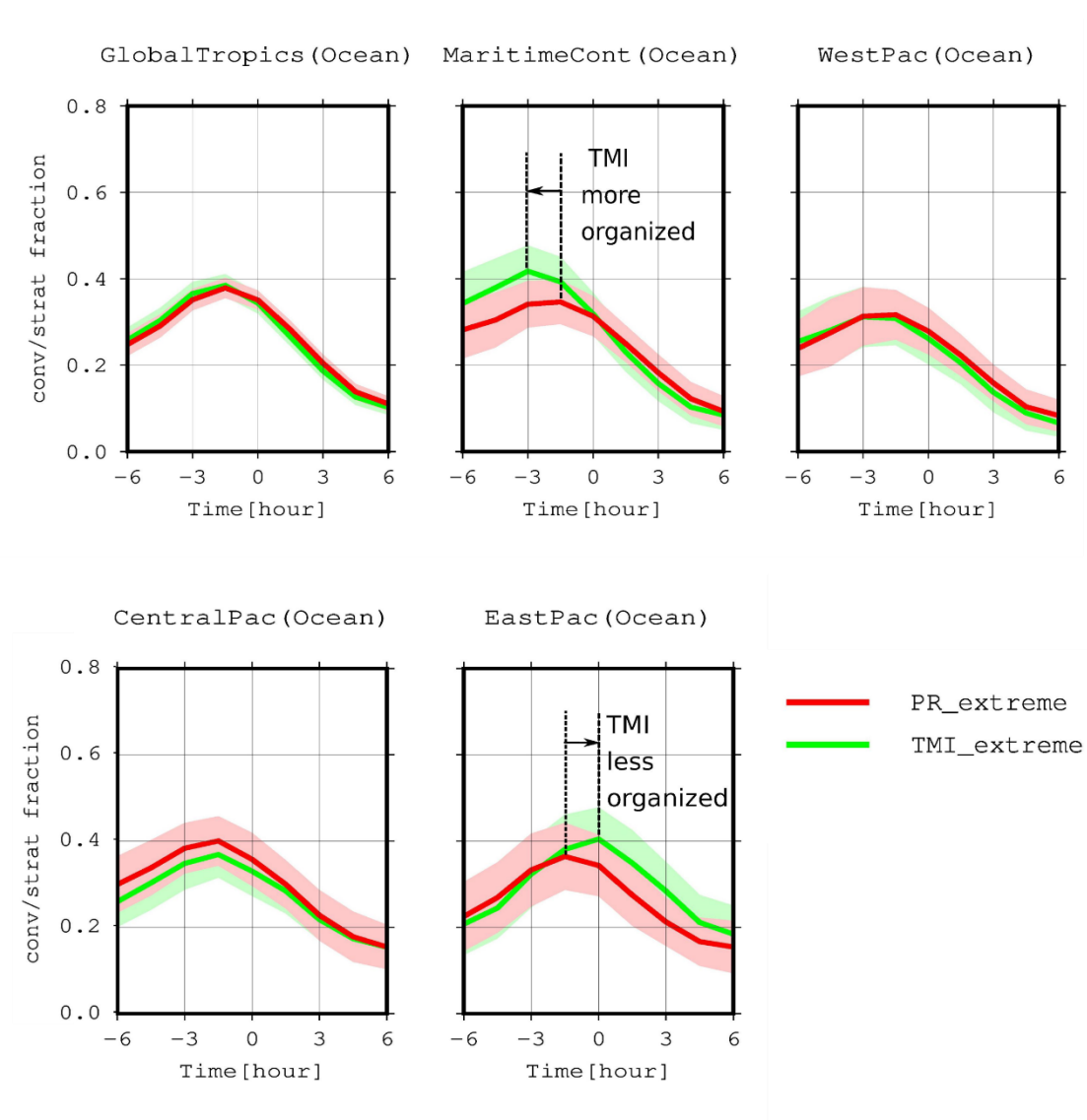


Figure 32. CloudSat convective fractions for the PR extreme events (red) and TMI extreme events (green) over the ocean domains. The shaded color represents the 95% confidence interval.

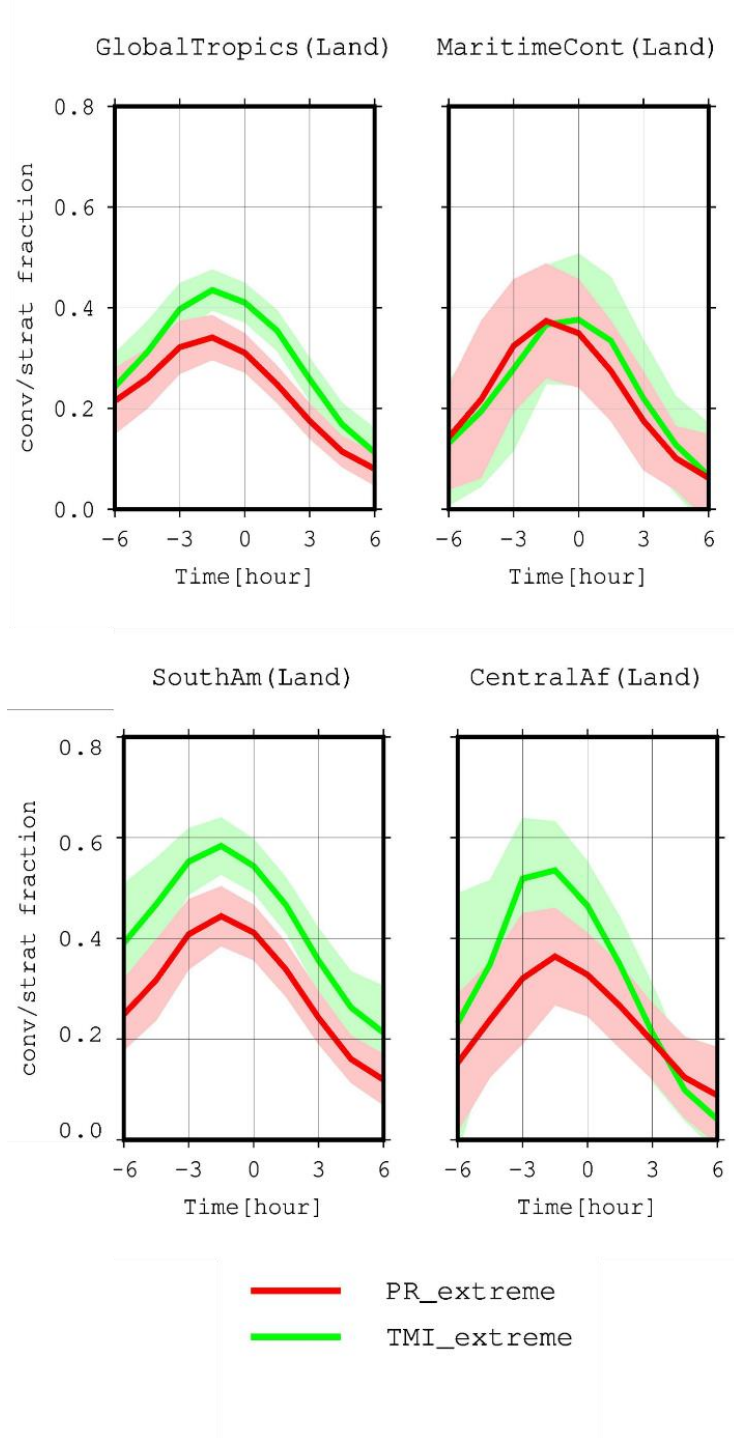


Figure 33. Similar to Figure 32, but for the land domains.

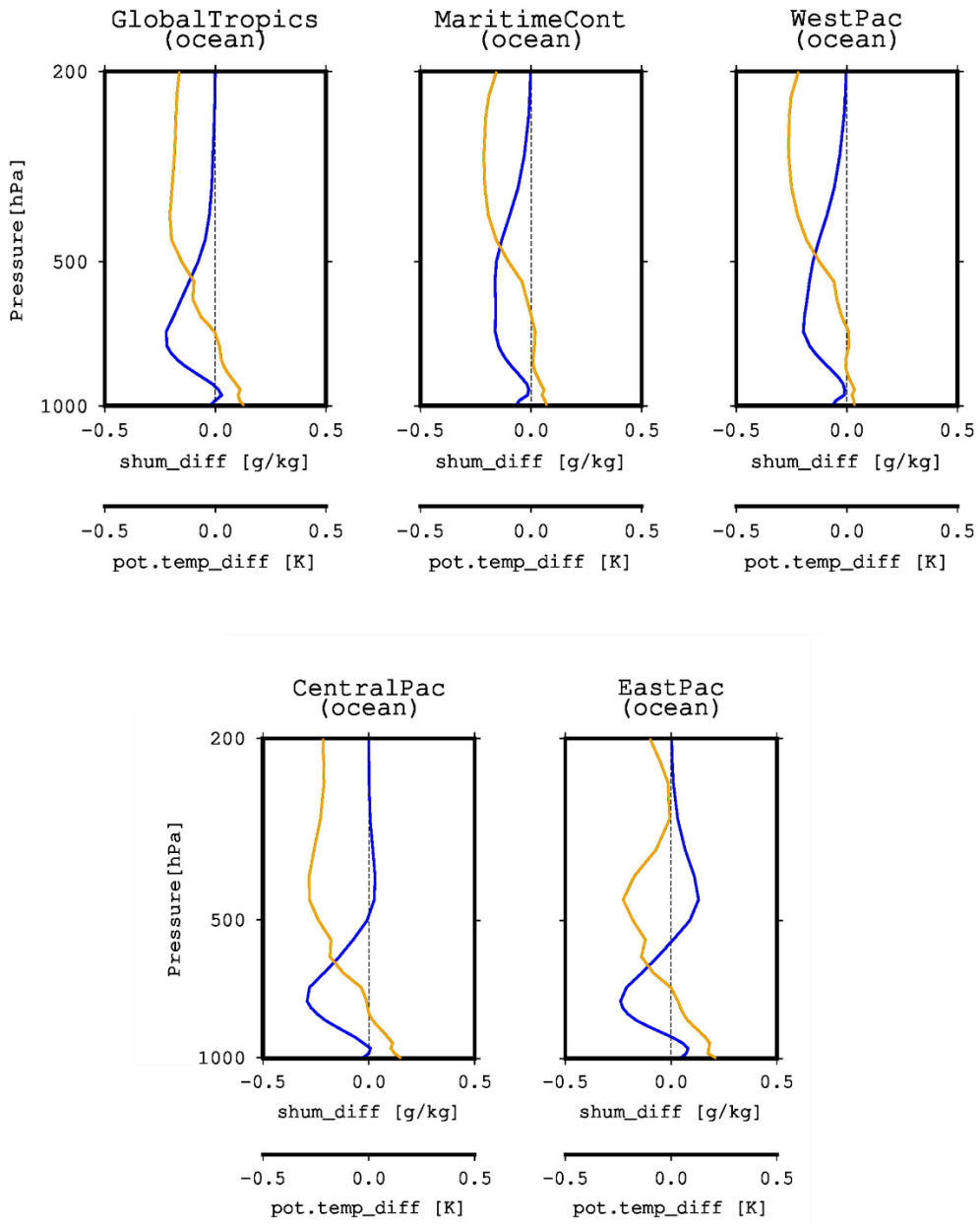


Figure 34. Specific humidity anomalies (blue) and air temperature anomalies (orange) from the ERA-Interim over-ocean regions in terms of the PR-TMI differences.

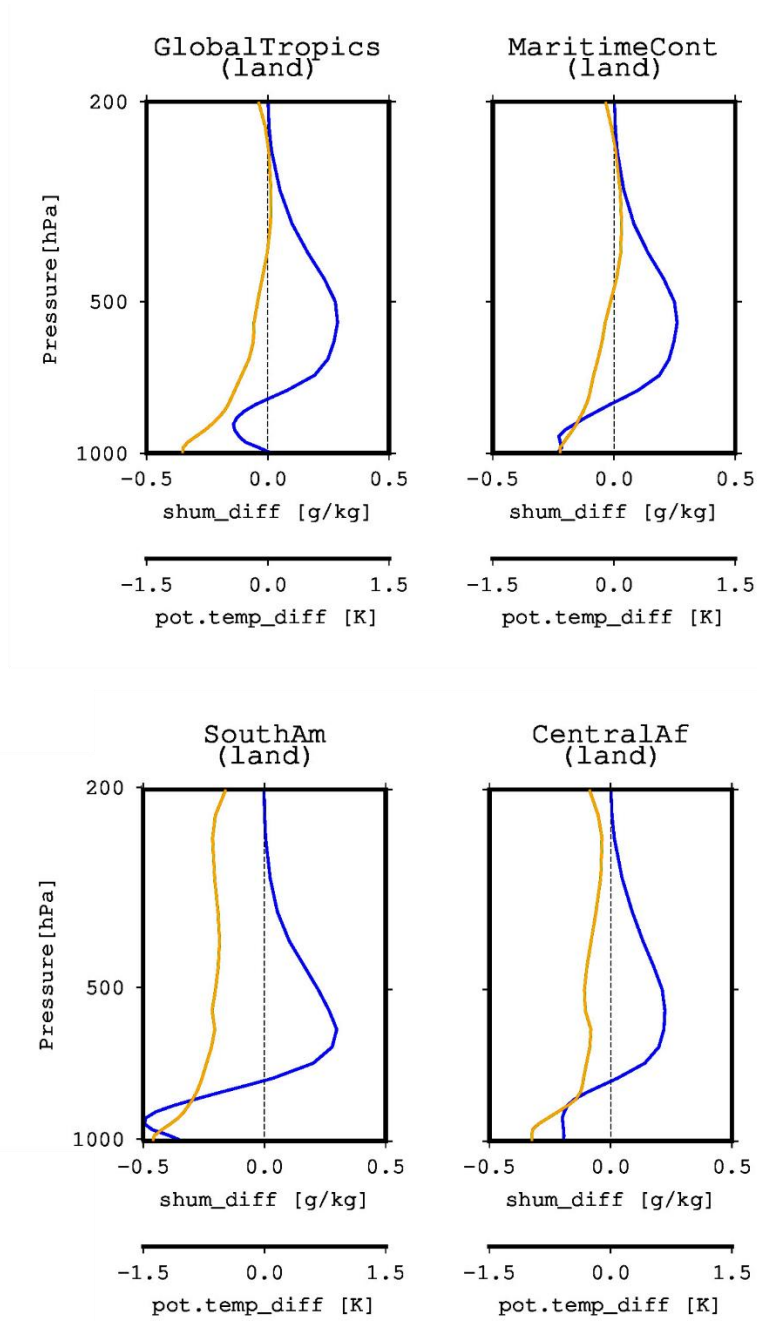


Figure 35. Similar to Figure 34, but for the land domains.

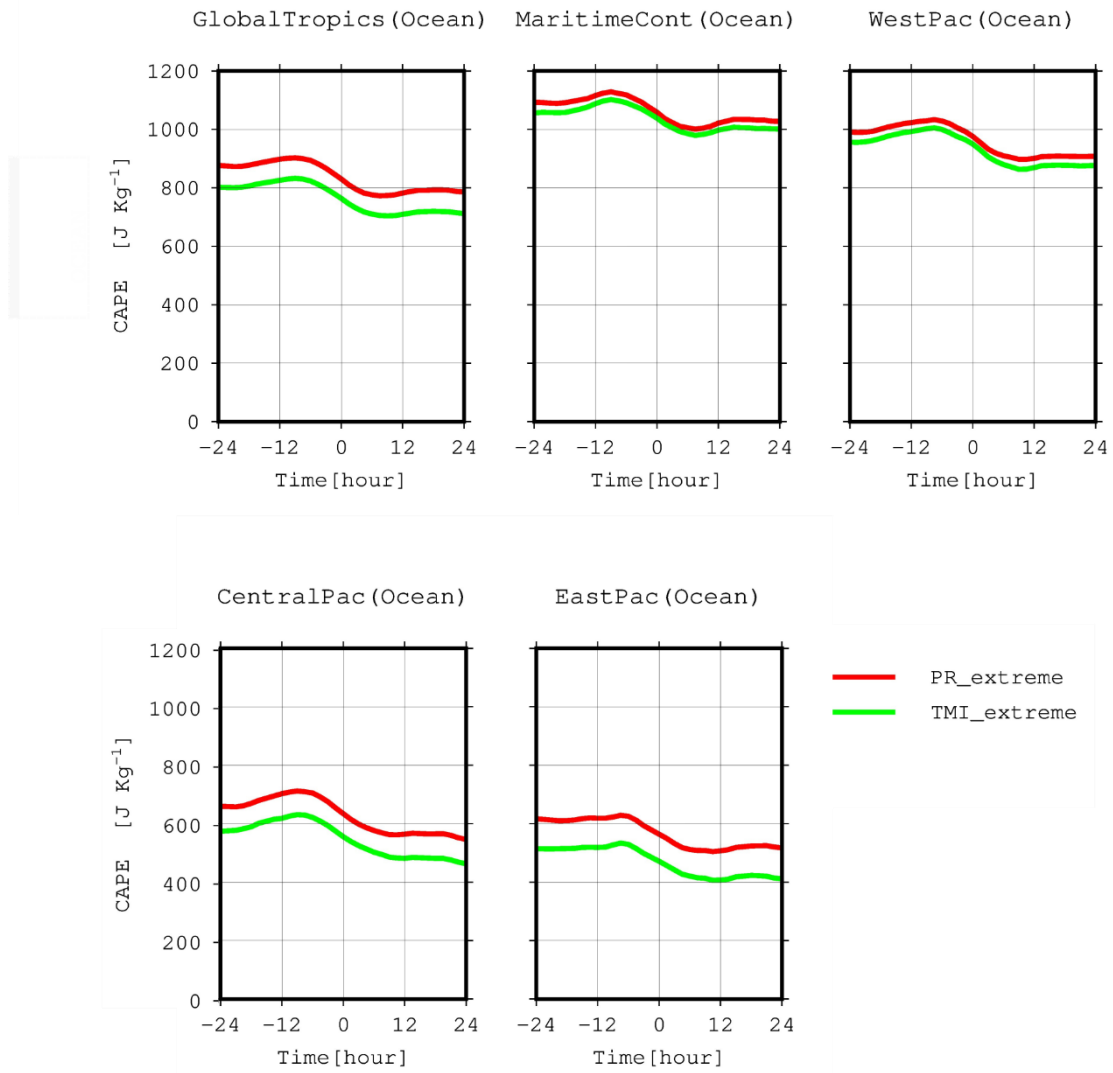


Figure 36. Temporal changes of the collocated Convective Available Potential Energy (CAPE) from the ERA-Interim data for the PR extreme events (red) and TMI extreme events (green) over the ocean domains.

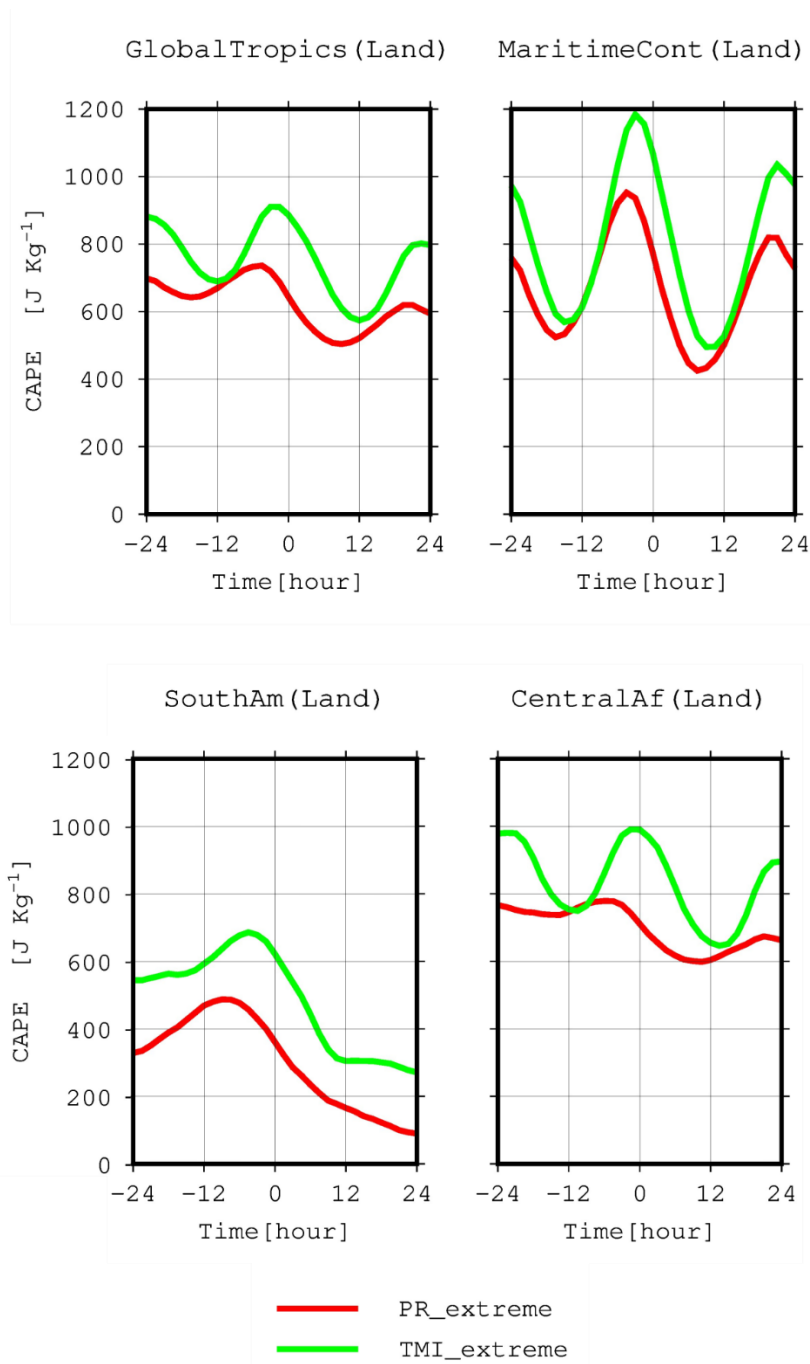


Figure 37. Similar to Figure 36, but for the land domains.

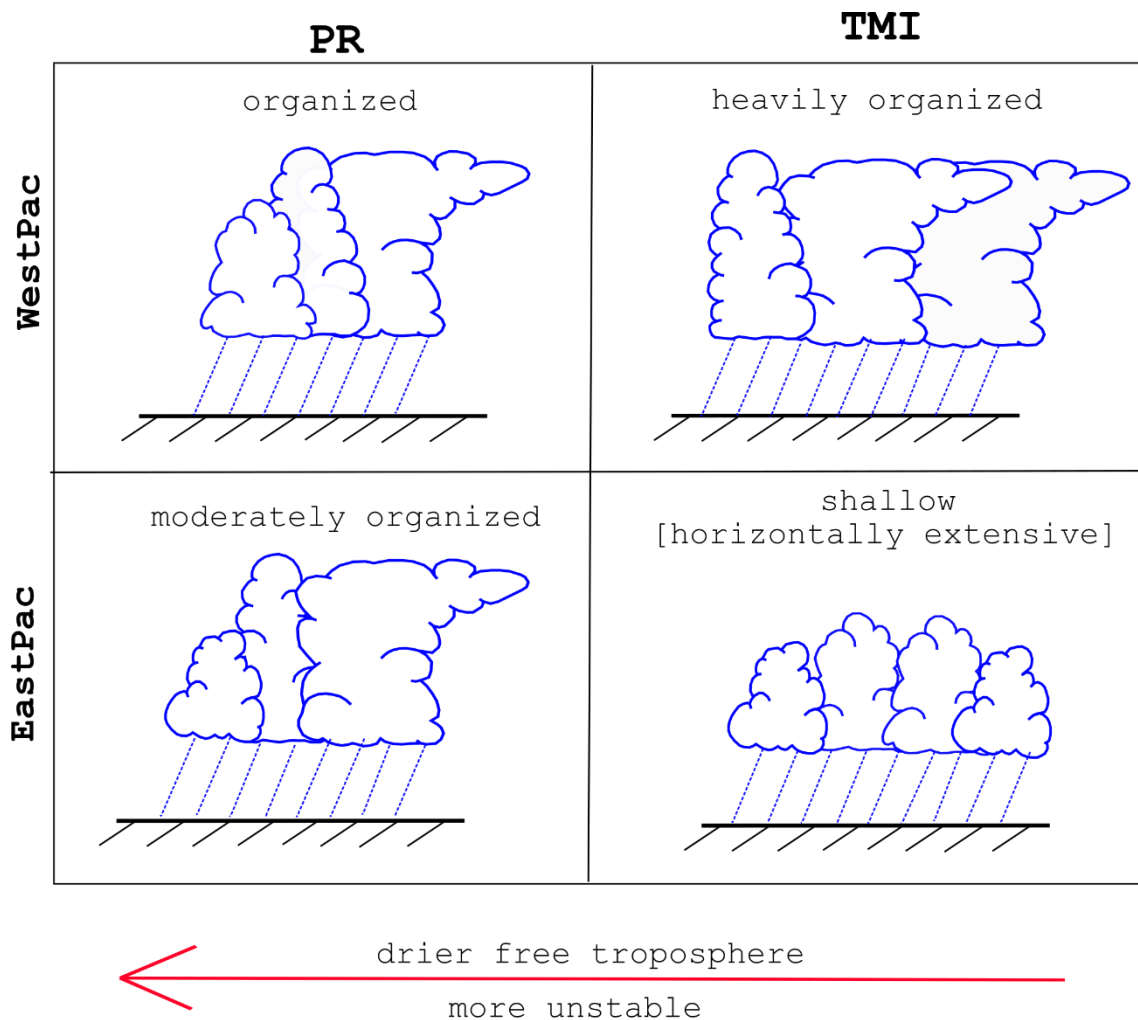


Figure 38. Illustration of the PR-TMI differences when identifying heavy rainfall events as associated with organized precipitation over ocean. The contrast between the eastern and western Pacific Oceans is shown in the figure.

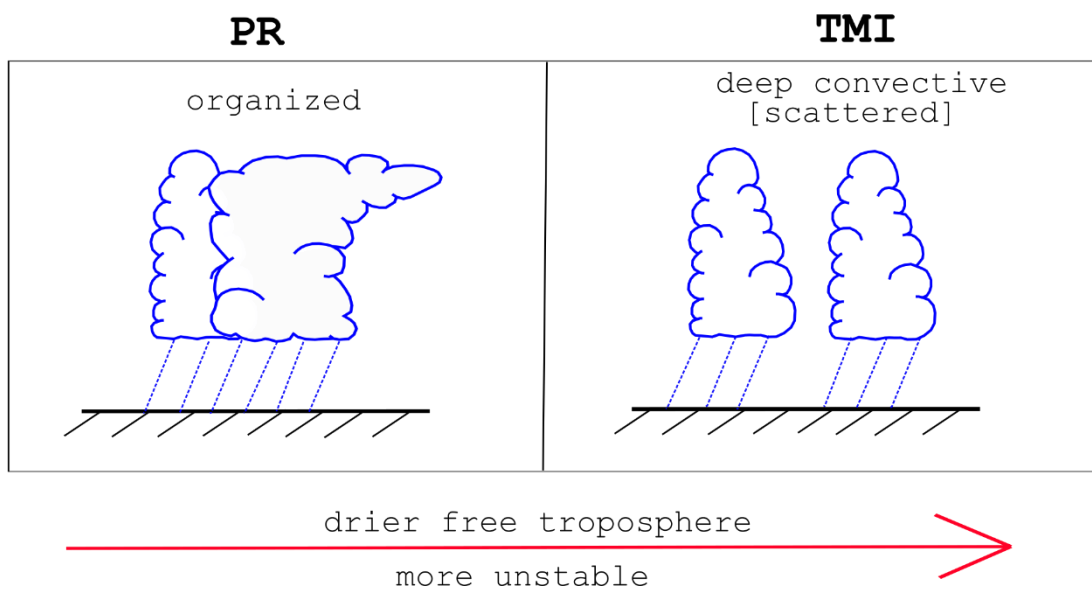


Figure 39. Similar to Figure 38, but for the land domains.

6. Conclusions

In summary, this research attempts to identify biases among different TRMM V7 products in estimating heavy rainfall over global tropics. These products and some ancillary datasets related to the rain-rate retrieval are matched up to identify the source of biases. The extreme-rain biases are then studied in more detail in terms of background physical processes using CloudSat and ERA-Interim datasets. In section 3, a pilot case study over the Maritime Continent is conducted to initially characterize the statistics of rain estimation biases in extreme rainfall. The result shows that extreme-rain biases among the TRMM datasets, particularly between the TRMM PR and TMI, exist due to different assumptions in the active-passive sensor retrieval processes. In section 4, a regional comparison of the rain estimation biases in extreme rainfall over global ocean and land domains is conducted. The results, again show that the different assumptions among the products account for generating rain estimation biases in extreme rainfall over the global tropics. In section 5, the rain estimation biases in extreme rainfall are examined further using collocated CloudSat and ERA-Interim datasets. The results indicate that different structures of convective organization could affect signals received by the active and passive sensors.

There are several key findings identified by this research. First, the extreme-rain biases have different characteristics compared to the climatological biases identified in many previous studies. This is because the assumptions inside the TRMM algorithms in estimating rain-rates in general, particularly from the TRMM TMI, are less robust for the extremes. Second, this research confirms the known limitation of the TMI land algorithm in estimating extreme rain-rates. The TMI land algorithm assumes that rain-rates is directly related with a larger number of ice particles aloft, while the PR identifies extreme events without much ice particles, but strong radar reflectivity near surface. As a result, the TMI identifies artificially high extreme frequency generated by afternoon precipitations. Third, this research shows that PR-TMI extreme-rain biases still exist over ocean although the TMI utilizes all of the emission and ice-scattering channels. The TMI tends to identify heavier rainfall when strong microwave emissions detected by the sensor. In contrast to the TMI, the PR identifies extreme events even with weak microwave emissions.

It is difficult to explain the above biases by utilizing PR and TMI datasets only, especially in relating the PR radar reflectivities and TMI brightness temperatures. In this research, utilization of CloudSat and ERA-Interim gives a detailed explanation of the above differences. The result shows that the biases are best explained in term of precipitation organization. Over the tropical ocean, the TMI tends to identify widely organized systems than the PR. This is mainly due to coarse resolution of the TMI emission bands. The widely organized systems have a large variation in term of heights. The TMI widely organized systems could have lower cloud top heights than the PR, such as over the East Pacific Ocean, or have taller cloud top heights than the PR, such as over the Maritime Continent Ocean. The widely organized systems identified by TMI, unfortunately, are less convective than identified by the PR. This might explain why the TMI's collocated PR profiles entirely have lower reflectivity than identified by the PR.

The characterization of the extreme precipitating systems over the tropical land shows that the warm rain extremes identified by the PR are associated with more organized systems than identified by the TMI. The organized systems maintain a large amount of moisture that is essential in the development of warm rain extremes. The TMI extreme events, on another hand, are associated with deep isolated systems. Large near-surface instability and strong ice-scattering signals indicate that the systems could be linked to the cold rain process. However, as indicated by PR vertical reflectivity profiles, the warm rain process could produce higher rain-rates than the cold rain process.

This research attempts to explain the differences between the TRMM PR and TMI when identifying heavy rainfall events over the global tropical lands and oceans. The results show that the PR and TMI detect heavy rainfall events from distinct physical processes that can be explained as a function of precipitation organization. Characterizing the precipitation organization could provide a potential application for reducing the rain-rate estimation biases in the active and passive sensors. This is not only useful for the future release of the TRMM products and its derivation, but also for newer satellites that utilize active and passive sensors. It is important to notice that TRMM dataset is selected in this research due to long-term observation periods and ended in 2014. As a successor to TRMM, The Global Precipitation Measurement (GPM) was launched on February 2014. The GPM contains a passive microwave sensor called GPM Microwave Imager (GMI). The GMI emission bands, in general, have finer resolution than TMI (about 32

km x 19 km for the 10 GHz channels). It is therefore important to identify whether the different precipitation organizations also exist in the GPM products.

References

- Adhikari, P., Y. Hong, K. R. Douglas, D. B. Kirschbaum, J. Gourley, R. Adler, and G. R. Brakenridge, 2010: A digitized global flood inventory (1998-2008): Compilation and preliminary results. *Nat. Hazards*, **55**, 405–422.
- Aldrian, E., and R. Dwi Susanto, 2003: Identification of three dominant rainfall regions within Indonesia and their relationship to sea surface temperature. *Int. J. Clim.*, **23**, 1435–1452.
- As-Syakur, A. R., T. Tanaka, T. Osawa, and M. S. Mahendra, 2013: Indonesian rainfall variability observation using TRMM multi-satellite data. *Int. J. Remote Sens.*, **34**, 7723–7738.
- Austin, R. T., A. J. Heymsfield, and G. L. Stephens, 2009: Retrieval of ice cloud microphysical parameters using the CloudSat millimeter-wave radar and temperature. *J. Geophys. Res. Atmos.*, **114**.
- Berg, W., T. L'Ecuyer, and C. Kummerow, 2006: Rainfall climate regimes: The relationship of regional TRMM rainfall biases to the environment. *J. Appl. Meteorol. Climatol.*, **45**, 434–454.
- Chang, C.-P., Z. Wang, J. McBride, and C.-H. Liu, 2005: Annual cycle of Southeast Asia-Maritime Continent rainfall and the asymmetric monsoon transition. *J. Clim.*, **18**, 287–301.
- CloudSat DPC, 2017: CloudSat 2B-GEOPROF. <http://www.cloudsat.cira.colostate.edu/data-products/level-2b/2b-geoprof>.
- Dee, D. P., and Coauthors, 2011: The ERA-Interim reanalysis: Configuration and performance of the data assimilation system. *Q. J. R. Meteorol. Soc.*, **137**, 553–597.
- European Centre for Medium-Range Weather Forecasts, 2017: ERA Interim. <https://www.ecmwf.int/en/forecasts/datasets/reanalysis-datasets/era-interim>.
- Furuzawa, F. A., and K. Nakamura, 2005: Differences of rainfall estimates over land by Tropical Rainfall Measuring Mission (TRMM) Precipitation Radar (PR) and TRMM Microwave Imager (TMI)-Dependence on storm height. *J. Appl. Meteorol.*, **44**, 367–383.
- Gopalan, K., N.-Y. Wang, R. Ferraro, and C. Liu, 2010: Status of the TRMM 2A12 land precipitation algorithm. *J. Atmos. Ocean. Technol.*, **27**, 1343–1354.
- Griffith, C. G., W. L. Woodley, P. G. Grube, D. W. Martin, J. Stout, and D. N. Sikdar,

- 1978: Rain estimation from geosynchronous satellite imagery—Visible and infrared studies. *Mon. Weather Rev.*, **106**, 1153–1171.
- Habib, E., A. Henschke, and R. F. Adler, 2009: Evaluation of TMPA satellite-based research and real-time rainfall estimates during six tropical-related heavy rainfall events over Louisiana, USA. *Atmos. Res.*, **94**, 373–388, doi:10.1016/j.atmosres.2009.06.015.
- Hamada, A., Y. N. Takayabu, C. Liu, and E. J. Zipser, 2015: Weak linkage between the heaviest rainfall and tallest storms. *Nat. Commun.*, **6**, 6213.
- Henderson, D. S., C. D. Kummerow, D. A. Marks, and W. Berg, 2017: A Regime-Based Evaluation of TRMM Oceanic Precipitation Biases. *J. Atmos. Ocean. Technol.*,.
- Hong, Y., R. F. Adler, A. Negri, and G. J. Huffman, 2007: Flood and landslide applications of near real-time satellite rainfall products. *Nat. Hazards*, **43**, 285–294.
- Houze, R. A., 1993: Cloud Dynamics, vol. 53 of the International Geophysics Series.
- Ichikawa, H., and T. Yasunari, 2006: Time-space characteristics of diurnal rainfall over Borneo and surrounding oceans as observed by TRMM-PR. *J. Clim.*, **19**, 1238–1260.
- Igel, M. R., A. J. Drager, and S. C. Heever, 2014: A CloudSat cloud object partitioning technique and assessment and integration of deep convective anvil sensitivities to sea surface temperature. *J. Geophys. Res. Atmos.*, **119**, 10515–10535.
- Iguchi, T., T. Kozu, R. Meneghini, J. Awaka, and K. Okamoto, 2000: Rain-profiling algorithm for the TRMM precipitation radar. *J. Appl. Meteorol.*, **39**, 2038–2052.
- , ———, J. Kwiatkowski, R. Meneghini, J. Awaka, and K. Okamoto, 2009: Uncertainties in the rain profiling algorithm for the TRMM precipitation radar. *J. Meteorol. Soc. Japan. Ser. II*, **87**, 1–30.
- Kiktev, D., D. M. H. Sexton, L. Alexander, and C. K. Folland, 2003: Comparison of modeled and observed trends in indices of daily climate extremes. *J. Clim.*, **16**, 3560–3571.
- Kirschbaum, D. B., R. Adler, Y. Hong, and A. Lerner-Lam, 2009: Evaluation of a preliminary satellite-based landslide hazard algorithm using global landslide inventories. *Nat. Hazards Earth Syst. Sci.*, **9**, 673–686.
- Kirstetter, P.-E., Y. Hong, J. J. Gourley, M. Schwaller, W. Petersen, and J. Zhang, 2013: Comparison of TRMM 2A25 Products, Version 6 and Version 7, with NOAA/NSSL Ground Radar–Based National Mosaic QPE. *J. Hydrometeorol.*, **14**, 661–669.

- Kozu, T., T. Iguchi, T. Kubota, N. Yoshida, S. Seto, J. Kwiatkowski, and Y. N. Takayabu, 2009: Feasibility of raindrop size distribution parameter estimation with TRMM precipitation radar. *J. Meteorol. Soc. Japan. Ser. II*, **87**, 53–66.
- Kripalani, R. H., and A. Kulkarni, 1997: Rainfall variability over South-east Asia—connections with Indian monsoon and ENSO extremes: new perspectives. *Int. J. Climatol.*, **17**, 1155–1168.
- Kumar, R., A. K. Varma, A. Mishra, R. M. Gairola, I. M. L. Das, A. Sarkar, and V. K. Agarwal, 2009: Comparison of TRMM TMI and PR version 5 and 6 precipitation data products under cyclonic weather conditions. *IEEE Trans. Geosci. Remote Sens. Lett.*, **6**, 378–382.
- Kummerow, C., 1998: Beamfilling errors in passive microwave rainfall retrievals. *J. Appl. Meteorol.*, **37**, 356–370.
- , and L. Giglio, 1994: A passive microwave technique for estimating rainfall and vertical structure information from space. Part I: Algorithm description. *J. Appl. Meteorol.*, **33**, 3–18.
- , W. S. Olson, and L. Giglio, 1996: A simplified scheme for obtaining precipitation and vertical hydrometeor profiles from passive microwave sensors. *Geosci. Remote Sensing, IEEE Trans.*, **34**, 1213–1232.
- , W. Barnes, T. Kozu, J. Shiue, and J. Simpson, 1998: The tropical rainfall measuring mission (TRMM) sensor package. *J. Atmos. Ocean. Technol.*, **15**, 809–817.
- , and Coauthors, 2001: The evolution of the Goddard Profiling Algorithm (GPROF) for rainfall estimation from passive microwave sensors. *J. Appl. Meteorol.*, **40**, 1801–1820.
- , P. Poyner, W. Berg, and J. Thomas-Stahle, 2004: The effects of rainfall inhomogeneity on climate variability of rainfall estimated from passive microwave sensors. *J. Atmos. Ocean. Technol.*, **21**, 624–638.
- Liu, C., and E. J. Zipser, 2005: Global distribution of convection penetrating the tropical tropopause. *J. Geophys. Res. Atmos.*, **110**, 1–12, doi:10.1029/2005JD006063.
- , and ———, 2013: Regional variation of morphology of organized convection in the tropics and subtropics. *J. Geophys. Res. Atmos.*, **118**, 453–466.
- , and ———, 2014: Differences between the Surface Precipitation Estimates from the TRMM Precipitation Radar and Passive Microwave Radiometer Version 7 Products.

- J. Hydrometeorol.*, **15**, 2157–2175.
- Maddox, R. A., 1980: Mesoscale Convective Complexes. *Bull. Am. Meteorol. Soc.*, **61**, 1374–1387.
- Masunaga, H., 2012: A Satellite Study of the Atmospheric Forcing and Response to Moist Convection over Tropical and Subtropical Oceans. *J. Atmos. Sci.*, **69**, 150–167.
- , T. Iguchi, R. Oki, and M. Kachi, 2002: Comparison of rainfall products derived from TRMM microwave imager and precipitation radar. *J. Appl. Meteor.*, **41**, 849–862.
- Moore, B. J., P. J. Neiman, F. M. Ralph, and F. E. Barthold, 2012: Physical Processes Associated with Heavy Flooding Rainfall in Nashville, Tennessee, and Vicinity during 1–2 May 2010: The Role of an Atmospheric River and Mesoscale Convective Systems. *Mon. Weather Rev.*, **140**, 358–378.
- Mori, S., and Coauthors, 2004: Diurnal land-sea rainfall peak migration over Sumatera Island, Indonesian maritime continent, observed by TRMM satellite and intensive rawinsonde soundings. *Mon. Wea. Rev.*, **132**, 2021–2039.
- NASA, 2011a: TRMM Product Level 2A Precipitation Radar (PR) Rainfall Rate and Profile.
http://disc.sci.gsfc.nasa.gov/precipitation/documentation/TRMM_README/TRMM_2A25_readme.shtml.
- , 2011b: TRMM Microwave Imager (TMI) Level 2A Hydrometeor Profile Product.
https://disc.gsfc.nasa.gov/precipitation/documentation/TRMM_README/TRMM_2A12_readme.shtml.
- , 2011c: Microwave Brightness Temperature (TMI).
https://disc.gsfc.nasa.gov/precipitation/documentation/TRMM_README/TRMM_1B11_readme.shtml.
- Nesbitt, S. W., E. J. Zipser, and D. J. Cecil, 2000: A census of precipitation features in the tropics using TRMM: Radar, ice scattering, and lightning observations. *J. Clim.*, **13**, 4087–4106.
- Pappenberger, F., E. Dutra, F. Wetterhall, and H. L. Cloke, 2012: Deriving global flood hazard maps of fluvial floods through a physical model cascade. *Hydrol. Earth Syst. Sci.*, **16**, 4143–4156.
- Prakash, S., C. Mahesh, R. M. Gairola, and P. K. Pal, 2012: Comparison of high-

- resolution TRMM-based precipitation products during tropical cyclones in the North Indian Ocean. *Nat. Hazards*, **61**, 689–701.
- Qian, J.-H., 2008: Why precipitation is mostly concentrated over islands in the Maritime Continent. *J. Atmos. Sci.*, **65**, 1428–1441.
- Rajendran, K., and T. Nakazawa, 2005: Systematic differences between TRMM 3G68 PR and TMI rainfall estimates and the possible association with life cycle of convection. *SOLA*, **1**, 165–168.
- Ramage, C. S., 1968: Role of A Tropical 'Maritime Continent' in the Atmospheric Circulation. *Mon. Weather Rev.*, **96**, 365–370.
- Reale, O., K. M. Lau, J. Susskind, and R. Rosenberg, 2012: AIRS impact on analysis and forecast of an extreme rainfall event (Indus River Valley, Pakistan, 2010) with a global data assimilation and forecast system. *J. Geophys. Res. Atmos.*, **117**.
- Rickenbach, T. M., and S. A. Rutledge, 1998: Convection in TOGA COARE: Horizontal scale, morphology, and rainfall production. *J. Atmos. Sci.*, **55**, 2715–2729.
- Salahuddin, A., and S. Curtis, 2011: Climate extremes in Malaysia and the equatorial South China Sea. *Glob. Planet. Change*, **78**, 83–91.
- Schumacher, C., and R. A. Houze Jr, 2000: Comparison of radar data from the TRMM satellite and Kwajalein oceanic validation site. *J. Appl. Meteorol.*, **39**, 2151–2164.
- Schumacher, R. S., and R. H. Johnson, 2005: Organization and Environmental Properties of Extreme-Rain-Producing Mesoscale Convective Systems. *Mon. Weather Rev.*, **133**, 961–976.
- Shige, S., H. Sasaki, K. Okamoto, and T. Iguchi, 2006: Validation of rainfall estimates from the TRMM precipitation radar and microwave imager using a radiative transfer model: 1. Comparison of the version-5 and-6 products. *Geophys. Res. Lett.*, **33**.
- Shige, S., Y. N. Takayabu, and W. K. Tao, 2008: Spectral retrieval of latent heating profiles from TRMM PR data. Part III: Estimating apparent moisture sink profiles over tropical oceans. *J. Appl. Meteorol. Climatol.*, **47**, 620–640.
- Simpson, J., C. Kummerow, W.-K. Tao, and R. F. Adler, 1996: On the tropical rainfall measuring mission (TRMM). *Meteorol. Atmos. Phys.*, **60**, 19–36.
- Sohn, B. J., M. J. Choi, and J. Ryu, 2015: Explaining darker deep convective clouds over the western Pacific than over tropical continental convective regions. *Atmos. Meas. Tech.*, **8**, 4573–4585.

- Song, H.-J., and B.-J. Sohn, 2015: Two heavy rainfall types over the Korean peninsula in the humid East Asian summer environment: A satellite observation study. *Mon. Weather Rev.*, **143**, 363–382.
- , ———, S.-Y. Hong, and T. Hashino, 2017: Idealized numerical experiments on the microphysical evolution of warm-type heavy rainfall. *J. Geophys. Res. Atmos.*, **122**, 1685–1699.
- Spencer, R. W., H. M. Goodman, and R. E. Hood, 1989: Precipitation retrieval over land and ocean with the SSM/I: Identification and characteristics of the scattering signal. *J. Atmos. Ocean. Technol.*, **6**, 254–273.
- Stephens, G. L., and Coauthors, 2002: The CloudSat mission and the A-Train: A new dimension of space-based observations of clouds and precipitation. *Bull. Am. Meteorol. Soc.*, **83**, 1771–1790.
- Tangang, F. T., L. Juneng, E. Salimun, P. N. Vinayachandran, Y. K. Seng, C. J. C. Reason, S. K. Behera, and T. Yasunari, 2008: On the roles of the northeast cold surge, the Borneo vortex, the Madden-Julian Oscillation, and the Indian Ocean Dipole during the extreme 2006/2007 flood in southern Peninsular Malaysia. *Geophys. Res. Lett.*, **35**.
- Wang, N.-Y., C. Liu, R. Ferraro, D. Wolff, E. Zipser, and C. Kummerow, 2009: TRMM 2A12 Land Precipitation Product - Status and Future Plans. *J. Meteorol. Soc. Japan. Ser. II*, **87A**, 237–253.
- Wilheit, T., and Coauthors, 1994: Algorithms for the retrieval of rainfall from passive microwave measurements. *Remote Sens. Rev.*, **11**, 163–194.
- Wilheit, T. T., 1986: Some comments on passive microwave measurement of rain. *Bull. Am. Meteorol. Soc.*, **67**, 1226–1232.
- Yamamoto, M. K., F. A. Furuzawa, A. Higuchi, and K. Nakamura, 2008: Comparison of diurnal variations in precipitation systems observed by TRMM PR, TMI, and VIRS. *J. Clim.*, **21**, 4011–4028.
- Zagrodnik, J. P., and H. Jiang, 2013: Investigation of PR and TMI Version 6 and Version 7 Rainfall Algorithms in Landfalling Tropical Cyclones Relative to the NEXRAD Stage-IV Multisensor Precipitation Estimate Dataset. *J. Appl. Meteorol. Climatol.*, **52**, 2809–2827.